# CONDUCTIVE POLYMER MICROWIRES FOR SINGLE CELL BIOELECTRICAL STIMULATION

A Dissertation
Presented to
The Academic Faculty

By

Scott B. Thourson

In Partial Fulfillment
of the Requirements for the Degree
Doctor of Philosophy in
Bioengineering

Georgia Institute of Technology

August 2018

**CONDUCTIVE POLYMER MICROWIRES FOR SINGLE CELL BIOELECTRICAL STIMULATION**

Approved by:

Dr. Christine K. Payne, Advisor
Mechanical Engineering and Materials Science
*Duke University*

Dr. Craig R. Forest, Co-Advisor
The George W. Woodruff School of Mechanical Engineering
*Georgia Institute of Technology*

Dr. Garrett B. Stanley
Wallace H. Coulter Department of Biomedical Engineering
*Georgia Institute of Technology*

Dr. Todd Sulchek
The George W. Woodruff School of Mechanical Engineering
*Georgia Institute of Technology*

Dr. Maysam Ghovanloo
School of Electrical and Computer Engineering
*Georgia Institute of Technology*

Date Approved: April 19, 2018

Just keep walking. The mountains do not care.

*Shannon J. Timpe, PhD*

## ACKNOWLEDGEMENTS

This research was completed with so many brilliant people who gave me their time and patience. I would like to thank my primary PhD advisor Christine Payne for her guidance, patience, and support. The Payne Lab played an important role in my development as a researcher with excellent scientific discussions and brainstorming sessions; I am grateful. I thank Craig Forest for going above and beyond the call of duty for a co-advisor and providing me with unwavering support. Although my presence was inconsistent, the willingness to provide feedback and have valuable scientific discussions was always consistent in the Forest Lab - thank you. I also want to thank those in the Dixon Lab - particularly Josh Hooks and Zhanna Nepiyushchikh who spent hours helping me suspend rat hearts from syringe needles. I really appreciate Sandra Gonzalez from the Cho Lab at Emory who helped me at a critical time in my research. Thank you to my friends who always gave me great advice and kept my spirits up.

I want to also thank my thesis committee who never hesitated to meet with me upon request and was willing to have update meetings every 6 months leading up to my defense. Their advice was had an enormous impact on the success of my research trajectory. I am grateful for my undergraduate research advisor, Dr. Shannon Timpe, who really changed my life and gave me all the tools I needed to enjoy good music, drink good whiskey, and be a successful graduate student.

I, of course, want to thank my family for their love and support. My mother never knew what I was up to for the past 10 years, but always knew what I was going through better than anyone. My brother was my inspiration to pursue science. His curiosity and independence rubbed off on me and is the reason I made it this far. Lastly, I want to thank my wonderful partner Emily who has stuck with me through the hardest times that we have had to endure yet. She will always be the love of my life. Thank you.

## TABLE OF CONTENTS

## LIST OF TABLES

# LIST OF FIGURES

## SUMMARY

There are currently no bioelectrical probes that are able to provide long-term electrical connections to a large population of single cells in the body. The challenge is multi-faceted: engineering an array of subcellular probes that are long, thin, mechanically flexible, electrically conductive, biochemically stable, and can be routed to individual target cells in a hostile, 3D tissue matrix. Conductive polymers have extraordinary properties that could enable the design of a bioprobe that meets many of these requirements simultaneously. The principal advantage of conductive polymers is the combination of their mechanical flexibility, electron conductivity, and efficiency in converting electrons to electric fields in electrolyte solutions. Conductive polymers have historically always been employed as films, but a synthesis method developed by Flanders et. al. yields high-aspect ratio polymer wires with dimensions ranging from 150 nm to 10 μm in diameter and up to millimeters in length. The research presented here investigates conductive polymer microwires for local electric field generation at the single cell level. This work focuses on experimentally characterizing the electrical properties of these wires and their ability to generate local electric fields for single cell stimulation. The advantages and limitations of their performance are identified in light of the ideal bioelectrical probe. The results are used to build a simulation model that can predict local electric field generation by current conductive polymer wires as well as wires with different shapes and enhanced material properties. The current work concludes that the conductivity of conductive polymers is not sufficient to permit the use of small, flexible wire sizes (smaller than 2 x 27 μm) to electrically stimulate single cells. Although conductive polymers are not suitable for electron conduction, their extremely low surface impedance makes them the best material for converting electron current into ionic electric fields at small scales. Thus, conductive polymers do not overcome all the challenges of electrically wiring every cell in our brain, per se, but they do have a critical niche in enabling subcellular dimensions for the next generation of bioelectrical probes.

# CHAPTER 1
# INTRODUCTION AND BACKGROUND

Complete measurement (recording) and control (stimulation) of every neuron in the brain simultaneously is the ideal scenario for understanding and treating the brain. However, it is difficult to even imagine a plausible means by which to achieve this goal when considering the number of neurons and their physical dimensions. There are about 86 billion neurons in the average human brain [1]. Each of these cells are about the diameter of a human hair. These cells form circuits and networks that give humans the ability to do everything from storing memories to initiating muscle contraction. Abnormalities in the brain can lead to dysfunctional behaviors such as tremors in Parkinson's disease patients, chronic pain, or depression. But, we do not know which cells or circuits are responsible for these abnormalities. Therefore, both our ability to treat and understand these brain dysfunctions requires the ability to control and probe individual neurons in the brain on a large scale *in vivo*. There is currently no method to achieve this due to the long list of challenges in electrically interacting with several individual cells in human brain tissue. The challenges originate from biological, mechanical, or electrical constraints that are inter-dependent [2]. The vast majority of approaches that have been developed so far only focus on addressing one or two of these constraints. This introduction will provide a brief overview of bioelectricity, methods of probing and controlling the brain, and conductive polymers for neural stimulation. Although the discussion here will focus on stimulation, it is worth noting that there is a great deal of overlap between research on electrodes for cell stimulation (i.e. sending signals) and cell recording (i.e. receiving signals), especially from a biocompatibility perspective.

## 1.1 Bioelectrical interface overview

Much of what is known about the brain has been compiled by several different tools used for measuring and inducing signals in the brain. These techniques interact with the brain either via contact (tissue implanted) or non-contact (ex vivo) methods. Almost all of these techniques are exclusively based on electromagnetic energy including electric fields, light, and magnetic fields. Contact methods sacrifice invasiveness for high resolution by penetrating tissue and interacting with neurons through locally generated fields. Non-contact methods are largely noninvasive and use fields to interact with brain cells from outside of the body. The advantage of non-contact methods is that they are noninvasive and also high-throughput, but they have poor resolution. A brief overview on the bioelectrical nature of cells and how external fields can stimulate cells is discussed first. Current technology for invasive and noninvasive neural devices follows.

### 1.1.1 Cell membrane potential

Electrical signals between cells generally originate from changes in the electrochemical voltage potential across the cell membrane. The membranes of electrically-active cells such as neurons and cardiomyocytes contain chemical-gated and voltage-gated ion channels. Each channel controls the passage of specific ions. This semi-permeable barrier along with ion pumps allows cells to control ion concentration gradients between intracellular and extracellular solutions. Much like a battery, a difference in ion concentration across the cell membrane generates a voltage and is called the membrane potential. The magnitude of this electrochemical potential can be approximated by the Nernst equation:

$$E = \frac{RT}{zF} ln\left(\frac{C_{out}}{C_{in}}\right) \tag{1.1}$$

where $E$ is the electrochemical potential, $R$ is the gas constant, $T$ is temperature, $z$ is the charge of the ionic species, $F$ is Faraday's constant, and $C_{in}$ and $C_{out}$ are the concentrations

of a given ion inside and outside of the cell, respectively. Thus, the cell membrane potential can be controlled by changing the local ion concentration on the inside or the outside of the cell. Changes in membrane potential is the basis for cellular electrical communication.

### 1.1.2 Biological action potentials

Cells electrically communicate in a digital fashion by modulating their membrane potential between -70 mV (stable, resting state) and +35 mV (unstable, depolarized state) [3]. The exact voltage potentials vary between cell types and individual cells, but these values will be used here as an example. These digital potential states are analogous to modern digital electronics, which use the binary states 0 and 1 for communication. Also like digital electronics, there is a threshold voltage (near -55 mV) at which the membrane potential will assume either of these states. At any voltage below -55 mV, the membrane potential will return to its resting state (-70 mV). At any voltage above -55 mV, voltage-gated ion channels in the cell membrane open to electrochemically ”short” the cell membrane. The membrane potential will transiently depolarize to +35 mV and then return back to -70 mV. This transient signal pulse or potential spike is called an action potential (Figure 1.1). Signal transmission occurs when the action potential of one cell causes ion channels to open in nearby cells to propagate the action potential signal. The sites of interaction between neurons occurs at junctions called synaptic clefts. During signal transmission, an action potential in the transmitting cell (pre-synaptic neuron) reversibly releases signal molecules known as neurotransmitters into the synaptic cleft nano-environment. Neurotransmitters from the transmitting cell bind to and open receptor-gated ion channels ion channels on the receiving cell (post-synaptic neuron) to propagate the action potential signal. A single cell can propagate an action potential signal to several neurons simultaneously. It is estimated that are about 100 trillion of these connections between neurons in the human brain.

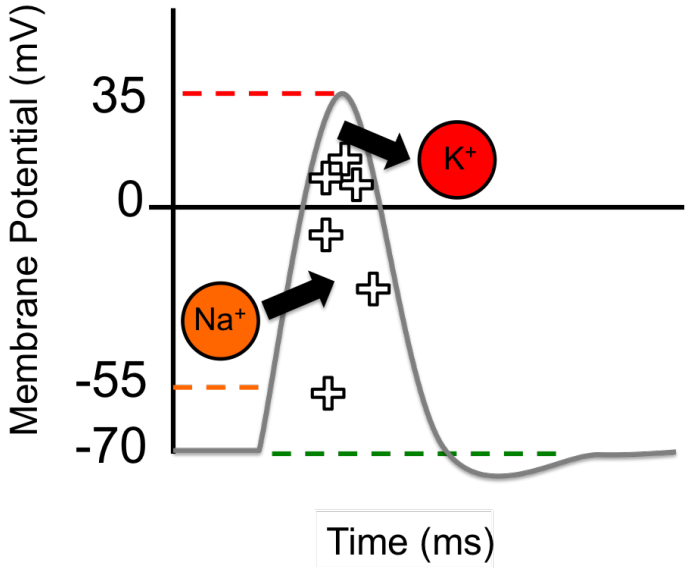


**Figure 1.1:** An illustration of a typical neuron action potential shape. Once the voltage rises above -55 mV, sodium ion channels open to depolarize the cell. Ion channels subsequently open to release intracellular potassium and re-polarize the membrane back to its resting state (-70 mV).

### 1.1.3 Artificially-induced action potentials

Our ability to control neuron stimulation hinders on our ability to mimic the initiation of an action potential by sufficiently depolarizing the cell membrane potential. The fundamental goal is to open and close ion channels in the cell membrane of an individual cell. Membrane depolarization can be achieved by increasing extracellular potassium concentration, locally release neurotransmitters, or incorporating more ion channels in the cell membrane. These strategies mimic actual biological stimulation but cannot easily target a single cell *in vivo* due to diffusion. Electrodes have become the standard method of single cell stimulation because they are capable of transiently changing local ion concentrations using electric fields. Since the cell membrane potential depends on both the intracellular and extracellular concentrations, electrodes can stimulate cells from either side of the cell membrane. This research focuses on extracellular stimulation due to the complexity in integrating electrodes into the cell membrane [4, 5]. Significant work on the theory and modeling of extracellular stimulation with electrodes was developed by Rattay et. al. who applied cable theory to axon stimulation [6, 7]. The cable model was originally developed for modeling underwater submarine telegraphic transmission lines. For neurons, the model assumes axons are

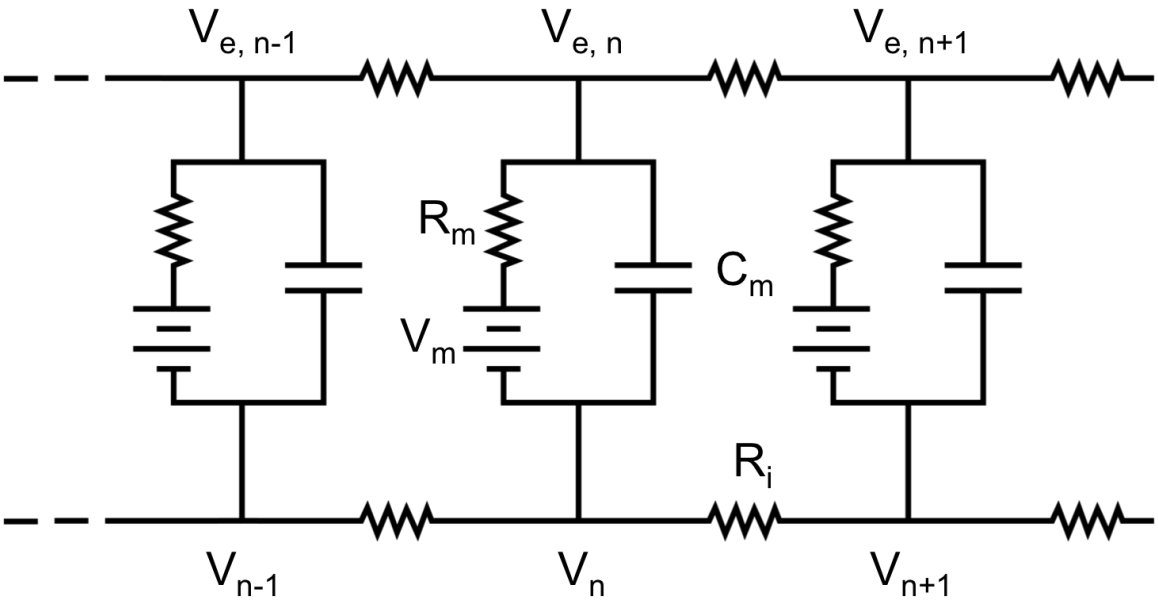


**Figure 1.2:** Equivalent circuit for 1-dimensional cable theory to model membrane potential along a cylindrical axon where $V_{e,n}$ is the extracellular potential, $V_m$ is the cell-generated potential, $R_m$ is the cell membrane resistance, $C_m$ is the cell membrane capacitance, and $R_i$ is the intracellular resistance along the axon. Membrane potential is solved at discrete intracellular points $V_n$.

cylindrical membranes that can be modeled as a passive, 1-dimensional equivalent circuit network. The membrane is treated as a series of resistors and capacitors in parallel, while the intracellular space is modeled as a series of resistors as shown in Figure 1.2. where $V_m$ is the resting cell membrane potential, $R_m$ is the cell membrane resistance, $C_m$ is the cell membrane capacitance, and $R_i$ is the intracellular resistance along the axon. Kirchoff's current law is used to solve for membrane potential at discrete intracellular points $V_n$ along the cable [6, 7]:

$$\frac{\Delta V_n}{\Delta t} = \frac{1}{c_m}\left\{\frac{\Delta x}{4\rho_i L}\left(\frac{V_{n-1} - 2V_n + V_{n+1}}{\Delta x^2} + \frac{V_{e,n-1} - 2V_{e,n} + V_{e,n+1}}{\Delta x^2}\right) - i_{ionic,n}\right\} \quad (1.2)$$

where $V_n$ is the reduced membrane potential, $c_m$ is the specific cell membrane capacitance, $d$ is the axon diameter, $x$ is the position coordinate along the axon, $\rho_i$ is intracellular resistivity, $L$ is the active length of the membrane, $V_{e,n}$ is the external potential, and $i_{ionic,n}$ is the current at the nth node. The time-dependent nature changes in the various ion channel conductance during changes in membrane potential can be accounted for using the Hodgkin-Huxley model [8]. For a long, straight unmyelinated axon, the extracellular po-

tential simplifies to the following:

$$f(x,t) = \frac{\partial^2 V_e(x,t)}{\partial x^2} \tag{1.3}$$

which is known as the activation function [6, 7]. When this function is positive, depolarization of the membrane occurs, which is necessary to raise the membrane potential above the action potential threshold. Therefore, the second partial spatial derivative of the extracellular potential along membrane of an axon is generally the quantity of interest for generating a field capable of cell stimulation, although modifications may be required for studies on cells with different shapes, stimulation frequencies, or media conditions [9–12].

Research work has also focused on simulating and modeling of extracellular electrode properties with respect to the generation of electric fields. Yvert et. al. has published excellent work in modeling extracellular fields and cell responses with a focus on the electrode properties [13–16]. An under-appreciated point of their work was the need for a Robin boundary condition at the electrode/electrolyte interface to accurately model the true potential field generated by electrodes [15]. The resulting potential fields predicted with the inclusion of this boundary condition have also been experimentally verified [14]. A robin boundary condition is defined by two other types of boundary conditions called Dirichlet and Neumann boundary conditions, which specify a value and derivative at the boundary. Effectively, a Robin boundary defines the voltage drop that occurs at the electrode/electrolyte interface. The physical origin of this phenomenon is due to the capacitive and resistive electrochemical behavior at a charged surface in an ionic solution. The term used for this type of impedance is called surface impedance. The most direct way to measure surface impedance for various materials is electrical impedance spectroscopy (EIS). EIS measurements apply voltage potentials to the electrode at typical frequencies from $\sim$1 Hz to as high as 100 kHz. The spectrum can be plotted to in a Nyquist plot and fit using equivalent circuit models to assign values to physical quantities such as surface charge

capacitance and charge transfer resistance. Surface impedance depends on the material, charge transfer mechanism, surface roughness, and electrolyte solution. A higher charge storage density (or charge injection capacity) is typically associated with a low surface impedance.

Most cells do not have perfect, straight cylindrical features and electrodes are not ideally polarizable and generate electric fields that depend on a multitude of conditions. Therefore, experiment and modeling studies are both needed to develop an understanding of the fields that electrodes generate and the response of cells in those fields. Bioelectrical stimulation becomes further complex in a biological environment. Current methods of stimulating and recording neuron signals have had moderate success but still have many limitations that hinder our ability to effectively treat and understand the brain.

## 1.2 Noninvasive methods

### 1.2.1 Recording

Obtaining an electroencephalogram (EEG) is the simplest noninvasive technique for recording brain activity. It uses electrodes on the subject's scalp that can measure activity in areas of the cerebrum of the brain. EEG is the primary method of identifying patients with epilepsy [17]. Because this method relies on the placement of electrodes on the outside of the skull, there is a lack of spatial accuracy, resolution, and depth [18]. In contrast, a technique called functional magnetic resonance imaging (fMRI) can acquire full images of the brain that report activity in regions of the brain in an awake human subject. The combination of high throughput and $\sim$1 mm$^3$ resolution enables this technique to identify patients with a variety of brain dysfunctions from attention deficit hyperactivity disorder [19] to Alzheimer's disease [20]. The drawbacks of fMRI is the need for high magnetic field strengths and expensive equipment. Both of EEG and fMRI are useful for diagnostics, but they lack single cell resolution to elucidate a deeper understanding of the brain. For example, each pixel in a fMRI image is called a voxel and is defined as a 1 mm$^3$ cube. There

are about 100,000 neurons in each voxel, but it has been shown that even a single neuron can affect behavior [21]. Therefore, there is a need for tools that can interact with the brain at a single cell level.

### 1.2.2 Stimulation

In general, noninvasive brain stimulation (NIBS) has been around for almost four decades [22]. Yet, the variety of non-contact methods to stimulate cells are few because fields are difficult to control at very far distances from target cells. The two most common methods are transcranial magnetic stimulation (TMS) and transcranial electrical stimulation (tES). TMS uses electromagnetic induction to induce electric fields in the brain whereas tES directly generates electric fields in the brain. Both of these methods lack spatial and temporal resolution for the same reasons as EEG and fMRI. Additionally, these methods are only effective near the primary motor cortex [18] and can not be used for deep brain stimulation applications. A recent study demonstrated a method the authors called "temporal interference" that used the frequency of generated electric fields to stimulate neurons in the hippocampus [23]. This technique is similar to the way two-photon microscopy confines fluorescence excitation. This research shows promise for deeper penetration of NIBS methods, but it has not been attempted in humans. NIBS techniques are not yet capable of single cell stimulation and have only recently demonstrated the ability to stimulate deeper into the brain. Clever methods of manipulating applied fields might improve spatial resolution and depth in the future.

## 1.3 Hybrid methods

It is logical to briefly discuss methods that bridge the gap between invasive and noninvasive techniques. The most promising example is the use of nanoparticles to help localize electric field stimulation around target neurons. Nanoparticles have been explored for a variety of applications *in vivo* including cancer treatment and drug delivery [24, 25]. A

useful property of nanoparticles is their interactions with fields. Nanoparticles convert energy absorbed from a field into energy for cell stimulation (membrane depolarization). Nanoparticles composed of gold, polymer, semiconductors, and iron have been used to locally stimulate neurons [26]. For example, it is well-known that gold nanoparticles have plasmons that are capable of transducing infrared light into thermal energy. Gold nanoparticles that are bound on target cells can then locally activate thermally-activated ion channels to induce cell depolarization [27]. Magnetic nanoparticles, such as iron oxides, can similarly stimulate cells but instead use magnetic fields [28]. Semiconductor nanoparticles have potential to both record and stimulate neurons due to their photocurrent properties [29, 30]. Nanoparticles can facilitate localized stimulation of individual cells but are less invasive than implanted electrodes. However, the success of this technique depends on the ability to deliver and localize nanoparticles to target cells in the brain. Nanoparticle delivery through the blood brain barrier is a challenge [31, 32], let alone neuron targeting. Additional research also needs to assess long-term health effects of nanoparticles *in vivo*. The concept of localized nanoparticle stimulation is nonetheless very promising since it avoids many of the biggest challenges faced by implanted electrodes.

## 1.4 Invasive methods

Tissue-implanted electrodes are currently the standard for deep brain stimulation treatments for brain dysfunctions such as Parkinson's disease. Voltage or current stimulus pulses applied to implanted electrodes generate localized electric fields to stimulate cells in close proximity to the electrode surface. This method is currently the most feasible for deep brain stimulation because the electrode is placed near the targeted region in the brain. In contrast to NIBS, the close proximity of the stimulation source decreases the distance that fields need to penetrate to reach their target. However, the physiological tissue environment is hostile. Human brain tissue is extremely sensitive to foreign materials and unnatural trauma (e.g. electrode implantation). The number of constraints imposed on the stimulation source

for compatibility in the tissue environment are numerous and inter-dependent. The following discussion will focus on implanted electrodes for cell stimulation. Implanted recording electrodes are only briefly discussed because they share many of the same challenges that stimulation electrodes face due to implantation and interactions with living tissue. Recording electrodes are also relevant since current research is trending towards multifunctional electrodes capable of both recording and stimulating neurons for close-loop bioelectrical interfaces.

### 1.4.1 Recording

The major difference between recording and stimulation electrodes is that recording electrodes are passive. Recording is achieved by placing an electrochemically sensitive electrode surface near a target cell. When the target cell undergoes an action potential, the extracellular and intracellular ion concentrations rapidly change ( $<$ 1 ms for neurons and $>$ 100 ms for cardiomyocytes). Changes in ion concentration shift the electrochemical potential at the recording site interface, which induces a small current signal in the recording electrode. Current signals are then amplified and converted to voltage readings that correspond to electrochemical potential measurements either inside or outside of the cell. Perhaps the most important parameter for designing recording electrodes is their electrical and electrochemical impedance. Recording electrodes with a lower impedance are preferred because the measured voltage signal is attenuated by high impedance, which is dictated by Ohm's Law for alternating current (AC) circuits:

$$V(\Omega, t) = Z(\Omega, t)I(\Omega, t) \tag{1.4}$$

where $V$ is the electrical voltage, $\Omega$ is the frequency of a sinusoidal stimulus, $t$ is time, $Z$ is the electrical impedance, and $I$ is electrical current. Higher impedance values decrease the measured voltage signal leading to a reduced signal-to-noise ratio (SNR). Noise is a

significant issue since extracellular potential measurements can be as low as a few μV for an action potential. Therefore, the total impedance is usually reported as the metric for effective recording electrodes. Total impedance not only consists of electronic resistance of the electrode, but also surface impedance at the electrode-electrolyte interface. Surface impedance can be improved (decreased) by using alternative surface materials and increasing electrode surface area. More on surface impedance will be discussed later. SNR can also be improved by placing recording electrode sites as close to the membrane of the target cell as possible. Some electrode designs have incorporated lipid layers to achieve transmembrane placement, which is the ideal configuration for high SNR measurements [4, 5, 33, 34]. However, these designs typically require complex fabrication methods and are not yet practical for *in vivo* implementation.

### 1.4.2 Stimulation

Recording electrodes are constrained by total electrical impedance and their ability to be placed in close proximity to the cell of interest. The same constraints apply to stimulation electrodes. Many of the challenges faced by recording electrodes are also faced by stimulating electrodes due to the effects of implantation trauma and the hostile biological environment. However, these challenges are amplified for stimulation electrodes since they are electrically driven devices. Electrochemical stimulation continually perturbs the biological environment and is always irreversible to some extent. This inherently exacerbates the tissue response and leads to chronic stability issues. The biocompatibility obstacles and design constraints will now be discussed in detail for stimulation electrodes.

### 1.4.3 Current FDA approved devices

Deep brain stimulation (DBS) has been approved for treating essential tremors, Parkinson's disease, obsessive-compulsive disorder, and dystonia [35, 36]. There are only a handful of companies with FDA approved electrode leads for DBS in the United States: Medtronic,

Aleva, Boston Scientific, and St. Jude Medical. Each of their devices are very similar in design due to the long and expensive approval requirements (See review: [37]). Implanted leads are cylindrical with diameters between 1 and 2 mm and have upwards of two dozen electrodes with dimensions ranging from 0.66 – 1.5 mm. For Parkinson's disease, these electrodes are inserted in the basal ganglia over the prefrontal cortex, which is relatively deep inside of the brain. The placement of these electrodes is critical for their effectiveness but proves to be a difficult task [38]. Surgical techniques as well as electrode lead design have evolved to improve the process or allow greater error while maintaining effective performance [39]. Once leads are surgically placed inside of the brain, along with their battery power supply, electrical stimulation parameters are tuned (e.g. current, frequency) to maximize therapeutic effects and minimize side effects (e.g. blurred vision, headaches) [40]. Side effects may be a result of unnecessarily stimulating nearby cells that may have no effect on tremors, presumably due to the relatively large size of current DBS leads. The estimated volume of the average human brain is $\sim$ 1,000,000 $mm^3$, or about 100,000 neurons per $mm^3$ [1, 41]. There are then $\sim$ 10,000 neurons in a 100 $\mu$m slice with an area of 1 $mm^2$. Therefore, the smallest electrode currently used for DBS at this time ($\sim$ 1.66 $mm^2$) stimulates $\sim$ 20,000 neurons simultaneously. Furthermore, experiments in mice have shown that even a single neuron can affect behavior [21]. There has also been an ongoing debate about the exact mechanism by which DBS even yields therapeutic results [42]. Furthermore, there are many questions still unanswered about which cells to target; the specific neurons or circuits responsible for brain dysfunctions is still unknown. Smaller electrodes that can better localize stimulus is needed to maximize therapeutic benefits and minimize side effects. Smaller electrodes would also facilitate research studies on which cells or circuits lead to dysfunctional brains.

### 1.4.4 Research for improved DBS

Current DBS electrodes are very simple in design but still suffer from complications. Artificial pacemakers implanted in human hearts have been used for far longer than DBS electrodes ($\sim$ 60 years compared to $\sim$ 20 years) [43, 44]. A study in 2012 showed that in a span of 5.8 years, almost 10% of patients with artificial pacemakers experienced problems that were mostly caused by the electrode leads [45]. The exact modes of failure and complications in pacemakers are only recently being identified [46]. Surprisingly, only about 5% of patients with implanted DBS electrodes experience electrode complications [47], but complication and failure rates can be much higher depending on what diseases are being treated [48]. Side effects are also very common with a rate up to $\sim$ 86 % in one study [49]. On average, patients experienced 3.5 adverse effects with the most common being related to gait and speech [49]. The excessive number of side effects and failure rates of implanted electrodes have motivated the development of new electrodes that are smaller, less-invasive, safer, and ultimately more effective for DBS patients. Additionally, an electrode scheme that can target individual neurons on a large scale can facilitate our understanding of both functional and dysfunctional brains.

### *1.4.4 Specificity*

Specificity is how well an electrode can localize stimulation fields to a target cell. Patch clamping is the gold standard for single cell potential studies [50]. A sharp glass pipette filled with solution is used to gain intracellular access enabling singe cell stimulation and recording. Briefly, a sharp glass pipette is filled with intracellular solution and contains a Ag/AgCl electrode that is wired to a high-precision amplifier. The pipette is lowered to the cell membrane while a small positive pressure is applied to the tip to prevent debris from clogging the tip. The electrical resistance of the pipette is monitored at all times and is generally between 2 – 10 M$\Omega$ in free solution. The pipette is positioned near the cell membrane using a micromanipulator until an increase in resistance is observed near the cell, which in-

dicates that the membrane is located at a sufficiently close distance to the glass pipette tip. The pipette pressure is switched to atmospheric pressure, which causes the membrane to seal the pipette tip. Resistance increases as the cell membrane is sucked up into the pipette until a gigaseal forms (i.e. pipette resistance $> 1$ G$\Omega$). A short negative pressure pulse is then applied to breach the cell membrane and gain intracellular access. The Ag/AgCl electrode in the glass pipette injects current to maintain either a constant cell membrane potential (voltage clamp) or current (current clamp). At this point, membrane potentials can be measured with unprecedented signal-to-noise ratios. This method can be used *in vitro* and *in vivo* [51, 52]. Recently, automatic patch clamp robots have been developed to improve throughput and speed of experiments [53, 54]. The patch clamping method is by far the most sensitive and selective single cell electrode available. However, patch clamping is limited by mechanical vibration, which restricts studies to only 1 – 2 hours. Additionally, patch clamping is only reliable *in vivo* when the animal subject is anesthetized, although clever schemes have made experiments in free-moving animals possible [55]. Also, the number of pipettes that can be inserted into the brain is physically limited by spatial constraints. Lastly, patch clamping is not a feasible method for human treatment or studies. Innovative intracellular probes have been developed that exhibit the same cell selectivity and signal-to-noise ratio as patch clamping, but their rigid and complex structures limit their feasibility for practical applications [4, 5, 33, 34].

### *1.4.4 Throughput*

There is a need for an array of electrodes that can interact with several individual cells independently to understand the role of cell circuits in the brain and effectively target only the cells responsible for brain dysfunctions. Beyond the brain, cochlear implants and visual prostheses designs are also working towards better electrode spatial resolution for localizing cellular stimulation [56]. The first step towards a higher throughput cell stimulation was the microelectrode array (MEA) which emerged in a 3D form in 1991 [57]. Since

then, MEAs have been used extensively in animal studies. The two most prominent types of MEAs are the Utah array and the Michigan probe [58, 59]. The Utah array consists of several electrode pillars equally spaced in a square matrix [58]. Modern Utah arrays have insulated pillars with exposed tips. The advantage of this type of array is the improved planar area in which electrodes can interact with cells. The disadvantage is that the Utah array can only achieve a depth as far as the length of each pillar, which is limited by microfabrication processes (typical aspect ratio limit is $\sim 40$). The Michigan probe increased the depth at which multiple electrode channels could interact with cells and resembles current electrodes used for DBS [59, 60]. A substantial number of studies have since investigated microelectrode arrays to improve signal throughput and selectivity [61–67]. A comprehensive review was recently published by Obien et. al. [68]. Nearly all MEA designs rely on microfabrication, which is limited to very stiff materials such as silicon and metals. Neural tissue, on the other hand, is soft and dynamic. Mechanically rigid electrode materials have been shown to induce internal bleeding and elicit an immune response upon implantation [69, 70]. Tissue damage during electrode implantation procedures (especially large electrodes) lead to poor chronic stability. Breeching the blood brain barrier during implantation causes adverse reactions that lead to the formation of scar tissue, which acts as an electrically insulating barrier at the biological/electrode interface [69, 70]. Studies *in vitro* still benefit greatly from advancing MEA technology [71]. State-of-the-art MEAs have demonstrated as many as 60,000 electrodes, stimulation sites as small as 10 μm, and pitch spacing as low as 18 μm [72–74]. Complementary metal oxide semiconductor (CMOS) technology has only recently become available commercially offering arrays with over 16,000 electrodes for *in vitro* cell studies [75].

### *1.4.4 Biocompatibility*

Biocompatibility is a broad term that encompasses many possible interactions of an implant with biological tissue. The primary goals of achieving biocompatibility in the context

of stimulation electrodes are to minimize biological interference (e.g. cell death, cell displacement, immune response) and to maintain efficacy of the implanted device (e.g. close proximity to cells, low excitation thresholds). Biocompatibility of electrodes depends on their chemical, mechanical, and electrochemical properties.

**Mechanical**

The effects of electrode mechanical properties on cells and tissue can be separated into static and dynamic interactions. It is well known that cells respond to static stiffness [76, 77]. The relevant parameter most often reported for static stiffness is elastic modulus (aka Young's modulus). Brain tissue has an elastic modulus between 1-10 kPa. Most electrode materials have an elastic modulus greater than 1 GPa [78]. This difference in static elastic stiffness has been shown to induce changes in cell phenotype, which may cause neurons to lose their function [76]. Young's modulus is not likely the best indicator for biocompatible mechanical properties since force is really the parameter that cells "sense" [79, 80]. A lower Young's modulus does, however, mean that microstructure will apply a lower force for a given set of dimensions. Cell forces range from 1 to 100 pN [81]. The effects of static stiffness are difficult to delineate from dynamic interactions *in vivo* since dynamic interactions are nearly unavoidable. Nonetheless, there is a recent increase of research into flexible electrodes arrays to minimize the host response due to contact with stiff materials [82]. One of the earliest designs was composed of an array of flexible parylene electrodes with gold contacts to improve chronic stability hindered by micromotion [83]. Prof. John Rogers et. al. have made substantial progress more recently in creating flexible and biodegradable electronics. The main disadvantages of these devices is a lack of spatial resolution since they are usually made of relatively large 2-dimensional gold electrodes [84]. The fabrication approach also limits electrode arrays to planar arrangements, but more recent developments include implanting deeper, dissolvable electrode arrays [85].

One problem with flexible electrodes is that they are difficult to implant since their flexibility prevents tissue penetration. Injectable electronics is the latest advancement in

implantable, flexible electronics [86]. These electrode schemes have been shown to have excellent chronic stability *in vivo* and was attributed to their flexible architecture [82]. This recent demonstration shows benefits of lower static mechanical stiffness but does not prove that it is required *in vivo*. Although, *in vitro* studies do prove that forces exerted on cells definitely impacts the cell [76, 79, 80]. Research has also shown that flexible electrodes do not entirely prevent adverse tissue reactions [87]. Dynamic mechanical interactions also need to be addressed.

Dynamic mechanical interactions originate from two dynamic events: tissue implantation processes and micromotion. Implanting electrodes into tissue, especially large electrodes composed of rigid materials, can cause cell displacement and breeches of the blood brain barrier by severing vessels [69, 70]. The trauma experience by the tissue can elicit an immune response, lead to gliosis, and ultimately, scar tissue formation [88, 89]. Once a scar tissue forms around an electrode implant, it acts as an electrically insulated barrier and diminishes signal integrity and the ability to stimulate cells. Injectable electronics may be able to circumvent this issue, but not all electrode schemes are necessarily injectable. One group recently tethered flexible electrodes to a rigid shuttle for implantation [90]. Once implanted, the shuttle can be removed by breaking the tether. Tissue damage did occur from penetration by the shuttle, but results showed that the tissue was able to full recover from implantation trauma and enabled superior chronic stability. Additional flexible electrodes were then able to be implanted into different regions of the same brain. These results indicate that tissue damage may not need to be entirely avoided as long as the delivered electrode is flexible and small enough to minimize its own biological response.

Micromotion occurs after implantation and is caused by mechanical movement of the brain or the electrode itself (due to external wiring). Movement of the electrode not only changes the proximity of electrode sites to target cells but also displaces tissue causing damage [91, 92]. Electrodes with higher flexibility have been shown to minimize damage due to micromotion [82].

One way to circumvent implantation entirely is to use wireless electrode schemes [93]. Wireless arrangements eliminate the need to connect electrodes to external electronics, and thus, eliminating micromotion and circumventing the risk for infection at the implant entry point [94]. The most difficult limitation for wireless schemes is the electrical power supply. Current technology for batteries and power transmission requires batters to be implanted as well, which complicates surgical procedures, especially considering their relatively short lifespan [95]. Wireless power transfer technology makes it possible to eliminate the need for a large battery or a battery at all, but needs significant improvement with respect to efficiency. For this reason, most wireless stimulation schemes have initially been focused on optogenetic methods since LEDs require little power [96–99].

**Chemical**

Delineating the different contributions of individual material properties to observed cell or tissue responses is difficult since multiple biological signaling pathways can be activated or suppressed simultaneously. Cell viability is also not clearly defined. Cells can undergo phenotypic changes but still appear to be ”healthy.” Many biocompatibility results for materials are inconsistent as a consequence, such as carbon nanotubes [100–103]. The biocompatibility of a material can also depend on whether it leeches into tissue, which may also be exacerbated by stimulation pulses. Kozai et. al. compiled a comprehensive review on neural interfacial materials [2].

Absolute biocompatibility may be difficult to ”measure,” but a significant amount of research has investigated ways of improving biocompatibility. The most common way is by incorporating biomolecules or anti-inflammatory agents into the electrode interface [89, 104]. Conductive polymers are particularly attractive because their polymerization process is conducive to the incorporation of therapeutic biomolecules [105, 106]. Conductive polymers have also demonstrated the ability to controllably release anti-inflammatory drugs with electrical stimulation [107]. Biomolecule incorporation has shown to decrease adverse reactions and improve chronic stability of electrodes [106, 108]. Some groups have

alternatively attempted to avoid the electrode-tissue interface entirely through tissue engineering. Green et. al. has worked on using encapsulated neurons as the mediation layer to stimulate other neurons [109]. The approach circumvents the uncertain tissue response to an electrode by developing a stable cell-electrode interface prior to implantation. This method is still relatively new but has shown promise.

**Electrochemical**

Many problems with the chronic stability of electrodes is due to the electrochemical transduction from electron current to ionic current during stimulation pulses. Repeated stimulation pulses have two adverse effects: electrode degradation and tissue damage. Electrode degradation occurs when irreversible electrochemical changes change the chemical makeup of the electrode surface. Degradation is more rapid when Faradaic currents are used as opposed to capacitive (non-Faradic) currents. Faradaic currents involve charge transfer across the electrode-electrolyte interface to species able to diffuse in solution. This charage transfer process is not fully reversible and leads to permanent changes to the electrode site [110, 111].

Tissue damage or cell death can occur if excessive voltages or currents are applied at the electrode interface. High voltage potentials at the electrode lead to electrolysis, which locally changes the pH in tissue [112]. A review of literature shows that a specific damage threshold for electrodes in tissue is very difficult to pinpoint [113]. One of the first attempts at defining a damage threshold for stimulation was the Shannon equation [114]:

$$log(D) = k - log(Q) \tag{1.5}$$

where $D$ is the charge density, $Q$ is the charge per phase for stimulation, and $k$ is an adjustable parameter between 1.5 and 2. As pointed out by Cogan et. al., this equation does not take into account frequency, pulse width, current density, or the size of electrode [113]. The typical allowable charge density limit reported is 30 $\mu$C cm$^{-2}$. This value of charge

density originates from FDA approval of the first DBS electrode [115]. However, studies have shown tissue damage to occur at higher and lower thresholds [114, 116]. Interestingly, microelectrodes seem to have their own safe charge limits [113]. Future works needs to more clearly define tissue or cell damage and develop better models to predict maximum stimulation parameters. Safe stimulation will become increasing important as electrodes decrease in size and chronic stability is improved. As electrodes become smaller and more intimately connected to cells, electroporation may be a more specific indicator of unsafe stimulation levels [117].

### *1.4.4 Alternative stimulus methods*

Optogenetics is the most promising alternative to direct electrode induced cell stimulation. Optogenetics allows controllable and reversible depolarization by incorporating light-gated ion channels (rhodopsin derivatives) [118]. The drawbacks of optogenetics include the difficulty in selectively introducing rhodopsin to specific neurons and the need for localized light sources for stimulation. Perhaps more importantly, genetic modification is required, which poses ethical concerns for applications in humans [119]. Nonetheless, optogenetics is already being tested in humans for visual prosthesis applications by first using natural light excitation [120].

### 1.4.5 Summary

Current neural stimulation technology has demonstrated cellular stimulation using extracellular and intracellular electrodes. Patch clamping is the gold standard technique for intracellular recording and stimulation of action potentials [54]. Patching clamping is not practical beyond research applications since it is low-throughput and requires the insertion of a hollow glass pipette through the craniotomy. Extracellular electrodes are far easier to implement and have higher throughput, which has made them one of the few successful devices currently used in clinical applications [121, 122]. But, extracellular electrodes lack

the cell selectivity and high signal-to-noise ratio offered by intracellular electrodes.

Electrode design requirements are vast but can be simplified into two general categories: shape and material. The unanimous approach for engineering the ideal electrode is to make electrodes smaller. Scaling laws have favorable impacts on material stiffness, selectivity, and biocompatibility [123, 124]. Engineering micro and nanoelectrodes with controllable shape and morphology for neural stimulation is limited by the extent of current nanofabrication capabilties. Carbon nanotubes (CNTs) are one of the more popular nanomaterials because of their high-conductivity and large aspect ratio [123]. However, CNTs are mechanically rigid, relatively short, difficult to spatially manipulate, and must be grown in bulk with uniform properties (i.e. individual CNTs cannot be customized). An alternative micro or nanomaterial is needed to satisfy these requirements.

## 1.5 Conductive polymer wires

### 1.5.1 PEDOT:PSS polymer

Currently approved implantable leads for DBS use platinum electrodes. Platinum is a rigid material and how low electrochemical performance compared to other materials. Other materials that are softer and have lower electrochemical surface impedance may improve biocompatibility, lower stimulus thresholds, and even extend battery life [125]. Conductive polymers are an interesting class of materials because of their low Young's modulus, low surface impedance, and ability to conduct electric current [126]. One of the more popular conductive polymers is poly(ethylene-dioxythiophene) (PEDOT), which is often coupled with a poly(styrenesulfonate) (PSS) counterion to form the PEDOT:PSS polyelectrolyte complex (Figure 1.3). This particular conductive polymer is popular because it is water processable (i.e. does not require organic solvents during deposition) and has a relatively high conductivity compared to other polymers. Thin layers of PEDOT:PSS have been found to be transparent but also exhibit electrochromic properties with an applied voltage [127]. Commercial uses for PEDOT:PSS include anti-static coatings, solar cells, and flexi-

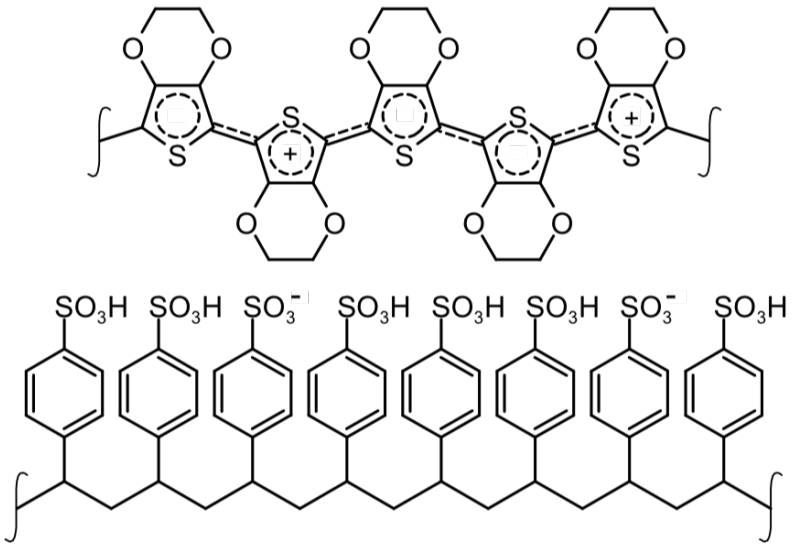


**Figure 1.3:** Chemical structure of poly(ethylene-dioxythiophene) (PEDOT) electrostatically-coupled to the poly(styrenesulfonate) (PSS) counterion to form PEDOT:PSS.

ble electrochromic displays. These applications take advantage of the optical, mechanical, and electrical properties of PEDOT:PSS, but, as noted, this polymer also has remarkable electrochemical properties [123, 128–130]. PEDOT:PSS in particular has demonstrated one of the highest charge storage densities determined for a material [131], which makes it ideal for super capacitors and, as discussed here, bioelectrode materials.

The high charge density of PEDOT:PSS is not fully understood but is thought to originate from the mechanism by which it transduces electronic to ionic charge [132–134]. PEDOT:PSS conducts electric current by hole conduction, which is the transport of delocalized positive charges, which are called polarons. The holes in PEDOT form via over-oxidation during chemical or electrochemical polymerization. There are varying degrees of over-oxidation that can either yield polars or biopolars (the latter is more conductive) [126]. The process of over-oxidation to enable conductivity is called doping. The excess positive charge in PEDOT is stabilized by a counterion, which is most commonly, but not limited to, PSS. When PEDOT:PSS is used at an electrode/electrolyte interface, an applied voltage can reversibly dope PEDOT by adding or removing electrons. The polymer interacts with charged ions in solution depending on its doped state. A highly doped PEDOT state attracts negative ions from solution to compete with the negatively charged sulfonate groups on PSS. In a low or undoped state, PEDOT has an excess negative charge due to

the integrated PSS chain, which then attracts positive ions from solution. In this way a full sinusoidal or square wave potential can be applied to PEDOT:PSS to generate an alternating electric field by creating ion potential gradients at this interface. This mechanism gives PEDOT:PSS what is called pseudocapacitive charge injection properties, because it is not considered strictly capacitive, yet it demonstrates a high-degree of reversibility [135].

Charge injection is the process of converting electronic charge into ionic charge, which then creates electrochemical fields in solution to stimulate cells. A high charge injection density or capacity is typically correlated with a low surface impedance. There are two primary types of charge injection: Faradaic and capacitive. Capacitive charge injection occurs from the build up of the electric double layer ions at the electrode/electrolyte interface. These ions attempt to cancel the electric field generated by the excess or deficiency of electrons at an electrode surface. Capacitive charge injection is by far the most preferred method to generate electric fields in solution because it is reversible and does not require any electrochemical reactions that can degrade the electrode material. The electric double layer is unfortunately very small (nanometers in thickness) and may not generate sufficient current with micro and nanoelectrodes capable of electrical stimulation of cells. Faradaic current is avoided if possible; these currents are irreversible since they involved the transfer of electrodes from the surface to ionic species in solution that then freely diffuse away. Over time, Faradaic currents (e.g. electrolysis) contribute to the degradation of the electrode surface and diminishes its ability to transfer charge and generate fields. In addition, Faradaic currents inherently generate local pH changes in the surrounding solution, which is destructive in a cell or tissue environment. Pseudocapacitive currents arise from electrochemical reactions of surface-bound species. Typically materials that exhibit pseudocapacitance are metal oxides that change oxidation states [136]. Examples include $RuO_2$ and $MnO_2$. This process is reversible, much like the reversible doping of PEDOT:PSS. This type of charge injection is biocompatible because it minimizes local pH changes within the acceptable potential window and does not degrade the electrode as quickly [131].

By combining the high charge injection property of PEDOT:PSS with its ability to form to high surface area nanostructures, exceptionally high charge injection values have been obtained. Some of the highest charge injection values currently reported in literature were obtained by coating an array of carbon nanotubes with PEDOT:PSS (1.21-15 mC $cm^{-2}$) [128, 129, 131, 137–139]. The long-term viability of cells on surfaces with charge densities of these magnitudes is uncertain [113]. Nonetheless, the high charge density of PEDOT:PSS has made microelectrodes more feasible and has recently been demonstrated for microelectrodes as small as 15 μm in diameter to stimulate cells [140, 141]. Additionally, conductive polymers can be chemically functionalized [142, 143], which gives the potential for their integration with multiple substrates and cell types (e.g. neurons, muscle cells, cardiomyocytes, etc.). PEDOT:PSS is also attractive for its superior biocompatibility [66, 140, 144–147].

PEDOT:PSS has exceptional electrochemical properties, but its electronic conductivity is no where near that of metals (Table 1.1 [148]). PEDOT:PSS films have demonstrated conductivities with an upper limit near 5,000 S $cm^{-1}$ whereas gold has a conductivity over 400,000 S $cm^{-1}$ [149]. The conductivity of electropolymerized PEDOT:PSS wires is even lower ( $< 50$ S $cm^{-1}$) [150]. It is worth noting that films are often dropcast and not electrochemically polymerized. Dropcast films have shown an increase in conductivity by several orders of magnitude using post processing techniques such as exposure to solvents or electric fields [151–155]. Superb charge storage and relatively poor electrical conductivity are the reasons that conductive polymers are almost always employed as films. However, the relatively low modulus of PEDOT:PSS ($\sim$1 – 3 GPa vs $\sim$80 GPa for gold) could provide a balance between conductivity and mechanical flexibility for bioelectrode applications.

### 1.5.2 Polymer wire synthesis

A method to grow polymer nanowires was first developed by Prof. Bret Flanders et. al. at Kansas State University [156–160]. This technique allows *in situ* growth of single polymer

**Table 1.1:** Comparison of material properties for common electrode materials.

| Material | Young's modulus (GPa) | Electrical conductivity (S $cm^{-1}$) | Charge density (mC $cm^{-2}$) |
|---|---|---|---|
| LDPE | 0.25 | $10^{-16}$ | |
| PEDOT:PSS | 1 – 2 | 38 | 1 – 15 |
| Gold | 80 | 400,000 | 0.01 |
| N-Silicon | 160 | 100 | |
| Platinum | 170 | 100,000 | 0.15 |
| CNT | 270 | 800,000 | 3 |

nanowires from gold nanoelectrodes that can interface with individual cells. The process is induced by the application of an alternating electric field between two sharp gold electrodes. The alternating field promotes polymerization at the location of highest electric field (electrode tip). The diameter of wires is controlled by adjusting the frequency, where a higher frequency yields smaller diameter wires. The length of the wires is only limited by the amplitude of the applied alternating voltage, which decreases with length due to the increasing series resistance along the wire. The original technique was developed for wires below 1 μm, but wires with diameters several micrometers in diameter have recently been demonstrated [150]. The advantage of growing these polymer wires is the ability to form high aspect ratio structures that current microfabrication techniques cannot achieve. High aspect ratio greatly lowers the bending modulus. Using classical beam theory, the maximum deflection due to a force at the end of a cantilever beam is given by:

$$\delta = \frac{PL^3}{3I} \tag{1.6}$$

where $\delta$ is deflection, $P$ is force applied at the end of the beam, $L$ is the length of the beam, and $I$ is the moment of inertia, which depends on the cross-sectional shape and area. Therefore, for a given cross-section, the force required to bend a beam decreases with $L^3$. It is well known that cells respond to the mechanical properties of their environment [76, 77,

161]. Cell forces range from 1 to 100 pN [81]. A high aspect ratio structure could enable the possibility of attaching wires to cells without harming the cell or physically disrupting the cell membrane. Flexible polymer wire attachment to cells could also eliminate mechanical trauma due to micromotion, which is a current issue in implantable deep brain stimulation (DBS) electrodes [91, 162]. Nanowire attachment to cells would also decrease the distance between the electrode and the cell membrane thereby decreasing the magnitude of applied voltage needed for stimulation and improving impedance stability [163, 164]. Glial cell encapsulation isolates electrodes from neurons and occurs due to electrode insertion trauma [70]. The high aspect ratio of polymer wires could potentially maintain electrical contact with cells beyond the encapsulation layer. Thus, wires composed entirely of polymer could hold promise for solving bioelectrode issues that have yet to be addressed.

Emerging technologies have aimed to scale down electrodes to improve selectivity and throughput of neuron stimulation. Improvements in these areas often come at the cost of higher electrical impedance (i.e. lower signal-to-noise) stemming from poor chronic stability and small surface area. Electrodes capable of individual stimulation of multiple cells simultaneously will require an interfacial nanomaterial with a low surface impedance, precise spatial-selectivity, mechanical flexibility, chronic stability, and excellent biocompatibility. The following provides foundational research for the investigation of using conductive polymer wires to selectively stimulate individual cells.

# CHAPTER 2
# CONDUCTING POLYMER NANOWIRES FOR CONTROLLING LOCAL PROTEIN CONCENTRATION IN SOLUTION

The following was published in the Journal of Physics D: Applied Physics, Volume 50, Issue 17 [165] and is reproduced here with permission from IOP Publishing.

J. D. Morris*, S. B. Thourson*, K. Panta, B. N. Flanders, and C. K. Payne, "Conducting polymer nanowires for control of local protein concentration in solution". In: Journal of Physics D-Applied Physics 50 (2017). *These authors contributed equally.

## 2.1 Overview

Interfacing devices with cells and tissues requires new nanoscale tools that are both flexible and electrically active. We demonstrate the use of PEDOT:PSS conducting polymer nanowires for the local control of protein concentration in water and biological media. We use fluorescence microscopy to compare localization of serum albumin in response to electric fields generated by narrow (760 nm) and wide (1.5 μm) nanowires. We show that proteins in deionized water can be manipulated over a surprisingly large micron length scale and that this distance is a function of nanowire diameter. In addition, white noise can be introduced during the electrochemical synthesis of the nanowire to induce branches into the nanowire allowing a single device to control multiple nanowires. An analysis of growth speed and current density suggests that branching is due to the Mullins-Sekerka instability, ultimately controlled by the roughness of the nanowire surface. These small, flexible, conductive, and biologically compatible PEDOT:PSS nanowires provide a new tool for the

electrical control of biological systems.

## 2.2 Introduction

The basic components of biological systems are small, ranging from nanometer-scale proteins to micron-sized cells, and soft. For example, the Young's modulus of neural tissue is 100 kPa – 1000 kPa [166, 167]. The small size and soft materials of human biology provide a challenge for the use of implantable bioelectric devices such as neural electrodes [62, 92, 161, 168]. The mismatch between the stiffness of implanted materials and the softness of cells and tissues leads to cellular damage and elicits an immune response. Soft materials, such as polymers and hydrogels, are more biocompatible with a Young's modulus comparable to tissue. However, materials used at the bioelectric interface need to be electrically conductive as well as small and flexible.

Electrically conductive polymer nanowires, described previously,[158–160] provide a small, flexible, electrically active material for the bioelectric interface. Poly(3,4-ethylenedioxythiophene):polystyrene sulfonate (PEDOT:PSS) nanowires are of specific interest due to the extensive characterization and known biocompatibility of PEDOT:PSS [169–174]. These nanowires have been electrochemically synthesized with average diameters of 340 nm, a Young's modulus of $\sim$2 GPa, and conductivity of $\sim$8.0 S cm$^{-1}$ [156, 158–160, 175]. Although the PEDOT:PSS nanowires are still stiffer than cells or tissue, they are two orders of magnitude more flexible than current state-of-the-art bundled carbon fiber neural electrodes with a diameter of 4.5 μm and a Young's modulus of 380 GPa [176].

Conducting polymer nanowires are promising tools for bioelectrical interfacing at cellular and subcellular scales. Previous work has demonstrated the use of conductive polymer films to control proteins in solution [177]. In this work, we demonstrate the use PEDOT:PSS nanowires, rather than bulk films, to control the local concentration of proteins in solution. We compare localization of charged proteins in response to electric fields generated by narrow (760 nm) and wide (1.5 μm) nanowires. We show that proteins in

deionized water can be manipulated over a surprisingly large micron length scale through the application of an electric field. We then compare this to an electric field applied in a high salt biological media, phosphate buffered saline (PBS). For future biological applications, which are likely to require multiple nanowires rather than a single nanowire, we demonstrate the synthesis of nanowires with controlled branching, allowing a single device to control multiple nanowires.

## 2.3 Materials and methods

### 2.3.1 Gold electrode fabrication

Conducting polymer nanowires were synthesized using directed electrochemical nanowire assembly in which nanowires are electropolymerized between two sharp gold electrodes [158–160]. Sharpened gold electrodes were fabricated by adapting methods used to etch scanning tunneling microscope electrodes [178]. Briefly, solid gold wire (0.2 mm diameter, 99.9%, Alfa Aesar, 10195-G1) was secured to 20 gauge stranded wire using parafilm. Gold wires were submersed $\sim$1 mm in high-concentration hydrochloric acid (6 M). Coiled platinum wire (0.3 mm diameter, 99.9%, Alfa Aesar, 43014-BU) served as the counter-electrode. A function generator (Agilent 33120A) provided a 10 Hz full square wave, $\pm$ 5 V amplitude. The square wave was rectified using a diode to deliver positive 5 V square pulses to the gold anode to initiate the reduction of gold into solution. Etching was terminated after $\sim$90 s to yield tip diameters $<$ 100 nm. After etching, electrodes were rinsed with ethanol, then water, and dried under nitrogen. Electrodes were plasma cleaned (Harrick) for 15 seconds before use.

### 2.3.2 Polymer wire growth

PEDOT:PSS nanowires were synthesized in an aqueous solution containing 10 mM 3,4-ethylenedioxythiophene (EDOT, Sigma-Aldrich, 483028) monomer and 20 mM polystyrene sulfonate (PSS, Sigma-Aldrich, 243051) as a counterion. PEDOT:PSS nanowires were

grown using a function generator (Agilent 33120A) supplying an alternating, square-wave voltage (2 – 100 kHz) across two sharp gold electrodes. The length of the nanowires is controlled by the spacing of the gold electrodes. The diameter of the nanowires is controlled by the frequency of the voltage used for the electrochemical synthesis. The wider nanowires (1.50 $\pm$ 0.55 μm diameter) were grown at 2 kHz and the thinner nanowires (760 $\pm$ 220 nm diameter) were grown at 10 kHz. Nanowire diameter was measured using a scanning electron microscope (SEM, Hitachi SU8230) and are the average of 4 different nanowires. Nanowire length was measured using brightfield microscopy (Olympus IX71, 60x objective, Andor iXon CCD camera). Nanowires were grown and imaged in a custom made flow cell to facilitate media exchange between the monomer solution and protein solution. Electrodes were spaced 50 μm apart (tip-to-tip). A -100 mV DC offset voltage was applied to promote PEDOT:PSS nanowire growth from a single electrode. The gap between the counter-electrode and the end of the growing nanowire was held constant by manually adjusting one of the micromanipulators. A Raman microscope (iHR550 Horriba-Jobin Yvon spectrometer fiber-coupled to a BX-41 Olympus microscope) was used to confirm nanowire composition.

### 2.3.3 Conductivity of PEDOT:PSS nanowires

The conductivity of the nanowire was determined using a two-point probe resistance measurement. A peristaltic pump was used to rinse the nanowire with 25 mL of deionized water to remove residual monomer. A 2 V, 10 kHz square wave was applied between the nanowire and the counter-electrode to fuse the nanowire across the electrodes. A Keithley 2400 source meter was controlled using a custom Igor Pro script to measure resistance. Voltage was swept between -1 and +1 V while measuring current. The resistance of the wire was determined by the inverse slope of the linear best fit line. Conductivity of the

nanowire was calculated using the formula:

$$\sigma = \frac{L}{AR} \tag{2.1}$$

where σ is conductivity (S $cm^{-1}$), $L$ is nanowire length, $A$ is nanowire cross-sectional area, and $R$ is electrical resistance.

### 2.3.4 Imaging protein concentration

To image protein localization, bovine serum albumin (BSA, Thermo Fischer Scientific, BP1600-100) was labeled with AlexaFluor546 (Thermo Fischer Scientific, A20002) according to the manufacturer's instructions. After the growth of a nanowire, the EDOT and PSS solution was exchanged for ultrapure deionized water (EASYpure II, Barnstead) or phosphate buffered saline (PBS, Gibco, 14040). Fluorescently-labeled BSA was then added to the solution. Fluorescence images were taken with an EMCCD camera (Andor iXon CCD camera) coupled to an inverted microscope (Olympus IX71, 40x objective). Profile plots where generated using Igor Pro's image processing package by taking the average over 25 pixel lines perpendicular to the nanowire.

## 2.4 Results and Discussion

### 2.4.1 Nanowire synthesis and electrical characterization

Nanowires provide a way to interface with cells or proteins on a relevant length scale. For example, using a nanowire to modulate cellular activity ensures only a single cell, rather than neighboring cells, are affected. PEDOT:PSS nanowires have been reported with diameter of $<$ 500 nm [158–160]. Within our lab, diameters of 500 nm to 1.5 μm are typical (Figure 2.1a and b). The length of the nanowire is controlled by the position of the two gold electrodes, typically 800 nm to 10 mm. Conductivity of the nanowires is measured with two-point probe resistance measurements. The average PEDOT:PSS nanowire con-

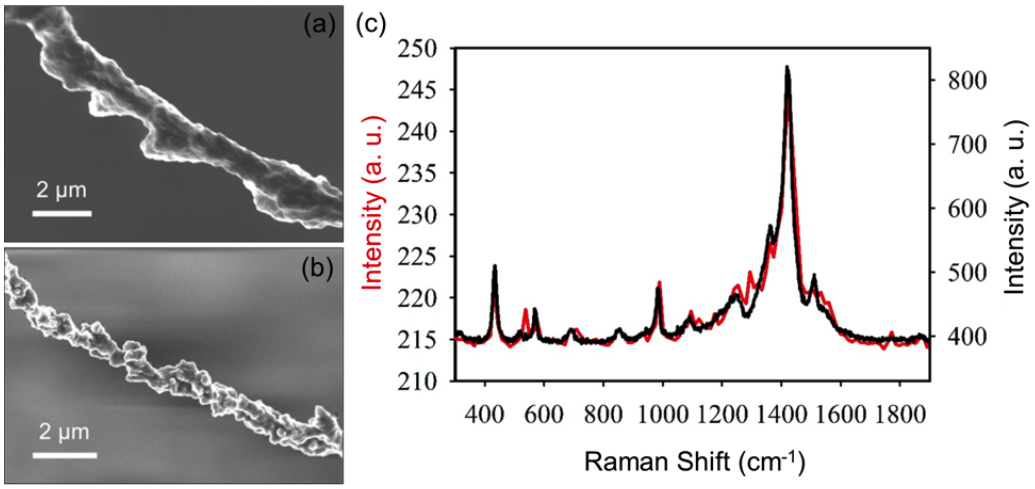


**Figure 2.1:** PEDOT:PSS nanowires. (a) SEM of a PEDOT:PSS nanowire grown with an AC frequency of 2 kHz. (b) SEM of a PEDOT:PSS nanowire grown with an AC frequency of 10 kHz. (c) Raman spectrum of a PEDOT:PSS nanowire (black) compared to a PEDOT:PSS film (red). SEM images were taken by S.B.T.

ductivity was found to be 24 $\pm$ 12 S cm$^{-1}$. On our size scales, conductivity was found to be independent of nanowire diameter and length. Nanowires composition was confirmed by comparing the Raman spectra of the nanowires with a PEDOT:PSS film (Figure 2.1c).

### 2.4.2 Using PEDOT:PSS nanowires to control local protein concentration

We first used relatively thick PEDOT:PSS nanowires with a diameter 1.5 μm (length = 25 μm) to control local protein concentration. Fluorescently-tagged BSA protein was added to solution after nanowire growth and an AC field (2 V, 1 Hz, square wave) was applied. Fluorescence intensity increased in the region of the PEDOT:PSS nanowire while a positive bias was applied (Figure 2.2a). A decrease in intensity was observed at negative biases (Figure 2.2b). This behavior is consistent with expectations given the net negative charge of BSA [179–181]. To observe the change in fluorescence around the nanowire, the intensity within a 25 μm x 10 μm box centered on nanowire was averaged for each frame of a short video (Figure 2.2c). An oscillation in fluorescence intensity was observed near the nanowire in response to the applied field (t = 4 seconds). To confirm that the oscillation in fluorescence intensity is due to the nanowire, and not the gold electrode, we took line profiles of the fluorescence intensity roughly 12 μm away from the gold electrode surface, similar to the distance used for the nanowire analysis (Figure 2.2). There was no significant

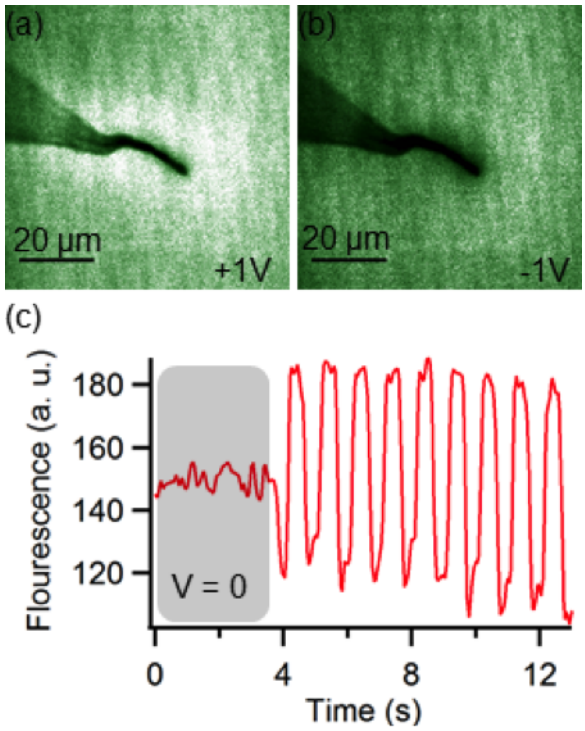


**Figure 2.2:** Fluorescence microscopy of a PEDOT:PSS nanowire with fluorescently-labeled BSA (∼100 nM) in the surrounding solution. The protein responds to an applied AC field (2 V, 1 Hz) from the nanowire. (a) Image of nanowire and protein (green); +1 V with respect to the gold counter-electrode. (b) Image of nanowire and protein (green); -1 V with respect to the gold counter-electrode. (c) Fluorescence intensity as a function of voltage in the region surrounding the PEDOT:PSS nanowire. Data was captured and analyzed by S.B.T. and J.D.M. and plotted by J.D.M.

change in fluorescence with changes in bias indicating that it is the PEDOT:PSS nanowire, not the gold electrode, responsible for altering the BSA concentration (Figure 2.3).

### 2.4.3 Comparison of protein control as a function of nanowire diameter

To determine the importance of nanowire diameter for controlling protein concentration, we repeated experiments using a thinner PEDOT:PSS nanowire with a diameter of 760 nm. In order to compare the local control of BSA, we took profile plots of fluorescence intensity as a function of distance centered on the nanowire (Figure 2.5). A positive bias shows less of a drop in fluorescence intensity at the nanowire compared to a negative bias due to an accumulation of BSA at the PEDOT:PSS nanowire surface.

The distance over which protein concentration was modulated was found to be 29.6 µm ± 8.6 µm and 16.7 µm ± 2.5 µm for the wide (d = 1.5 µm) and narrow (d = 760 nm) nanowires, respectively (Figure 2.5a and b). Averages and standard deviations were

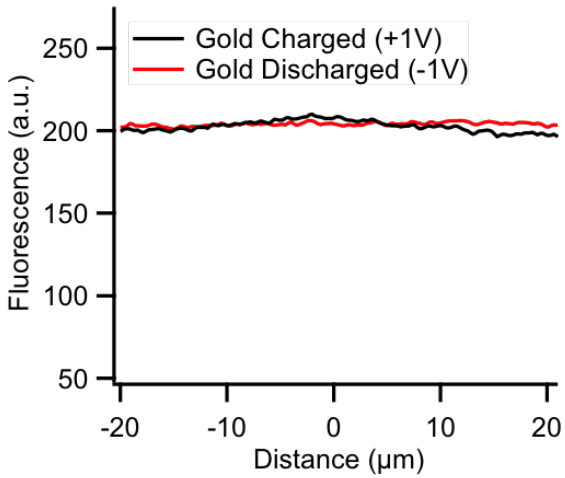


**Figure 2.3:** Fluorescence profiles (average of 25 line profiles) taken ∼12 μm away from the gold electrode surface at a positive (black) and negative bias (red). There is no significant change in fluorescence indicating that it is the PEDOT:PSS nanowire, and not the gold electrode, causing fluctuations in protein concentration. Data was captured and analyzed by S.B.T. and J.D.M. and plotted by J.D.M.

determined from measurements using three separate nanowires. The difference between the wide and narrow nanowires shows that altering the nanowire diameter allows the distance over which protein is manipulated to be tuned. It is important to note that under our experimental conditions a large number of factors that are difficult to control can alter the spatial extent over which protein is modulated. For example, slight changes in electrode geometry, changes in nanowire roughness or branching, variations in the contact resistance between the gold electrode and the nanowire, and the exact sharpness of the gold electrodes could all cause differences in the spatial extent of protein modulation. These variations are reflected in the relatively large standard deviations.

Regardless of these factors, the most surprising aspect of this result is the large distance over which protein is controlled for both nanowires. These distances are dramatically larger than the expected thickness of the electrostatic double layer at equilibrium, which is on the length scale of angstroms [163]. Previous reports have demonstrated ∼250 nm control of proteins using electric fields [182]. We show modulation of proteins over a length scale that is 100-fold greater. Conditions unique to our experiment which may alter the equilibrium thickness of the electrostatic double layer include the high curvature of the nanowire surface[183] and large counter ions (BSA) [184]. The curvature of the nanowires studied here, however, is below what is necessary to induce significant changes in the electrostatic

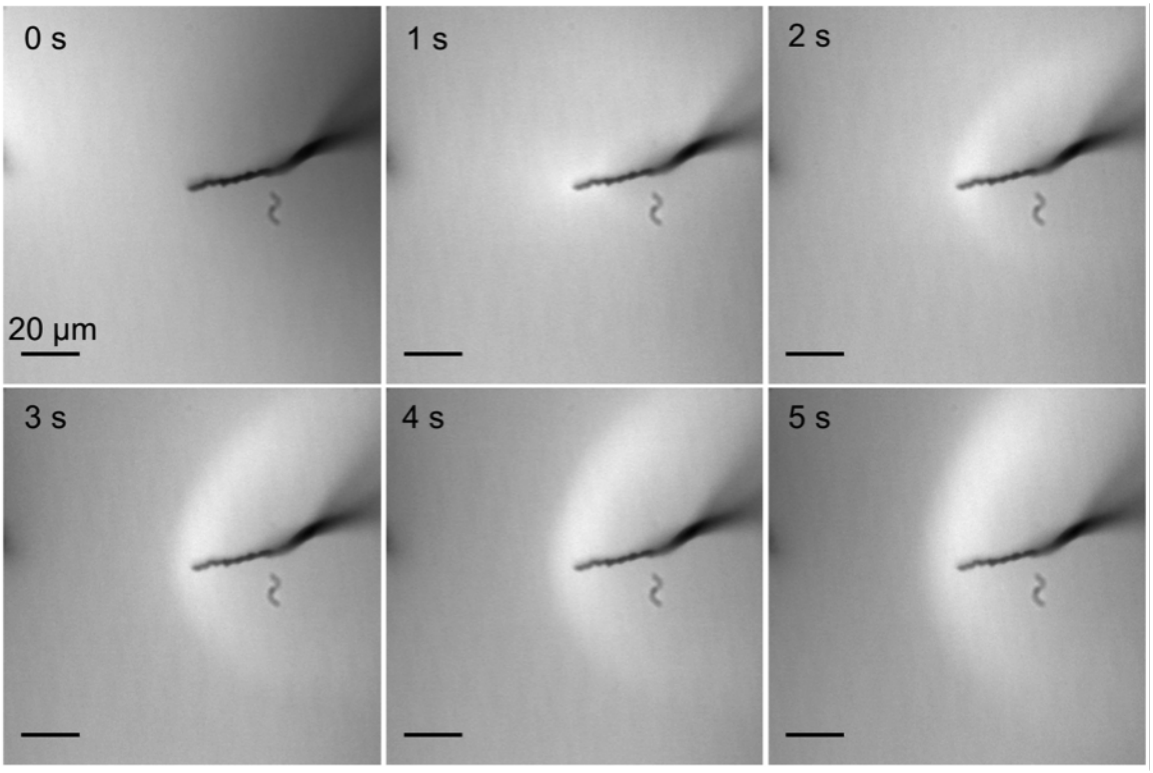


**Figure 2.4:** A sequence of fluorescence images of a 1.5 µm nanowire in the presence of BSA (300 nM) over 6 seconds. At t = 0 s the voltage on the nanowire switched to +1 V. Over this time frame additional BSA continues to accumulate around the nanowire. This shows that at the frequency in our experiments (1 Hz) the nanowire has not yet reached equilibrium. Image was plotted by J.D.M.

double layer [183]. The large size of BSA is expected to increase the equilibrium electrostatic double layer, but only out to a few nanometers. Instead, we suggest that our profiles are not at equilibrium. This is possible if the nanowire is charging in a regime controlled by bulk diffusion. These slow charging times allow for variation of the concentration of electrolytes over much larger distances [185]. Experiments at lower frequencies (50 mHz) show continued charging of the PEDOT:PSS nanowire, supporting this hypothesis (Figure 2.4).

We next quantified the amount of protein modulated for each diameter of nanowire. The relative quantity of protein modulated by the nanowire can be obtained by integrating the difference in area under the profiles at each bias. This integration indicates that the thin nanowire manipulates just 22.1% $\pm$ 7.3% of the quantity of protein displaced by the wider nanowire. At equilibrium, the small nanowire would be expected to store 50% less charge due to a 50% reduction in surface area. Since BSA acts as the negatively charged species in

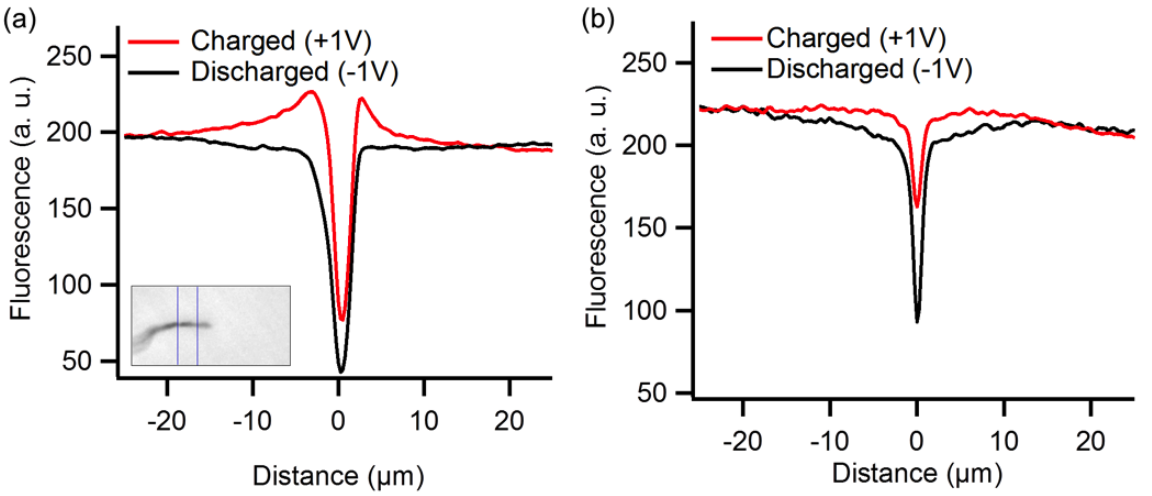


**Figure 2.5:** Profile plots of BSA concentration, measured as fluorescence intensity, as a function of nanowire diameter. (a) Charged (red, +1 V) and discharged (black, -1 V) PEDOT:PSS nanowire (d = 1.5 μm). The inset (50 μm x 25 μm) shows the cross section of the nanowire used to generate profile plots. Profile plots are generated from an average of 25 pixel lines perpendicular to the nanowire (b) Charged (red, +1 V) and discharged (black, -1 V) PEDOT:PSS nanowire (d = 760 nm). Data was captured and analyzed by S.B.T. and J.D.M. and plotted by J.D.M.

the electrostatic double layer, this decrease in charge storage will result in the manipulation of less BSA. At our frequency (1 Hz), however, the nanowires have not yet charged to equilibrium. This likely explains the deviation from the expected 50% reduction in charge storage. The increased quantity of protein manipulated by the larger nanowire highlights how altering the diameter of a PEDOT:PSS nanowire can provide the appropriate degree of charge storage for a desired application.

### 2.4.4 Comparison of protein control in water and biological media

The deionized water used in the experiments described above (Figures 2.2 and 2.5) provides an effective model environment for studying the modulation of proteins with PEDOT:PSS nanowires. The addition of salts is required for a more realistic biological environment. For this reason, we investigated the impact of biological media on the ability to control local protein concentration using PBS, a saline solution containing sodium chloride, potassium phosphate, and sodium phosphate. In a high concentration of electrolytes, the electrostatic double layer will be comprised primarily of salts instead of BSA. In this case we would expect the electrostatic double layer to be dramatically reduced. Similar to the experiments described above, we applied an AC field (2 V, 1 Hz, square wave) to a PEDOT:PSS

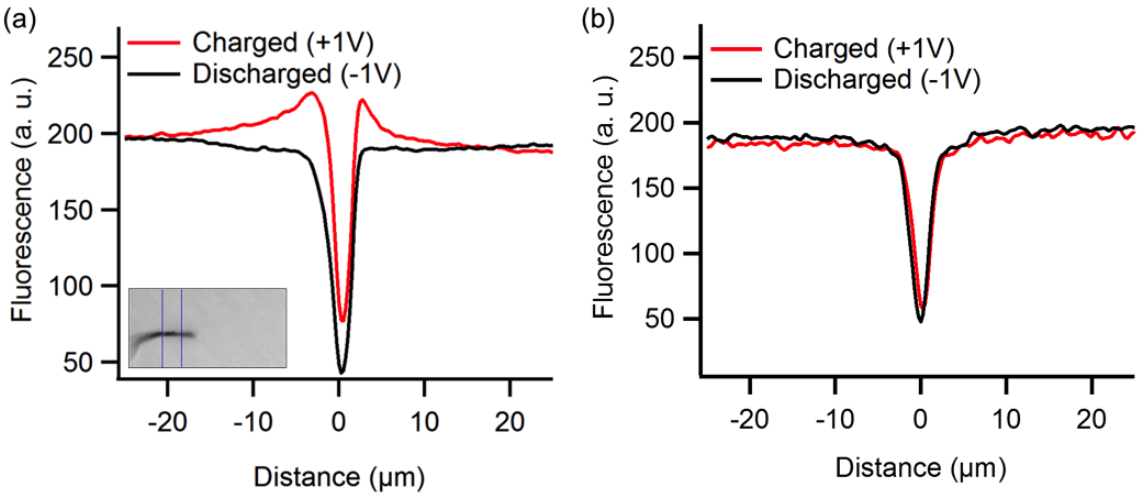


**Figure 2.6:** Profile plots of BSA concentration, measured as fluorescence intensity, centered around a PEDOT:PSS nanowire (d = 1.5 μm). (a) BSA in water (replotted from Figure 2.5a for comparison) charged (red, +1 V) and discharged (black, -1 V). The inset (50 μm x 25 μm) shows the cross section of the nanowire used to generate profile plots. Profile plots are generated from an average of 25 pixel lines perpendicular to the nanowire. (b) BSA in PBS while charged (red, +1 V) and discharged (black, -1 V). Data was captured and analyzed by S.B.T. and J.D.M. and plotted by J.D.M.

nanowire (d = 1.5 μm, l = 25 μm) in the presence of BSA (300 nM) in PBS. We again use profile plots to compare the spatial extent of control (Figure 2.6). We find that the thickness of our electrostatic double layer drops below the resolution of our microscope. This change is expected since the diffuse layer portion of the electrostatic double layer decreases as electrolyte concentration increases [163].

## 2.5 Conclusions

We have demonstrated that PEDOT:PSS nanowires can be used for the local control of protein concentration through an applied electric field. In water, these nanowires can control protein concentration over ∼30 μm for the wide, 1.5 μm diameter, nanowires and ∼17 μm for the thinner, 760 nm diameter, nanowires (Figures 2.2 and 2.5). The quantity of protein moved through solution can be controlled by the diameter of the nanowire, effectively altering the charge storage of the electrostatic double layer. The distance over which proteins can be modulated drops significantly in the presence of PBS, a high salt buffer, as the thickness of the electrostatic double layer decreases. These small, flexible, conductive, and biologically compatible PEDOT:PSS nanowires provide a new tool for the electrical

control of biological systems.

# CHAPTER 3

# CARDIOMYOCYTE CELL STIMULATION WITH PEDOT:PSS MICROWIRES



Scott B. Thourson and Christine K. Payne. ”Modulation of action potentials using PEDOT:PSS conducting polymer microwires”. In: Scientific Reports 7.1 (2017).

## 3.1 Overview

We describe the use of PEDOT:PSS conducting polymer microwires to modulate action potentials in single cells. PEDOT:PSS conducting polymer microwires are electrochemically synthesized with diameters ranging from 860 nm – 4.5 μm and conductivities of $\sim$30 S cm$^{-1}$. The length of the microwires is controlled by the spacing of the electrodes used for the electrochemical polymerization. We demonstrate the use of these microwires to control the action potentials of cardiomyocytes, showing that the cellular contractions match the frequency of the applied voltage. Membrane integrity assays confirm that the voltage delivered by the wires does not damage cells. We expect the conducting polymer microwires will be useful as minimally invasive devices to control the electrical properties of cells with high spatial precision.

## 3.2 Introduction

Integration of electronic devices with biological systems requires the development of new, less invasive tools, that can modulate cellular activity while minimizing disruption of the

surrounding tissue. Conventional electrodes made from metals, silicon, and carbon fibers are relatively hard and brittle making them inherently bio-incompatible [168, 186, 187]. The recent development of smaller, more flexible, materials, including single crystalline gold nanowires [188], nanoneedles, nanopillars, and nanotubes [64, 189–191], and conformable materials [192–195] has helped to address the need for less invasive tools. Similarly, conducting polymers have been used as coatings, films, or electrode materials to provide a softer interface with cells [192, 196–201]. Combining the benefits of a wire configuration with the softer material properties of conducting polymers, we have developed conducting polymer microwires as a small, flexible, electrically active material for the bioelectric interface that can be used to modulate the action potentials of individual cells.

Poly(3,4-ethylenedioxythiophene):polystyrene sulfonate (PEDOT:PSS) is a well-characterized conducting polymer [169], with known biocompatibility [173, 196, 202], that has been used previous to form conductive [158, 159, 165], flexible ($\sim$1 GPa) [203], nano- to micro-diameter wires. PEDOT:PSS conducting polymer microwires are electrochemically synthesized with diameters ranging from 860 nm – 4.5 μm and conductivities of $\sim$30 S cm$^{-1}$. The length of the microwires (nanometers-millimeters) is controlled by the spacing of the electrodes used for the electrochemical polymerization. We demonstrate the use of these microwires to control the action potentials of cardiomyocytes, showing that the cellular contractions match the frequency of the applied voltage. Membrane integrity assays confirm that the voltage delivered by the wires does not damage cells. Overall, the use of conducting polymer microwires to modulate the action potentials of cardiomyocytes is the first step in the development of a new tool for bioelectric electric control in vivo.

## 3.3 Materials and methods

### 3.3.1 Electrochemical polymerization and characterization of PEDOT:PSS microwires

The electrochemical synthesis and characterization of PEDOT:PSS nano- and microwires has been described previously [158, 159, 165]. In brief, PEDOT:PSS microwires were syn-

thesized from the tip of a sharp gold electrode in an aqueous solution containing 10 mM 3,4-ethylenedioxythiophene monomer (EDOT, Sigma-Aldrich, 483028, St. Louis, MO) and 20 mM polystyrene sulfonate (PSS, Sigma-Aldrich, 243051), used as a counterion. A second gold electrode is used to shape the electric field during the electrochemical synthesis. Fabrication of the sharp gold electrodes from solid gold wire (0.2 mm diameter, 99.9%, Alfa Aesar, 10195-G1) was based on methods used to etch scanning tunneling microscope electrodes [178], and has been described previously for the electrochemical synthesis of PEDOT:PSS conducting polymer wires [165]. Gold wire was submersed $\sim$1 mm in hydrochloric acid (6 M). Coiled platinum wire (0.3 mm diameter, 99.9%, Alfa Aesar, 43014-BU) served as the counter-electrode. A function generator (Agilent 33120A) provided a 10 Hz full square wave, $\pm$ 5 V amplitude. Etching for $\sim$90 s yielded tip diameters $<$ 100 nm. After etching, gold electrodes were rinsed with ethanol, then water, and dried under nitrogen. Gold electrodes were plasma cleaned (Harrick) for 15 seconds before use. During microwire synthesis, the gold electrodes were spaced 50 μm apart (tip-to-tip). Polymerization was carried out using a function generator (Agilent, 33120A, Santa Clara, CA) supplying an alternating, square-wave voltage (0.1 kHz – 5 kHz) across the two gold electrodes. Conducting polymer wire diameter was measured using a scanning electron microscope (SEM, Hitachi, SU8230, Tokyo, Japan). Conducting polymer wire length was measured using brightfield microscopy (Olympus IX71, 60x objective, Tokyo, Japan and Andor iXon CCD camera, Belfast, UK). Conductivity was measured with two-point probe using a sourcemeter (Keithley, 2400, Solon, OH) to sweep the voltage between -1 and +1 V while measuring current. Resistance was calculated from the inverse slope of the current-voltage curves. Conductivity was determined using diameter and length measurements obtained from microscopy images.

### 3.3.2 Cell culture

Neonatal rat cardiomyocytes were a gift from Prof. Hee Cheol Cho at Georgia Tech and Emory University. Glass bottom cell culture dishes (3.5 cm, MatTek, P35G-0.170-14-C, Ashland, MA) were coated with 40 μg $mL^{-1}$ – 250 μg $mL^{-1}$ fibronectin (356008, Corning, NY) in phosphate-buffered saline (PBS, 14190144, Invitrogen, Carlsbad, CA) for at least 1 hour prior to seeding cells. Culture medium consisted of M199 medium (M4530-1L, Sigma-Aldrich) supplemented with 10 mM HEPES, 0.1 mM MEM non-essential amino acids, 3.5 mg $mL^{-1}$ glucose, 2 mM L-glutamine, 4 μg $mL^{-1}$ vitamin B12, and 100 U $mL^{-1}$ streptavidin/penicillin. This medium was supplemented with 10 % FBS for the first two days of culture and 2 % for the third day. Cells were used within 3 days of culture (37 °C and 5 % carbon dioxide). Prior to experiments, cells were rinsed with Tyrode's solution (137 mM NaCl, 4 mM KCl, 1.8 mM CaCl2, 1 mM MgCl2, 10 mM HEPES, 10 mM glucose) at 37 °C.

Human cervical carcinoma cells (HeLa, CCL-2, ATCC, Manassas, VA) were cultured in Minimum Essential Medium (MEM, 61100, Invitrogen) supplemented with 10 % fetal bovine serum (FBS, 10437028, Invitrogen) at 37 °C and 5 % carbon dioxide. On the day before experiments, MEM with phenol red was replaced with phenol red-free MEM (51200-038, Gibco/Thermo Fisher, Waltham, MA) to reduce background fluorescence. Cells were passaged every 3 – 4 days. Propidium iodide (PI, P1304MP, Invitrogen) was added to the cells for a final concentration of 500 μM 10 minutes prior to experiments.

### 3.3.3 Cardiomyocyte stimulation and analysis

Following electrochemical polymerization, PEDOT:PSS microwires were removed from the monomer solution and placed in a cell culture dish containing the cardiomyocytes. Micromanipulators were used to position the microwires. Modulation was carried out in Tyrode's solution at room temperature. Cathodic-led biphasic voltage pulses were delivered at 1 Hz with a pulse width of 1 ms and an interphase period of 1 ms (Keithley 2400

sourcemeter). Throughout this process, the cells were imaged at 10 fps using brightfield microscopy (Olympus IX71, 60x objective, Andor iXon CCD camera). Contraction of cardiomyocytes was analyzed using Tracker version 4.96 (Douglas Brown, Open Source Physics, http://physlets.org/tracker/index.html) video tracking software.

COMSOL Multiphysics modeling software (COMSOL, Palo Alto, CA) was used to calculate the electric flux at the plasma membrane. The conducting polymer microwires expose cells to a nonuniform electric field. The shape of this field depends on the geometry, conductivity, potential, and position of the PEDOT:PSS wires. These parameters were used in COMSOL simulations to model the instantaneous, nonuniform, electric field generated by each experimentally applied pair of voltage and conducting polymer wire separations. The electric field distribution was integrated over the area of the cell membrane to obtain electric flux. The membrane area was approximated by a rectangle with a height of 5 μm and a width equal to the width of the cell. The rectangular cross section was positioned and angled with respect to the position and axis of the conducting polymer wire to match experimental conditions. The microwire geometry was approximated as a cylinder with a hemisphere located at the microwire tip. The gold electrode was modeled as a cone with the tip placed 5 μm within the base of conducting polymer wire. The length of the conducting polymer wire was defined as the distance from the tip of the gold electrode to the tip of the conducting polymer wire. Electrical conductivity of gold, PEDOT:PSS, and the PBS solution was 456,000 S $cm^{-1}$ (COMSOL-provided value), 37 S $cm^{-1}$ (approximate average for microwires $\geq$ 1 μm diameter), and 1.5 S $m^{-1}$ (approximated using a supplier-provided value for PBS), respectively. Voltage boundary conditions were applied at the base of the gold electrode cones. Electric flux values (Figure 3.1) were obtained for cross-sectional rectangles positioned between 0.25 μm and 48 μm from the tip of the conducting polymer wire near the cell. Rectangular cross-sections were spaced by 1 μm and 2 μm for positions between 0 – 8 μm and 8 – 48 μm, respectively.

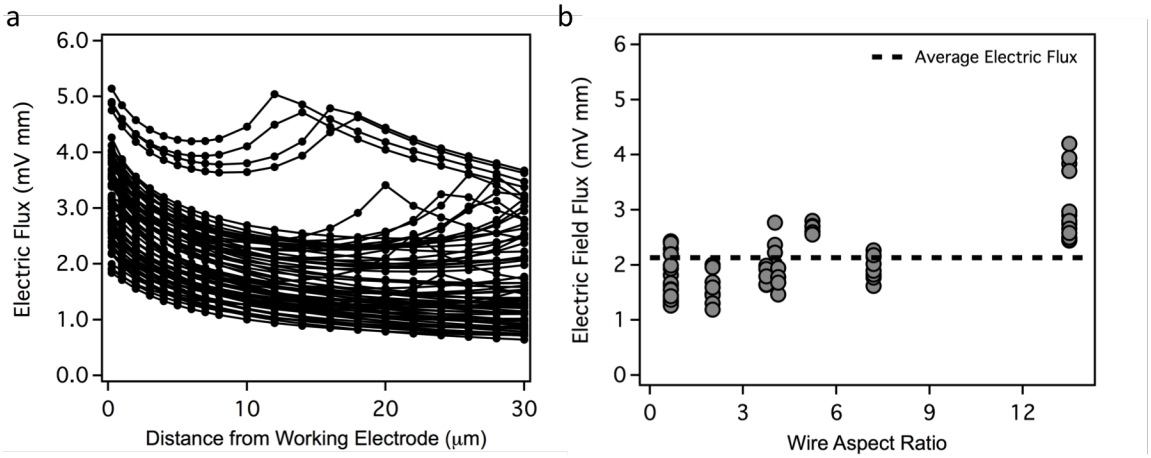


**Figure 3.1:** The minimum electric flux required for cellular modulation was found by varying the distance between the microwires and determining the point at which cardiomyocyte contractions became irregular ($<$ 9 consecutive contractions). 8 different microwires and 19 different cardiomyocyte cells were tested in 71 experiments. The cathode position was held constant. (a) The calculated electric flux (COMSOL) is plotted for each data point in Figure 3b as a function of distance from the working electrode where 0 is at the tip of the cathode. (b) The threshold electric field flux for each curve at 6 μm from the tip of the working electrode is nearly constant (2.13 $\pm$ 0.65 mV mm).

### 3.3.4 Charge storage density from current transients

Electrical current curves of PEDOT:PSS microwires and gold electrodes were measured for 1 V voltage steps. Surface area was controlled using a micromanipulator to position the microwire or gold electrode in a droplet of PBS in electrical contact with a large carbon counter electrode (Figure 3.2a). Controlling the microwire immersion depth removed the charge contribution from the uninsulated gold electrode allowing us and to measure charge storage as a function of microwire geometry. To prevent the microwires from breaking at the air-water interface, coverslips with a hydrophobic layer of trichloro(1H,1H,2H,2H-perfluorooctyl)silane (448931, Sigma-Aldrich) were used to increase the PBS contact angle, allowing the microwire to be inserted and removed from the droplet perpendicular to the air-water interface. A 1 V voltage step was applied to the microwires for 20 – 30 ms at a frequency of 1 Hz. The current was measured using a current-to-voltage converter constructed using a high-impedance operational amplifier with a gain of 105. The proportional voltage was recorded using an oscilloscope (TBS1064, Tektronix, Beaverton, OR) at a sample rate of 250 kHz. Microscope images were used to measure the microwire immersion depth for each corresponding current transient (Figure 3.2b). Custom Igor Pro code

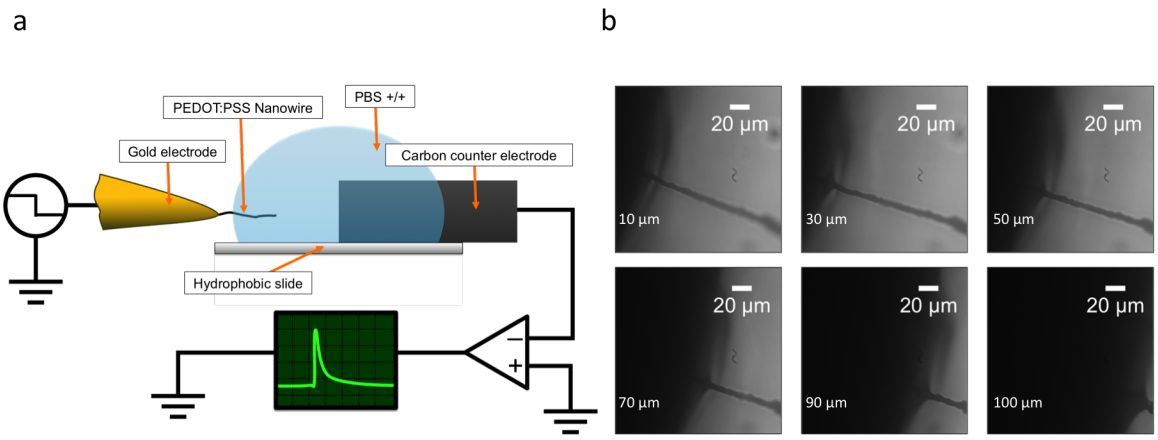


**Figure 3.2:** Measurement of current transients (Figure 3.6). (a) Schematic of the immersion method used to obtain current transients of PEDOT:PSS microwires. Following microwire synthesis, a micromanipulator on an inverted microscope was used to control the electrochemical area of the microwire in a 200 L drop of phosphate buffered saline (PBS) on a hydrophobic slide. A source meter applied a -1 V cathodic step between the microwire and a large carbon-counter electrode. Current was amplified with a transimpedance amplifier and read using an oscilloscope. (b) Brightfield images showing a 2 kHz microwire immersed at different depths in a PBS droplet.

was used to calculate charge storage by integrating the area under each current transient.

### 3.3.5 Electric flux for neonatal cardiomyocyte stimulation

COMSOL Multiphysics modeling software (COMSOL, Palo Alto, CA) was used to calculate the electric flux at the plasma membrane. The conducting polymer microwires expose cells to a nonuniform electric field. The shape of this field depends on the geometry, conductivity, potential, and position of the PEDOT:PSS wires. These parameters were used in COMSOL simulations to model the instantaneous, nonuniform, electric field generated by each experimentally applied pair of voltage and conducting polymer wire separations. The electric field distribution was integrated over the area of the cell membrane to obtain electric flux. The membrane area was approximated by a rectangle with a height of 5 µm and a width equal to the width of the cell. The rectangular cross section was positioned and angled with respect to the position and axis of the conducting polymer wire to match experimental conditions. The microwire geometry was approximated as a cylinder with a hemisphere located at the microwire tip. The gold electrode was modeled as a cone with the tip placed 5 µm within the base of conducting polymer wire. The length of the conducting polymer wire was defined as the distance from the tip of the gold electrode to the tip

of the conducting polymer wire. Electrical conductivity of gold, PEDOT:PSS, and the PBS solution was 456,000 S $cm^{-1}$ (COMSOL-provided value), 37 S $cm^{-1}$ (approximate average for microwires $\sim$1 μm diameter), and 1.5 S $cm^{-1}$ (approximated using a supplier-provided value for PBS), respectively. Voltage boundary conditions were applied at the base of the gold electrode cones. Electric flux values (Figure 3.1) were obtained for cross-sectional rectangles positioned between 0.25 μm and 48 μm from the tip of the conducting polymer wire near the cell. Rectangular cross-sections were spaced by 1 μm and 2 μm for positions between 0-8 μm and 8-48 μm, respectively.

## 3.4 Results and discussion

### 3.4.1 PEDOT:PSS microwire diameter dependence on frequency

The electrochemical synthesis of PEDOT:PSS conducting polymer nano- and microwires has been described previously [158, 159, 165, 204]. In brief, the wires are grown in an aqueous solution containing EDOT (10 mM) monomer and PSS (20 mM) from the tip of a sharp gold electrode, using a second gold electrode to shape the electric field. The length of the wire is controlled by the spacing of the two gold electrodes during the electrochemical polymerization. Microwire diameter is controlled by the frequency (0.1 – 5 kHz) of the AC voltage ($\pm$ 1 – 3 V, square wave) used for the polymerization (Figure 3.3a), similar to the approach used for gold and iridium nanowires [156]. Microwire diameters were measured with SEM. Although it is possible to synthesize wires with diameters of 150 nm (100 kHz), micron-diameter wires were used in the experiments described below. Conductivity of the microwires were measured by two-point probe (Figure 3.3b) with values ranging from 11 S $cm^{-1}$ to 80 S $cm^{-1}$. Average conductivity for PEDOT:PSS wires synthesized in our lab is 33 $\pm$ 21 S $cm^{-1}$ (n = 18 wires). Previous work has reported conductivities of $\sim$8.0 S $cm^{-1}$ for PEDOT:PSS wires (340 nm diameter) synthesized using an identical approach [158]. The variation in conductivity is likely due to variation in the distribution of the electrically conductive PEDOT and insulating PSS that occurs during the electropolymerization

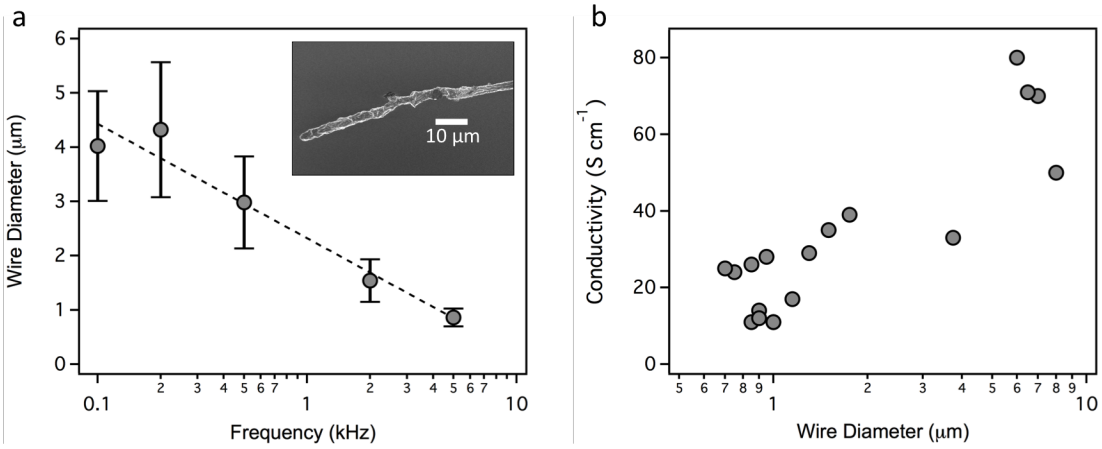


**Figure 3.3:** Characterization of PEDOT:PSS microwires. (a) Microwire diameter as a function of the AC frequency used for electrochemical polymerization. Data was obtained from SEM images for n $\geq$ 3 different microwires. The dashed line shows the best fit to the data. Error bars represent $\pm$ standard deviation of the mean. The inset shows a representative SEM image of a PEDOT:PSS microwire grown using a 500 Hz square wave. (b) Conductivity of PEDOT:PSS microwires as a function of wire diameter. (n = 8, two values overlap)

process.

### 3.4.2 Cardiomyocyte stimulation

The physiological activity of neurons, muscle cells, and heart cells depends on action potentials, rapid changes in ion gradients. For cardiomyocytes, action potentials are associated with cellular contractions, the familiar 'beating.' We tested the microwires to determine if they could modulate the action potentials of neonatal rat cardiomyocytes. Induction of an action potential was measured by tracking the displacement of a region of the plasma membrane of individual cells. Two microwires (3.0 μm diameter, 11 μm length), serving as an electrode and counter-electrode, were placed in solution next to a cell of interest (Figure 2a). In the absence of an applied voltage, there is occasional spontaneous beating, with the cell contracting infrequently (Figure 3.4b, top). Applying a $\pm$ 1 V biphasic pulse, the cell beats in response to the frequency (1 Hz) of the applied voltage (Figure 2b, bottom).

Subsequent experiments determined the microwire and electrical parameters necessary to induce an action potential in the cardiomyocytes (Figure 3.5). Successful modulation was defined as regular ($\sim$3) contractions in response to the applied voltage, in comparison to skipped, irregular ($<$ 3), contractions (Figure 3.5a). As expected, modulation is sensitive to microwire diameter, length, spacing, and applied voltage (Figure 3.5b). Wire diameter

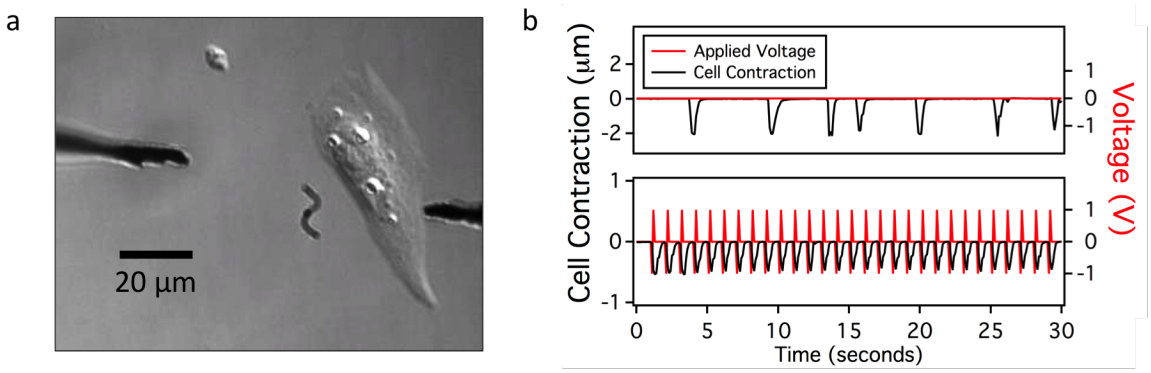


**Figure 3.4:** Electrical modulation of a cardiomyocyte. (a) Brightfield microscopy image of a neonatal cardiomyocyte showing the two microwires positioned for modulation (3.0 µm diameter, 11 µm long). In this image, the working electrode is on the right. (b) Cell contractions are recorded by tracking the displacement of a region of the cell in response to an applied voltage (red, 1 V biphasic pulse, 1 ms, 1 Hz). This example is representative of experiments with 40 distinct cardiomyocytes.

and length can be considered together as an aspect ratio (length diameter$^{-1}$). Spacing is defined as the distance between the two conducting polymer wires serving as electrode and counter-electrode. The distance between the working electrode and the plasma membrane of the cell was held nearly constant (2.31 µm ± 1.32 µm) for all experiments as the modulation of action potentials is very sensitive to this distance. These experiments show that long or narrow microwires require a greater voltage or shorter inter-wire distance to induce an action potential. Ultimately, these three parameters (aspect ratio, spacing, and applied voltage) converge on a minimum electric flux required to induce regular action potentials (Figure 3.1). Previous studies with cardiomyocytes (chick, guinea pig, and canine, 10 ms stimulus) and conventional bulk electrodes have found that a minimum uniform electric field of 0.14 V mm$^{-1}$ – 2.25 V mm$^{-1}$ is required for the stimulation of single cells, depending on the cell source and direction of the applied field (parallel or perpendicular) [205–207]. In comparison, an average electric field of 6.2 ± 1.9 V mm$^{-1}$ was required in our experiments (n = 71 experiments using 19 cells and 8 wires, Figure S1), in good agreement considering the use of a non-uniform electrical field and differences in cell types and experimental approach.

We carried out control experiments, testing 13 cells with 7 different pairs of gold electrodes, to ensure that the sharp gold electrodes used to synthesize the microwires were not responsible for the modulation of action potentials. The gold sharp electrodes were not

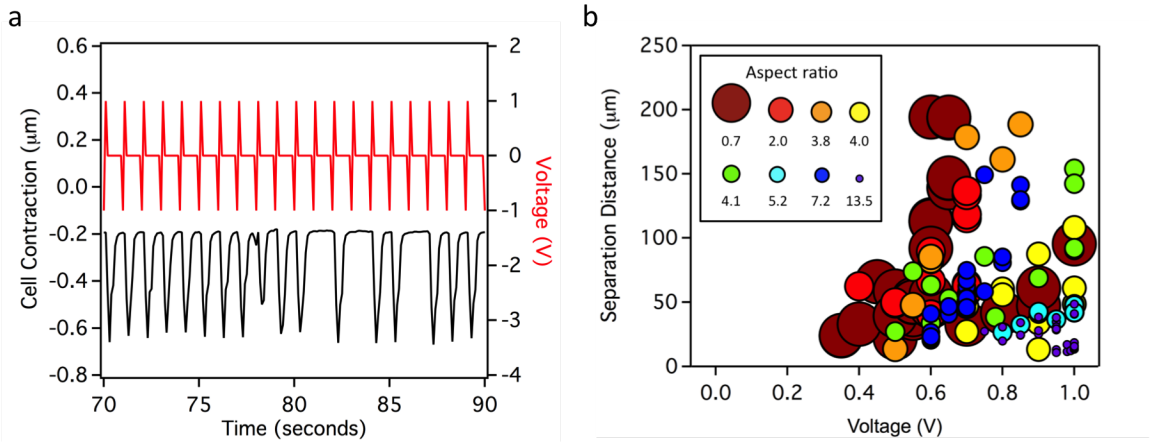


**Figure 3.5:** A combination of wire diameter, length, applied voltage, and wire spacing determine whether the electric flux at the cell is sufficient for cellular modulation. (a) Successful modulation was determined by observing cell contractions (black) in response to an applied voltage (red), measured using video tracking of a portion of the cell. Insufficient flux resulted in irregular contractions. This example, in which the distance between the wires was increased at 80 s, shows a maximum of 3 consecutive contractions at the increased spacing. (b) Modulation data from 8 different wires tested on 19 different cells as a function of aspect ratio (length/diameter) of the working electrode, separation between the wires, and voltage. Circle size represents wire aspect ratio.

capable of cellular modulation, independent of voltage or spacing between electrodes. To understand this difference, we measured the charge storage density of the conducting polymer microwires and gold electrodes by analyzing current transients in response to a 1 V pulse (Figure 3.6). The surface area of each microwire was controlled by immersion into an electrolyte solution of phosphate buffered saline (PBS, Figure 3.2). Current transients were integrated with respect to time to obtain the total charge transferred by the microwire and normalized by the surface area of the microwire. While the electric field at the sharp tip of the gold electrodes is extremely high ($\sim$1 kV mm$^{-1}$ based on COMSOL simulations), when the electric field is multiplied by its small surface area at the cell membrane a very small electric field flux is present, consistent with the inability of these bare gold electrodes to induce action potentials cardiomyocytes.

The measurement of current transients also points towards the minimum electric flux required for cellular modulation. Thinner PEDOT:PSS wires (1.5 µm diameter, 8.5 µm length; 1 V, 1 Hz) did not induce action potentials in the cardiomyocytes. Using a conductivity of 1.5 S m$^{-1}$ to describe the surrounding cell culture media and an electric flux of 2.13 0.65 mV mm (n = 71 experiments using 19 cells and 8 wires, Figure S1), we estimate an

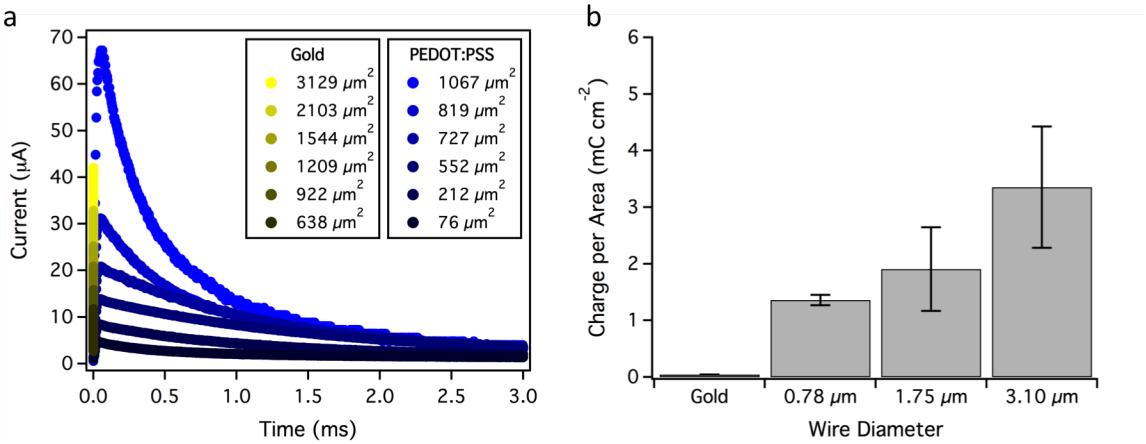


**Figure 3.6:** Induction of action potentials requires conducting polymer microwires. (a) Representative electrical current transients recorded from a PEDOT:PSS microwire (blue, 3.1 μm diameter) and a gold electrode. Electrical current from a 1 V step was amplified using a transimpedance amplifier and recorded with an oscilloscope. Surface area was varied by controlling the length of microwire or electrode immersed in a buffer solution (Figure 3.2). (b) Charge storage density of a gold electrode and conducting polymer microwires. Charge per area was obtained by integrating the current transients in (a) and normalizing them to geometric surface area by approximating the microwire as a cylinder.

instantaneous membrane current of 3.2 μA is required for stimulation, assuming a cellular cross-sectional area of 345 $\mu m^2$.

### 3.4.3 HeLa cell health due to microwire stimulation

Cell health following the use of microwires was tested using propidium iodide (PI), a fluorogenic dye that binds to nucleic acids. Healthy cells with intact membranes are impermeable to PI, appearing dark in a fluorescence microscopy image. If the cell membrane is damaged, PI enters the cells, leading to a fluorescent cell. Human cervical cancer cells (HeLa) were incubated with PI (500 μM, 10 min pre-incubation) and a voltage was applied to the cells (4.9 μm diameter (average), 4.5 – 21 μm long wires, ± 1 V, 1 Hz, biphasic), similar to conditions used for cardiomyocytes (Figure 3.4). We recorded brightfield and fluorescence images before and after 1000 pulses from the microwires. In comparison, experiments with the cardiomyocyte typically measured action potentials for 100 pulses, with each pulse inducing an action potential. No sign of PI internalization was observed, indicating that the microwires and applied voltage do not damage the plasma membrane. We did test the limits of plasma membrane integrity using extremely high voltages (± 5 V and ± 10 V, Figure 3.8). At ± 10 V (4.9 μm diameter (average), 4.5 – 21 μm long wires, 1

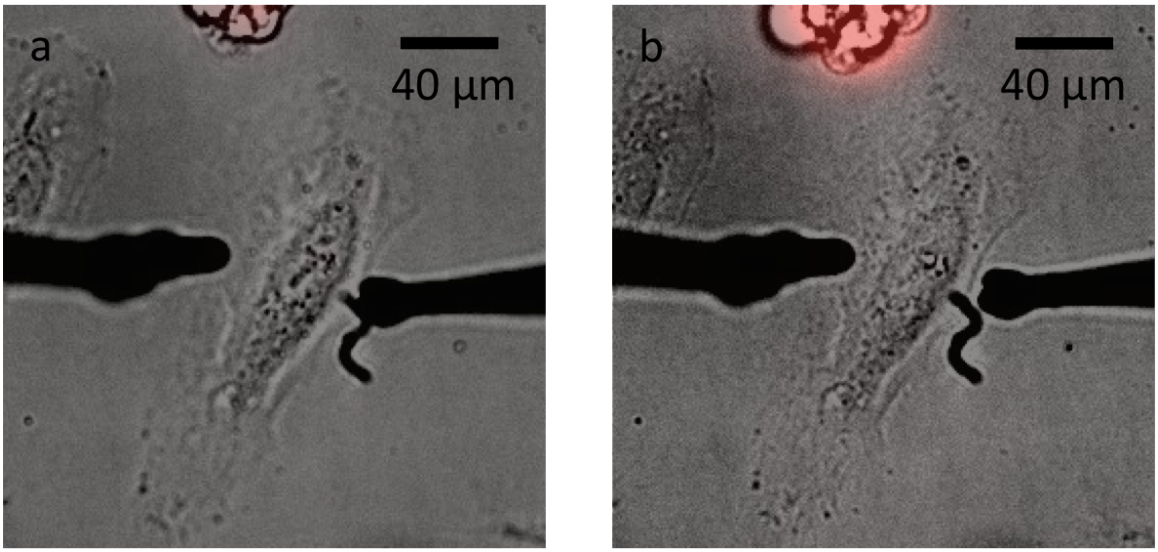


**Figure 3.7:** The plasma membrane is not disrupted by microwire activity. (a) Overlaid brightfield and fluorescence microscopy images of microwires and a HeLa cell, incubated with PI (500 µM, red), prior to an applied voltage. The cell debris at the top of the image appear red because the plasma membrane is disrupted making them permeable to PI. (b) The same cell was imaged after the microwires (left wire = 5 µm diameter, 21 µm long; right wire = 7.5 µm diameter, 4.5 µm long) were used to deliver 1000 consecutive pulses (1 V, 1 Hz, biphasic). Identical experiments were carried out for three different wires, testing 3 cells with each wire (n = 9 cells in total).

Hz, biphasic, 60 pulses) some cell death was detected. No cell death was detected at ± 5 V following 60 pulses. At longer times and/or higher voltages, electrolysis of water damaged the cells.

## 3.5 Conclusions

These conducting polymer wires, with small, easily tuned diameters (860 nm – 4.5 µm) and moderate conductivities (33 ± 21 S $cm^{-1}$) (Figure 3.3) provide a new, much less invasive, tool for the control of action potentials (Figure 3.4). In comparison to surface microelectrodes, microwires, positioned by micromanipulators, provide a straight-forward configuration to address single cells. Physically, the conducting polymer wires control the ion concentration at the plasma membrane. They do not penetrate or even contact the plasma membrane. In comparison to patch-clamping, the ability to induce an action potential by only placing the microwires near a cell is expected to have a much greater throughput for experiments. The activity of the wires depends on wire diameter, length, spacing, and applied voltage (Figure 3.5), which can be considered as a minimum electric flux required

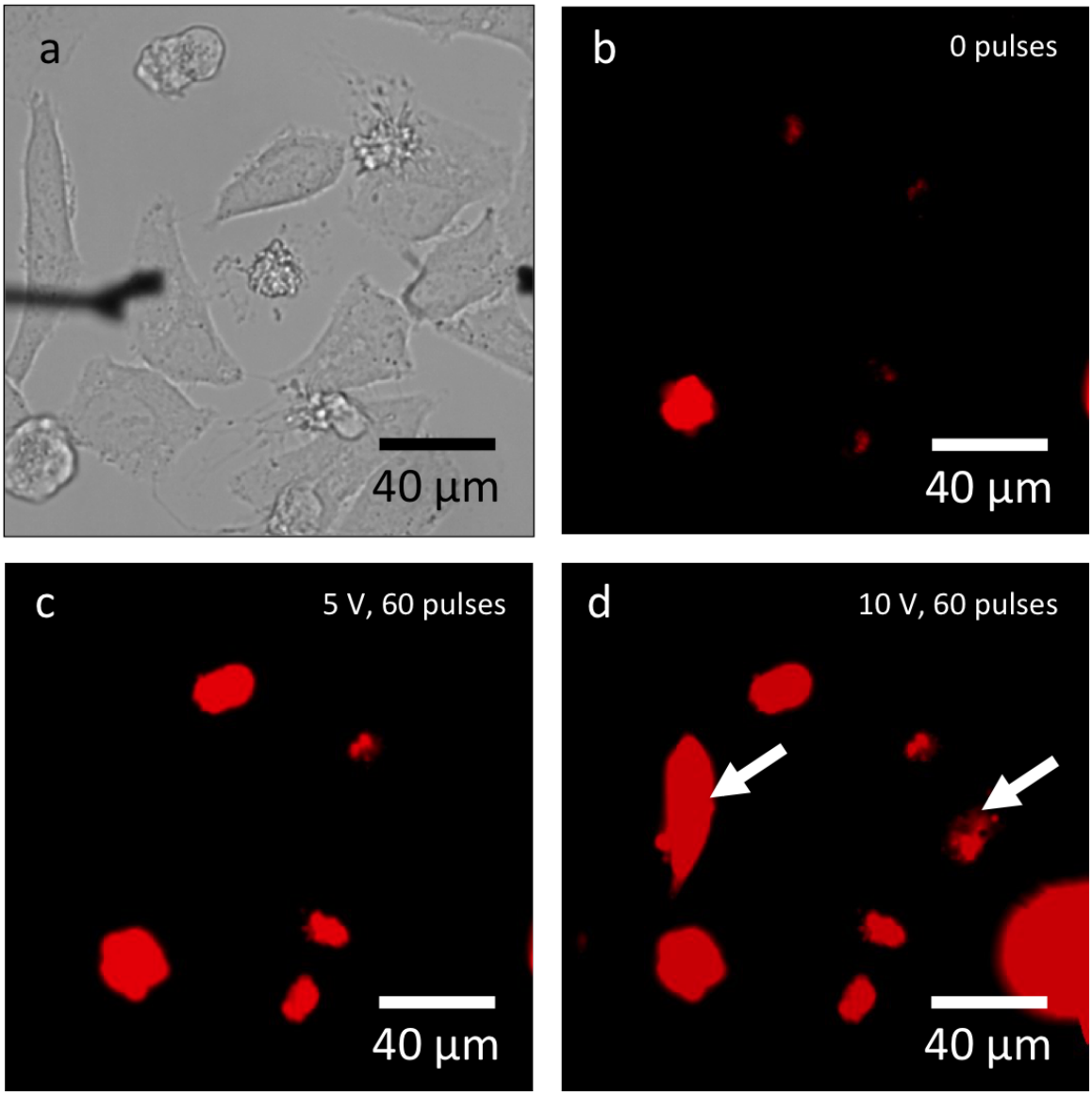


**Figure 3.8:** Cytotoxicity test of PEDOT:PSS microwire modulation using HeLa cells incubated with propidium iodide (PI). PI is a cell impermeant fluorogenic dye that only enters cells or cell debris with a permeabilized membrane, indicating that the cells are damaged. (a) Brightfield microscopy image of PEDOT:PSS microwires placed near the membrane of a HeLa cell and (b) corresponding fluorescence microscopy image with PI (500 µM, red) present in the cell culture medium. The fluorescent signal present in these images shows that the plasma membrane of the cell debris is permeabilized prior to microwire activity. (c) Following 60 pulses at 5 V (1 Hz, biphasic) the cell debris internalize additional PI. The adherent cells remain healthy. (d) After an additional 60 pulses, now at 10 V (1 Hz, biphasic), two dead cells are observed as the new fluorescent signal (indicated by arrows).

for modulation. The electric flux delivered by the microwires does not damage the plasma membrane at the levels required for modulation (Figure 3.7). Similar experiments using conducting polymer wires to control the resting membrane potential of E. coli also showed that these microwires do not damage cells [204].

The advantage of the conducting polymer microwires compared to conventional bulk electrodes, which have been used previously to stimulate chick, guinea pig, and canine cardiomyocytes [205–207], or even patterned substrates, is the small, sub-cellular, diameter of the microwires. Our previous work using similar conducting polymer microwires to control local protein concentration and the resting membrane potential of E. coli suggests a $< 50$ μm distance of activity [165, 204], which will make these microwires useful for cellular-level studies, such as neural mapping, where the localized modulation of an action potential is required. Future work will be necessary to measure the distance of activity both in cell-free systems and for the modulation of action potentials in monolayers of cells. Most similar to the conducting polymer microwires are single crystalline gold nanowires ($\sim$100 nm), which have been used for neural recording, including the detection of the site of epileptic spikes [188], and the triggered release of dopamine [208], These gold nanowires have a similar advantage of sub-cellular control and low Young's modulus, although device construction is quite difficult. Individual tungsten tips are attached to individual gold nanowires with a conductive carbon paste [188]. In comparison, the conducting polymer wires are synthesized directly from a gold electrode forming the device in a single step. Overall, we expect the conducting polymer wires will provide a new tool for the modulation and mapping of action potentials. The small diameter will allow cellular-level control and the relatively low Young's modulus ($\sim$1GPa) [156] suggests they will be a less invasive tool for future in vivo studies.

# CHAPTER 4
# MEMBRANE POTENTIAL CHANGES IN POLYMER INDUCED ELECTRIC FIELDS

## 4.1 Overview

PEDOT:PSS conductive polymer wires have previously been tested as single cell stimulation electrodes using cardiomyocytes. Various polymer wire dimensions were used to stimulate individual cardiomyocytes at various voltages and wire locations. Cardiomyocyte contraction was used as a digital indicator of successful electrical stimulation by polymer wires. Using 1 V as the upper voltage limit, the minimum dimensions for a wire used to stimulate a single cell was found to be around 2 x 27 μm. However, cardiomyocytes can typically contract spontaneously, without stimulation, and their response to stimulation varies based on their health and shape.

Here, patch clamping was used to directly measure membrane potential of HEK cells in response to a nonuniform electric field generated by PEDOT:PSS polymer stubs (small cylindrical deposits) and wires. The field generated by stubs and wires smaller than 2 x 27 μm is investigated and compared to larger polymer dimensions. A COMSOL model is built to reproduce the potential fields generated by polymer stubs and wires. The first part of this research focuses on characterizing the electrochemical surface properties of PEDOT:PSS and bare gold to provide accurate material properties for the model. Surface impedance values from conventional techniques, such as electrical impedance spectroscopy (EIS), are compared to uniform potential fields measured *in situ* using a glass pipette microelectrode. Polymer stubs and wires are then placed near HEK cells during 1 V, 1 kHz sinusoidal stimulation. Changes in membrane potential were measured directly using patch clamping. The results were then compared to the model in the context of potential field shape

and magnitude. Uniform fields generated by bare gold and measured with a glass pipette closely matched the surface impedance values obtained from EIS measurements. Uniform fields generated by PEDOT:PSS, however, were underestimated by EIS by almost an order of magnitude. Nonuniform potential measurements were conducted for cylindrical PEDOT:PSS stubs at the end of sharp gold electrodes. The model consistently underestimated the field generated by stubs with diameters greater than 2 μm and overestimated for diameters less than 2 μm.

The discrepancy for smaller diameters wa s likely due to the limitations of using a time averaged surface impedance in a static model. Time-dependent studies suggest that the capacitance of the small stub diameters may be too small to measure with local field potentials under a 1 kHz excitation. Underestimation of larger diameter stubs may be due to using a spatially-averaged surface impedance that does not account for the three-dimensional charge interaction in a porous polymer matrix. Patch clamping results of HEK cells in nonuniform potential fields indicate that cell membrane potential roughly matched the model-predicted potential field generated by PEDOT:PSS structures at the cell membrane. The model tested surface impedance values obtained from both uniform potential mapping, nonuniform potential mapping, and EIS. Interestingly, uniform field derived surface impedance values were found to be more accurate for polymer stub diameters greater than 2 μm. The field generated at cells using smaller diameter stubs and wires were overestimated in all cases. These results have implications regarding the dimensional limits in which a Neumann boundary condition can be used to accurately model potential fields generated by porous, low surface impedance materials.

## 4.2 Materials and methods

### 4.2.1 Polymer film synthesis

Gold wire was vertically immersed 4 mm (for EIS) or 8 mm (for field mapping) into a 10 mL solution of 10 mM EDOT and 20 mM PSS in a rectangular polystyrene chamber on

a glass coverslip (Lab-Tek®Glass Chamber Slide). A coiled platinum wire served as the counter electrode with a custom made Ag/AgCl reference microelectrode placed as close to the gold working electrode as possible. Short constant current pulses of 13 nA $mm^{-2}$ were applied using a Keithley 2400 sourcemeter controlled by an in house Igor Pro script. The applied voltage was monitored *in situ* during polymerization as a preliminary indication of relative changes in surface impedance. The voltage from 5 pulses each of 1, 10, and 100 ms in duration were applied repeatedly until the desired charge deposition density of PEDOT:PSS was achieved. Charge deposition densities of 2, 10, 20, and 50 mC $cm^{-2}$ were used. Scanning electron microscopy was used to image film morphology at each charge deposition density.

### 4.2.2 Polymer stub synthesis

Isolated cylindrical polymer stubs at the tips of gold electrodes were fabricated for electric field mapping and cell stimulation studies. Custom, sharp gold electrodes were fabricated as previously described [150, 165]. Briefly, 0.2 mm gold wire was etched in 6 M HCl using a 10 Hz, +7 V rectified square wave. Each gold electrode was rinsed in 70% ethanol and plasma cleaned on high for 20 seconds before use. Two, three-axis manual micromanipulators were used to position the tip of one gold electrode into the field of view of an Olympus inverted microscope at 64x magnification. A 300 μL drop of an aqueous solution containing 10 mM EDOT and 20 mM PSS was added to a glass cover slip. Glass coverslips were treated with a hydrophobic layer to increase the contact angle of the droplets and allow the gold electrode tip to be inserted perpendicularly to the air/liquid interface [150]. The tip of the gold electrode was inserted only 5 – 10 μm into the monomer solution to ensure that the rest of the gold electrode remained uncoated. A coiled platinum wire was used as the counter electrode. Polymerization at the gold tip was performed with 2 second pulses at a constant voltage of +900 mV vs. Ag/AgCl reference microelectrode using a Keithley 2400 sourcemeter controlled by an in house Igor Pro script. Electropolymerization was observed

to occur more rapidly at the air water interface onto the gold, which created undesirable polymer geometries. Therefore, each gold electrode was slowly retracted from the solution during polymerization using the micromanipulator. Electrode retraction during each pulse promoted uniform polymerization and formed a cylindrical polymer geometry at the electrode tip. Larger diameter polymer stubs were obtained by repeating this process for up to six additional pulses. The monomer solution was replenished after every three stubs.

### 4.2.3 Self-assembled monolayer deposition for gold insulation

Gold was electrochemical insulated using a 1-dodecanethiol self-assembled monolayer (SAM) coating [209]. Gold wire and electrodes were first electrochemically etched for a few seconds in 6 M HCl using a 10 V, 10 Hz rectified square wave. Gold electrodes were rinsed in 70% ethanol and then plasma cleaned on high for 20 s. Electrodes were then immersed in a 10 mM solution of 1-Dodecanethiol in 100% ethanol for at least 18 hours. Electrodes were then finally rinsed in 70% ethanol.

### 4.2.4 Polymer wire synthesis on insulated gold

Sharp gold electrodes were etched and electrically insulated with a SAM prior to wire growth. Two electrodes were positioned with manipulators under a microscope in air. The tips of the electrodes were brought into contact to create an electrical short while a 3 V, 10 kHz full square wave was applied using an Agilent 33120A function generator. The high current concentration melted the tips and locally destroyed the ordered SAM coating. The electrodes with exposed tips were then fully inserted into 100 μL of the EDOT and PSS monomer solution. The tips were placed as close as possible, typically within 10 μm, to minimize the required voltage needed for wire growth. A 1 – 3 kHz square wave was applied between the electrodes to initiate wire polymerization depending on the desired diameter as previously described [165]. The voltage amplitude was increased until polymer wire formation was observed. Images before and after wire synthesis revealed small

deposits of polymer formation at various defect sites in the SAM coating. These polymer deposits were visibly removed prior to cell experiments using a mixture of $NH_4OH$-$H_2O_2$-$H_2O$ [210] in the presence of a rectified square wave with an amplitude of 3 V and at a frequency of 10 kHz. The polymer wire was protected from the cleaning solution by keeping it in air during the cleaning process. Electric potential mapping revealed that electrodes cleaned in this way exhibited a surface impedance similar to that of SAM-coated gold.

### 4.2.5 Conductivity

Conductivity was found from two-point probe resistance measurements across several PEDOT:PSS wires. Polymer wires were removed from the monomer solution following growth and inserted into a 100 μL drop of deionized water. Water was used to eliminate current contributions from ionic double layer charging while still maintaining an aqueous environment. PEDOT:PSS has previously been shown to have a similar conductivity in water and electrolyte solutions [133]. A clean, sharp gold counter electrode was brought into contact with the wire in water. Contact resistance can vary significantly between polymer and metal since the surface of the polymer is a rough matrix with a nonuniform distribution of conducting regions. A 10 kHz square wave with an amplitude of 1 – 3 V was applied up to 60 s to temporarily establish ohmic contact between the counter gold electrode and the wire. Immediately after fusion, resistance measurements were obtained by sweeping an applied voltage between -1 and +1 V. Several trials were performed while increasing fusion voltage by 100 mV until the measured resistance decreased to a minimum value. The resistance was determined from the slope of current vs. voltage curves using a linear regression (Figure 4.1). The trial that yielded the lowest resistance was used for each measurement to maximize consistency. Contact resistance was still found to be significant and was accounted for by repeating resistance measurements at several points along the wire (Figure 4.2a). The resistance was plotted as a function of position along the wire (Figure 4.2b). The slope was used to determine resistivity of the wire, which is independent of

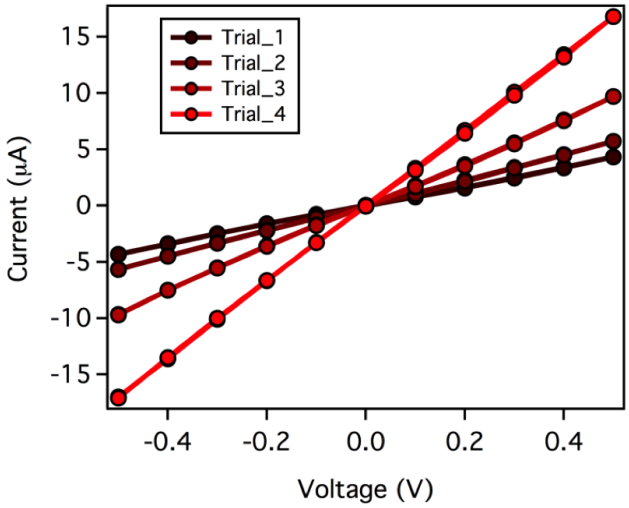


**Figure 4.1:** Representative current-voltage (IV) curves along a PEDOT:PSS wire with a diameter of 570 nm. IV curves were obtained for n = 9 wires.

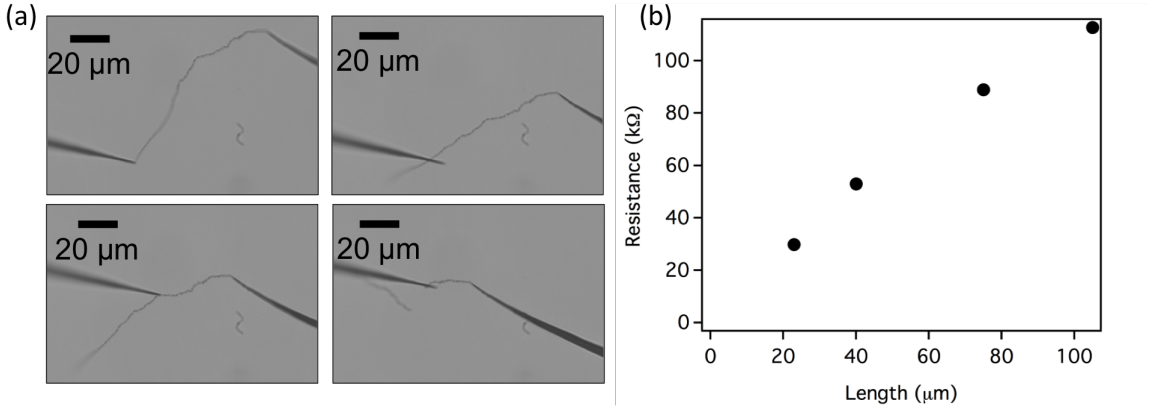


**Figure 4.2:** (a) Microscope images showing a sharp bare gold electrode (left) applying a voltage at several points along the same PEDOT:PSS wire. (b) Representative resistance values obtained at each location along the wire shown in (a).

contact resistance.

### 4.2.6 Electrical impedance spectroscopy

Bare gold and PEDOT:PSS coated gold electrodes at charge densities of 2, 10, 20, and 50 mC $cm^{-2}$ were vertically immersed into a beaker filled with HEK extracellular medium. A custom Ag/AgCl reference microelectrode was placed as close to the working electrode as possible with a coiled platinum wire as the counter electrode. A C60 Electrochemical Workstation and software was used to perform electrical impedance spectroscopy (EIS) on the working electrode. A voltage magnitude of 400 mV was used to test the impedance of the working electrode between the frequencies of 1 Hz and 100 kHz. The working

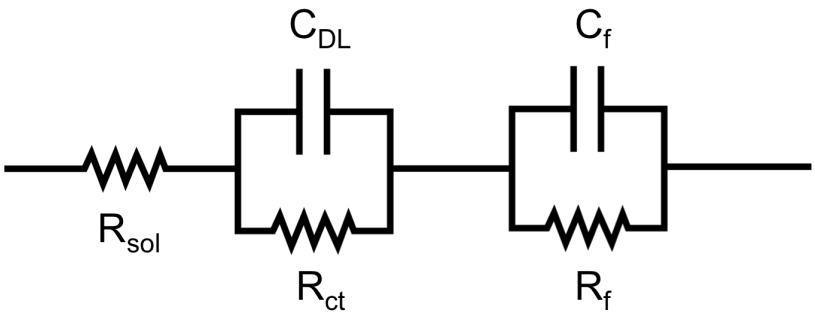


**Figure 4.3:** Equivalent circuit model used for EIS fitting where $C_f$ is the film capacitance, $R_f$ is the film resistance, $C_{DL}$, is the electric double layer capacitance, $R_{ct}$ is the faradaic charge transfer resistance and $R_{sol}$ is the solution resistance.

electrode was tested at different depths of 1, 2, and 3 mm. A corkscrew lift was used to control the immersion depth by adjusting the beaker height with a resolution of 10 μm (Thorlabs LJ750).

The Ellis2 external package for Igor Pro was used for impedance curve fitting. PEDOT:PSS EIS data was fit using the equivalent circuit shown in Figure 4.3. The circuit consists of two Randles circuits in series with a third resistor for the electrolyte resistance. A similar model has been previously proposed for conductive polymer films [211, 212]. The authors used Voigt elements by changing the capacitors to constant phase elements (CPE). The CPE models a nonideal capacitor with a power coefficient between 0 and 1, where 1 is for an ideal capacitor. However, results found that the power coefficient was $>$ 0.95, indicating near ideal capacitor behavior. The resistor in each Randles circuit models the charge transfer resistance. One Randles circuit represents the impedance due to the double layer capacitance at the polymer/electrolyte interface while the second Randles circuit models the hole/ion diffusion within the polymer up to the gold substrate [133, 213]. Representative fits using this circuit are shown in Figure 4.4. Frequencies between 300 Hz and 10 kHz were used for fitting since the model was found to converge faster and yielded more consistent residuals. The impedance magnitude at 1 kHz was found by interpolation between the frequencies of 967 and 1170 kHz.

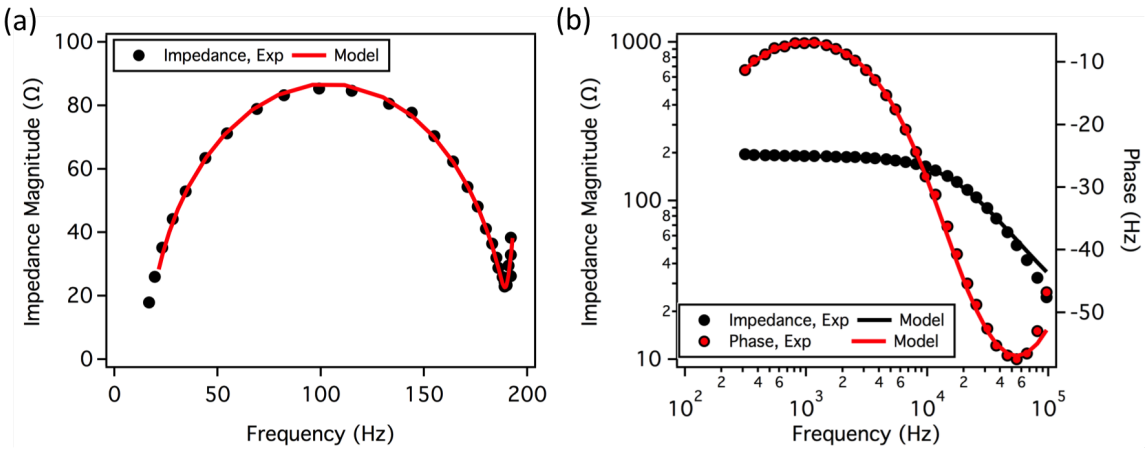


**Figure 4.4:** Representative electrical impedance spectroscopy data presented in a Nyquist plot for 50 mC $cm^{-2}$ PEDOT:PSS. EIS was obtained for n = 3 trials for each charge density as well as bare gold.

### 4.2.7 Cyclic voltammetry

A Keithley 2400 sourcemeter controlled using Igor was used to perform a voltage potential sweep for cyclic voltammetry. A custom Ag/AgCl reference electrode and a coiled platinum counter electrode were used and placed in a 10 mL microscope dish with HEK extracellular as the electrolyte medium. The working electrode was vertically inserted into the electrolyte using a micromanipulator, similar to the film deposition arrangement. Voltage was swept between -0.6 V and +0.8 V vs. Ag/AgCl at a scan rate of 500 V $s^{-1}$.

### 4.2.8 Human Embryonic Kidney (HEK) cells

Human embryonic kidney (HEK) cells were thawed from cryo storage. HEK cells were cultured in MEM + 10% FBS and incubated at 37 °C and 5% CO2. HEK cells used for stimulation experiments were cultured on coverslips pre-treated with PDL. Coverslips with cells were culture in 12-well plates with 2 mL of medium and used within 3 – 4 days of initial seeding. HEK extracellular medium was used for all experiments unless otherwise noted. Glass pipettes were filled with HEK intracellular medium for patch clamp experiments only.

### 4.2.9 Patch clamping

Patch clamping was performed using the same system and software programs used for potential field mapping. Patch pipettes were pulled using a Sutter P1000. Pipettes were filled with 20 μL of HEK intracellular solution. Pipette potential and parasitic capacitance was nulled when the tip was near the testing region. Pipettes with resistances between 2 and 8 MΩ were used. A fresh pipette was used for each cell experiment. A coverslip containing HEK cells was placed in the polystyrene dish and held in place using a small amount of silly putty.

### 4.2.10 Uniform electric field mapping

Surface impedance is dependent on the material and condition at the electrode/electrolyte interface and is significant factor in determining electric field generated by a voltage-excited electrode in solution. A 50 mm polystyrene petri dish filled with 40 mL of HEK extracellular solution at room temperature was used for all experiments. A mobile glass pipette electrode, typically used for patch clamping, was employed here to directly measure local field potentials generated by polymer and gold electrodes with an applied voltage. Two straight 0.2 x 8 mm wires were attached to micromanipulators and oriented parallel with respect to each other. An upright microscope with a 40x water immersion objective was used to view the electrodes. Wires were placed 400 μm apart to create a uniform electric field. All distances were measured by translating the pipette tip with a three-axis piezoelectric manipulator and reading out displacement using LinLab 2 (Scientifica software). A 1 kHz sine wave with an amplitude between 0.1 and 1 V was applied between each set of electrodes using an external stimulator (World Precision Instruments, DS8000) and stimulus isolator (World Precision Instruments, DLS100). The local field potential was measured from the pipette with respect to a distant Ag/AgCl electrode in solution. The peak-to-peak voltage potential was measured using an in-house Labview program. Potential was recorded at distances between 25 and 375 μm from the edge of one electrode at

25 μm increments. Potential maps were obtained for three different pairs of bare gold, SAM-coated gold, and 50 mC $cm^{-2}$ PEDOT:PSS-coated gold electrodes. All experiments were carried out inside of a wire mesh faraday cage to reduce electric noise to below 1 mV peak-to-peak.

#### 4.2.11 HEK cell stimulation

Before patching, one of the polymer wires (i.e. the working electrode) was fixed such that the tip was 10 μm above the substrate at the edge of the cell. The mobile counter wire was manipulated using a Scientifica 3-axis piezoelectric micromanipulator with a resolution of 100 nm. The tip of the counter wire was also positioned 10 μm above the substrate and initially placed at a tip-to-tip distance of 25 μm from the working electrode. The patch pipette pressure was then set to atmospheric and lowered to form a gigaseal on the membrane of the target cell. A gigaseal was achieved when the pipette resistance measured between 1 – 4 MΩ. The pipette potential and capacitance was nulled again after a gigaseal was achieved. A 1 kHz, 1 V amplitude sine wave was applied between the polymer wires or gold electrodes using an external stimulator for all experiments. Pipette potential was recorded during stimulation in the gigaseal state to determine the potential contribution due to parasitic capacitance of the pipette. Recordings were taken during stimulation for counter wire distances of 25, 50, 100, and 500 μm defined with respect to the tip of the wire fixed at the end of the cell membrane. The results of these measurements are referred to here as 'sealed.' The peak-to-peak potentials measured in the sealed state were assumped to be due to parasitic capacitance of the pipette and were subtracted from peak-to-peak values measured in the patch state. A negative pressure pulse was applied to the pipette to break into the HEK cell. Break-in was determined when the pipette resistance dropped below 100 MΩ and a stable negative membrane potential was observed (typically near -50 mV). Pipette potential measurements were then repeated in the 'patched' state with the same stimulation parameters and at the same counter wire distances as performed in the sealed

state. Finally, a high positive pressure was applied to the pipette to burst the cell with the pipette in place. Pipette potential measurements were then repeated in the 'broken' state with the same stimulation parameters and at the same counter wire distances as performed in the sealed and patched states.

All voltage potential data was captured in current clamp mode at a rate of 40 kHz for a total of 9 seconds, which was divided into 3 acquisition files. Images of the cells during each recording were captured. Potential measurements were taken without stimulation for each cell and found to be less than 1 mV peak-to-peak in all cases. All pipette potential data was analyzed using a custom Igor Pro script. Peak-to-peak values for each experiment were averaged over the 9 second interval ($\sim$9000 periods). The change in cell membrane potential was determined by subtracting the sealed from the patched peak-to-peak potential values. Stimulation experiments were carried out using different sets of electrodes including: bare gold, SAM-coated gold, PEDOT:PSS stubs, and PEDOT:PSS wires.

### 4.2.12 COMSOL modeling

#### *4.2.12 Surface impedance calibration*

Experimental uniform field results were used to calibrate the COMSOL model through surface impedance values. The slope of the potential measurements (i.e. electric field) for each set of parallel wires was found using linear regressions. A COMSOL model was generated using two 0.2 x 8 mm cylinders spaced 400 μm apart. Material properties and boundary conditions were similarly applied as described in the COMSOL modeling section of the methods. Potential values from the model solution were exported and fit using a linear regression to find the value of the resulting uniform electric field. The surface impedance for each electrode in COMSOL was tuned until the slope of the simulated electric field matched the experimental electric field within 1%. This process was conducted for three sets of electrodes for each of the three difference surface treatments: untreated gold, 50 mC $cm^{-2}$ PEDOT:PSS, and SAM-coated gold.

Polymer stubs and wires were oriented perpendicular to each other at a tip-to-tip separation of 100 μm. A 1 V, 1 kHz sine wave was applied between the electrodes for all mapping experiments. Local field potentials were measured at 432 positions over a 100 by 100 μm square area with one side along the axial center between the electrode or wire tips. Coordinate positions were designated in LinLab 2 to enable automatic positioning for mapping experiments. Pipette positions and peak-to-peak voltage potentials were synchronously tracked by taking a screen capture video at a frame rate of 20 fps using VLC.

The model for polymer stub experiments was corrected by using a manual algorithm to alter the surface impedance values of the gold electrodes and the PEDOT:PSS. The electrodes were assumed to have a similar surface impedance and were thus changed simultaneously. The impedance of the PEDOT:PSS features on each electrode were independently tuned since different diameters may have had different effective impedance values. It was observed that the polymer impedance had little effect on the slope of the axial potential profile along x = 100 μm. It was assumed that this profile represented the slope of the uniform field attributed to the gold electrodes (Figure 4.15c). The surface impedance of both electrodes were tuned until the potential slope along this profile matched within 1% of the slope obtain experimentally. Next, the surface impedance of each PEDOT:PSS stub or wire was tuned until the electric field differential error was no more than 500 V $mm^{-1}$ between y-coordinates of 5 and 95 μm. The PEDOT:PSS impedance was found to slightly alter the axial potential profile along x = 100 μm. The impedance value of the gold electrodes were refined once again until the slope along the x = 100 μm was, again, within 1%. The values of surface impedance of the electrodes and of the polymer were recorded for n = 8 stubs.

### *4.2.12 Cell membrane potential*

COMSOL multiphysics simulation software version 5.2a or later was used for all computations. All model components shown in Figure 4.5 were built within COMSOL and assigned the material properties shown in Table 4.1 unless noted otherwise.

**Table 4.1:** COMSOL input parameters.

| Component (-) | Geometry (-) | Material (-) | Conductivity (S $cm^{-1}$) | Surface impedance (ohm $m^2$) | Permittivity (-) |
|---|---|---|---|---|---|
| Glass coverslip | Cylinder | Glass | 0.015 | | |
| PEDOT:PSS wires | Cylinder + hemisphere | PEDOT:PSS | 38 | | |
| Gold electrodes | Cone | Gold | | | |
| Cell | Half-ellipsoid | HEK extracellular | | | |
| Insulating caps | Hemisphere | HEK extracellular | | | |
| Extracellular buffer | Cylinder | HEK extracellular | | | |



**Table 4.2:** COMSOL mesh parameters.

| Component (-) | Max. element size (μm) | Min. element size (μm) | Max. element growth rate (-) | Curvature factor (-) | Resolution of narrow regions (-) |
|---|---|---|---|---|---|
| PEDOT:PSS wire surface | 5 | 0.25 | 1.3 | 0.2 | 1 |
| Gold electrode tip | 5 | 0.05 | 1.3 | 0.2 | 1 |
| Cell surface | 5 | 0.05 | 1.3 | 0.2 | 1 |
| Remaining | 153 | 19.2 | 1.3 | 0.5 | 0.6 |

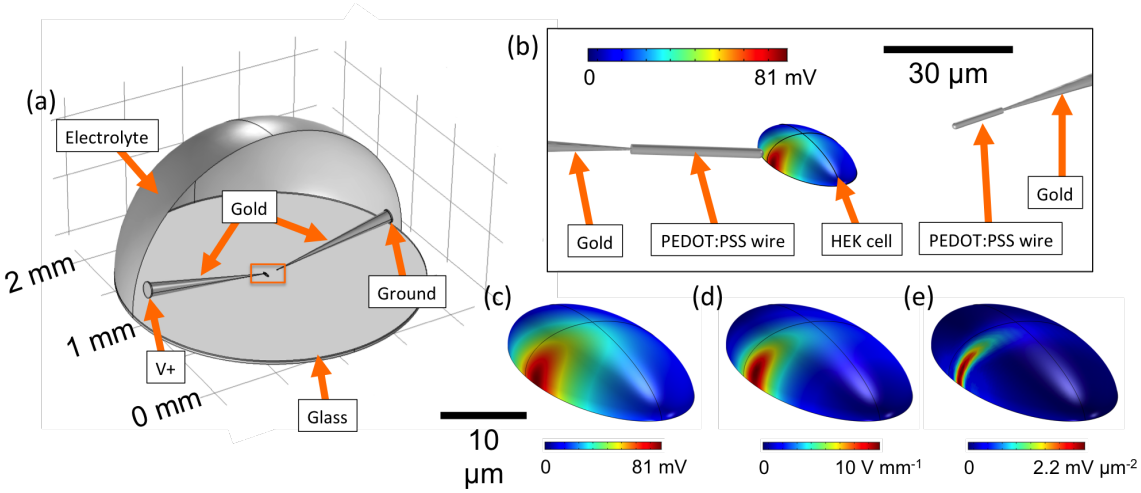


**Figure 4.5:** (a) Schematic of the COMSOL model used for simulating cell membrane potential changes in response to applied field generated by PEDOT:PSS stubs or wires. (b) Magnified view of model with cell and PEDOT:PSS wires at the ends of gold electrodes. COMSOL surface plot of (c) potential, (d) electric field, and (e) electric field gradient at the cell membrane.

The overall dimensions of the model varied based on the arrangement of electrodes but was no smaller than 2 mm in diameter. Physical dimensions of wires and electrodes were obtained by measuring the full width half maximum of line profiles from brightfield microscope images in ImageJ. Gold electrodes were approximated as cones with an aspect ratio of that obtained from corresponding images and assuming a tip diameter of 50 nm. PEDOT:PSS wires were modeled as cylinders with a hemisphere at the tip. PEDOT:PSS wires were assumed to overlap the gold electrode about 5 µm. The cell was not modeled as a separate component, but rather as a half ellipsoid surface with the same properties as the extracellular buffer. The potential at the cell membrane was evaluated as an average over this surface area of the half ellipsoid. All cells were assumed to have a height of 5 µm. The length and width were estimated from brightfield images. Electrodes with wires were angled 10 degrees with respect to the glass substrate. The tip of each wire or electrode was placed at the closest edge of the cell membrane at a vertical height of 10 µm above the substrate. The model was solved using the electrostatics physics module in COMSOL, which solves the model using the Poisson equation for a given set of boundary conditions. Voltage potential boundary conditions were applied to the base surface of each gold electrode cone. Since only 1 mm of the electrode length was modeled, a virtual insulator was placed at the backside of the surface boundary conditions to eliminate nonphysical current

from shorting around the model. A course mesh was used for the bulk of the model with refined surface meshes at the regions of interest (e.g. at polymer and electrode tips). The mesh parameters are listed in Table 4.2. Mesh size was optimized to yield solution values within 1% convergence.

## 4.3 Results and discussion

### 4.3.1 Electrical impedance spectroscopy

Electrical impedance spectroscopy (EIS) is a method by which a low amplitude alternating sinusoidal potential is applied between an electrochemically active surface and large inert counter electrode. The amplitude and phase shift of resulting current waveforms are captured for a range of excitation frequencies. The frequency dependence of impedance can then be modeled with an equivalent circuit elements to reveal electrochemical characteristics of the surface such as specific capacitance and charge transfer resistance. These elements arise from charging and discharging the electric double layer and faradaic processes. Here, EIS was used to determine the necessary charge deposition density of PEDOT:PSS to ensure a low surface impedance. The resulting surface impedance value from EIS was also used for comparison to that obtained via local field potential mapping.

PEDOT:PSS was electro-deposited onto 200 μm diameter gold wire at a current density of 13 nA $mm^{-2}$. Impedance spectroscopy was performed for gold surfaces treated with charge deposition densities of 0, 2, 10, 20, and 50 mC $cm^{-2}$. The sinusoidal excitation had a magnitude of 400 mV vs. Ag/AgCl and a frequency range between 1 Hz and 100 kHz. Real and imaginary impedance values at each frequency for bare gold and 50 mC $cm^{-2}$ PEDOT:PSS are plotted in the Nyquist plots shown in Figure 4.6. Note that the frequency of each data point decreases from left to right. Thus, the lowest impedance is exhibited at the highest frequency in which current is 'shorted' through the electric double layer capacitance. Impedance eventually increases with frequency in a linear fashion, which is termed the Warburg impedance. At these low frequencies, faradaic currents become diffu-

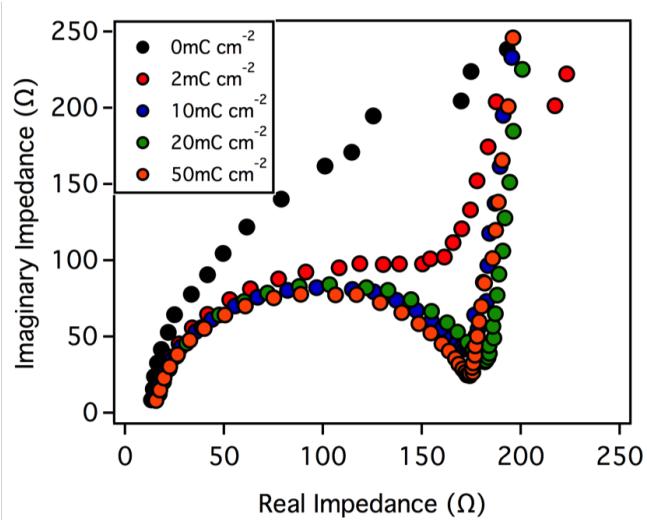


**Figure 4.6:** Representative electrical impedance spectroscopy data presented in a Nyquist plot for bare gold and various charge deposition densities of PEDOT:PSS.

sion limited and impede charge transfer. The impedance spectra for bare gold was nearly linear for the majority of the frequency range. Thus, Gold exhibits Warburg impedance at a relatively high frequency, which indicates that charge transfer for gold is dominated by faradaic processes (e.g. electrolysis) instead of double layer capacitance. Faradaic currents can be largely irreversible, which leads to permanent electrochemical degradation and local pH changes, which can have adverse consequences in biological environments. This is a well-known reason why gold is not a preferable microelectrode material.

A semi-circle shape is observed for PEDOT:PSS prior to the linear Warburg impedance region shown in Figure 4.6. This result indicates that PEDOT:PSS has a relatively large specific capacitance compared to gold, which yields a lower overall surface impedance. There are two main differences between gold and PEDOT:PSS that enable a higher specific capacitance. First, the porous nature of the polymer surface (Figure 4.7) increases the electrochemical surface area, which increases the double layer capacitance. Second, the polyelectrolyte complex of PEDOT and its counter-ion PSS, provides an additional charge transfer mechanism that is considered to be pseudo-faradaic. Briefly, the positively doped PEDOT polymer forms an electrostatic complex with the negatively charged PSS counter-ion. An applied potential converts the doped PEDOT to undoped PEDOT, at which point the PSS counter-ion subsequently dissociates into solution. The advantage of this process

is that it is considered to be reversible since the PSS polymer is embedded into the PEDOT polymer matrix and not likely to diffuse away from the surface. This is why PEDOT:PSS is considered to be pseudo-capacitive and is safer for biological applications while lowering surface impedance for higher electric field generation at a given voltage than most materials.

Power coefficients for CPEs were found to be greater than 0.95, which suggests that the CPE elements used to model PEDOT:PSS are nearly ideal capacitors. Thus, the general Voigt models can be replaced with two Randles circuits as shown in Figure 4.3. Representative fits from each circuit are shown in Figure 4.4. Frequencies between 300 Hz and 10 kHz were used for fitting since the model was found to converge faster and yield more consistent residuals. The impedance magnitude at 1 kHz was found by interpolation between the frequencies of 967 and 1170 kHz. The standard frequency of interest for bioelectrode interfaces is 1 kHz. The surface impedance values at 1 kHz for PEDOT:PSS and gold are plotted in Figure 4.7 as a function of charge deposition density. No additional reduction in impedance was found beyond 20 mC $cm^{-2}$, but the variance of surface impedance for 50 mC $cm^{-2}$ PEDOT:PSS surfaces was reduced. These trends are consistent with previous studies of PEDOT:PSS films [143, 214]. A charge deposition density of 50 mC $cm^{-2}$ was chosen as the model PEDOT:PSS interface for all further studies.

For time dependent model studies in COMSOL, it is necessary to have approximate values of specific capacitance and surface resistance. EIS results for PEDOT:PSS were modeled using two Randles circuits in series. The equivalent circuit used for fitting using the Ellis2 curve fitting package in Igor Pro is shown in Figure 4.3. The circuit is composed of a series resistor and two series circuits each consisting of a resistor and capacitor in parallel.

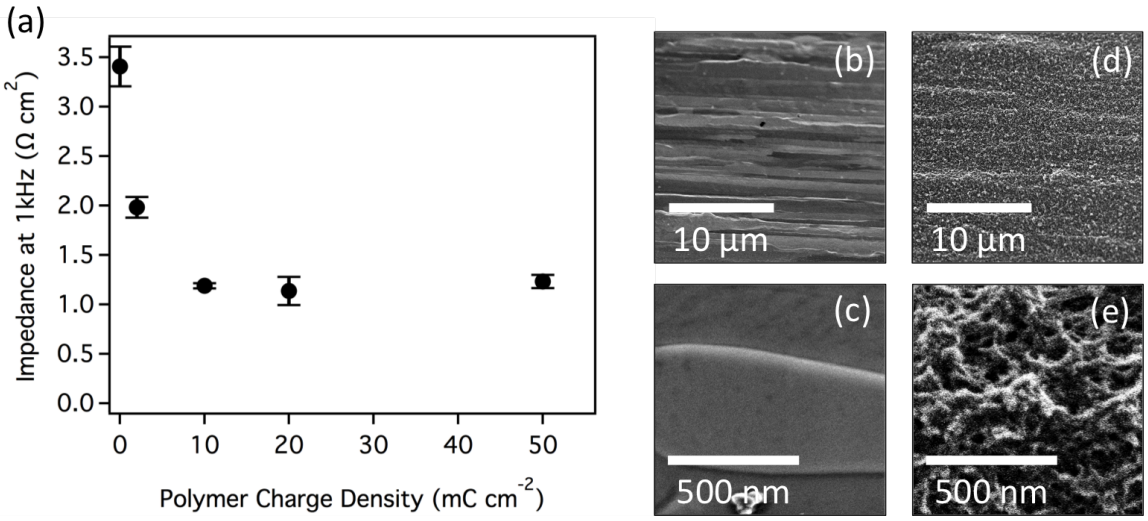


**Figure 4.7:** (a) Surface impedance at 1 kHz from electrical impedance spectroscopy as a function of PEDOT:PSS charge deposition density onto gold (n = 3 for each charge density; error bars represent ± 1 standard deviation). Scanning electron micrographs of (a) (b) bare gold and (c) (d) gold deposited with 50 mC cm$^{-2}$ of PEDOT:PSS.

### 4.3.2 Scanning electron microscopy

Scanning electron microscopy (SEM) images were captured for the different PEDOT:PSS charge deposition densities tested to confirm that differences in results are indeed related to varying amounts of deposited polymer. SEM images for all tested surfaces are shown in Figure 4.7. Bare gold displayed multiple grain boundaries with smooth surfaces. A PEDOT:PSS charge deposition density of 2 mC cm$^{-2}$ was visible, but did not exhibit full surface coverage. Large amounts of polymer with a porous structure were seen at a charge density of 10 mC cm$^{-2}$. Differences in surface morphology were indistinguishable beyond 20 mC cm$^{-2}$, but film thickness was noticeably higher from 20 to 50 mC cm$^{-2}$; the gold surface texture was less visible. These results are consistent with the observation that surface impedance is at a minimum with little variation between 20 and 50 mC cm$^{-2}$.

### 4.3.3 Cyclic voltammetry

Cyclic voltammetry (CV) is a common electrochemical characterization method that measures current while applied potential amplitude is swept. Bare gold and PEDOT:PSS were tested at a scan rate of 500 V s$^{-1}$ between -0.6 and +0.8 V referenced to a Ag/AgCl electrode. This potential range is defined for safety and deemed the electrochemical water

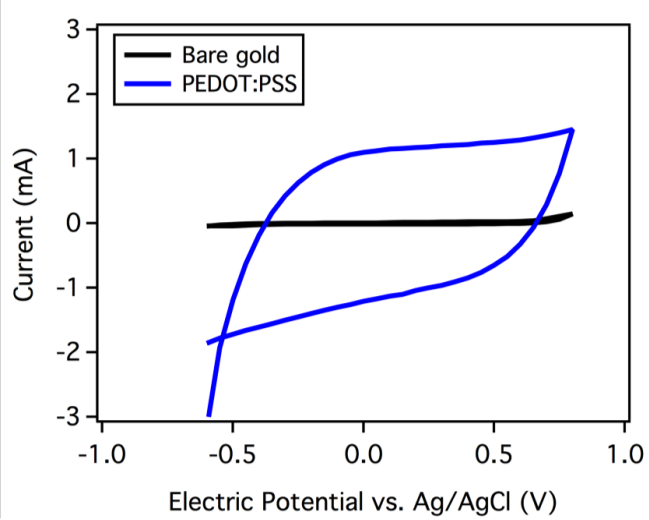


**Figure 4.8:** Representative cyclic voltammagram of bare gold and PEDOT:PSS in physiological buffer

window, which is the range in which electrolysis does not yet occur [131]. A coiled platinum wire served as the counter electrode. A representative CV plot is shown in Figure 4.8. There were two important observations when comparing bare gold vs. PEDOT:PSS coated gold. First, the difference in current for PEDOT:PSS during forward and reverse potential sweeps indicated a larger reversible current when compared to gold, which does not. This evidence supports the well-known conclusion the PEDOT:PSS has a higher charge storage capacity compared to bare gold. Second, it is important to note that electrochemical current for the gold interface did not begin to increase until high potential magnitudes were applied. This was due to the fact that gold cannot transfer charge to the electrolyte until the minimum potential for electrolysis was achieved (i.e. lower than -0.6 V and higher than +0.8 V vs. Ag/AgCl).

### 4.3.4 Uniform field potential mapping

A simplified equivalent circuit for a voltage applied between two electrodes in an electrolyte is shown in Figure 4.9. Series electrical resistance due to each electrode material is shown as $R_{e1}$ and $R_{e2}$. For most of the experiments here, these terms are very small, but thin PEDOT:PSS wires do introduce significant series resistance. The surface impedance at each electrode interface, $Z_{s1}$ and $Z_{s2}$, is represented by a complex impedance element

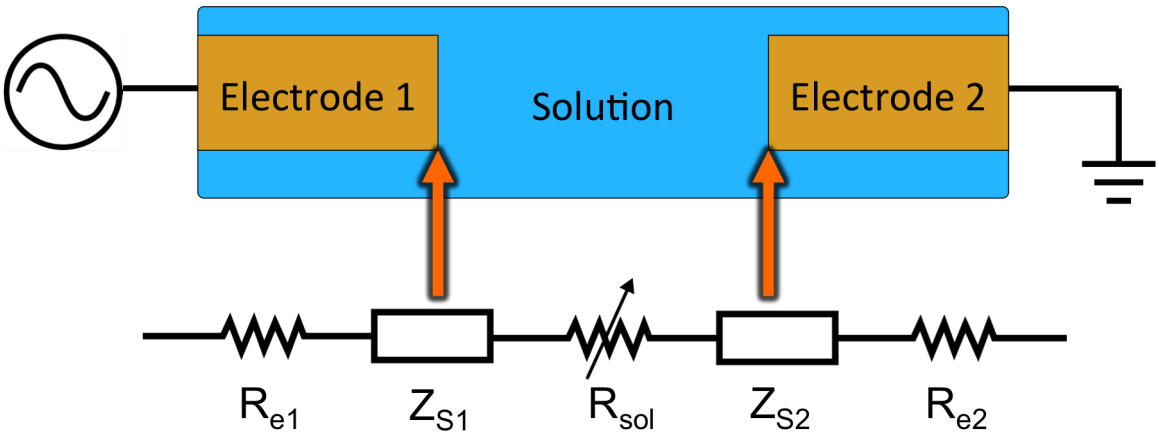


**Figure 4.9:** Equivalent circuit model used for COMSOL simulations. Equivalent circuit used to model quasi-static field conditions from experimental results where $R_e$ and $R_{sol}$ are the series resistance values for each electrode and across the solution, respectively. $Z_s$ represents the surface impedance at each electrode and is dependent upon the electrode surface chemistry as well as the voltage and frequency of stimulation.

since it is dependent on the frequency of the excitation waveform. Finally, the solution resistance, $R_{sol}$, is modeled as a variable resistor in series. The resistance of the solution depends on the conductivity and the length of solution separating the electrode interfaces. The solution conductivity was found to be 1.59 S $cm^{-1}$ using a flow cytometer (BD Accuri). It is important to note that at an infinite separation distance between the electrodes, the solution resistance will dominate the voltage drop while the voltage drop due to surface impedances and electrode resistances become increasingly negligible. The conductivity of gold, PEDOT:PSS, and the electrolyte solution are already known or previously determined. Surface impedance is the only unknown value for bare gold and PEDOT:PSS interfaces.

Two 8 mm long gold wire electrodes were positioned parallel and separated by 400 μm in electrolyte (Figure 4.10). The long length relative to the separation distance generated a uniform electric field with an applied potential, similar to a parallel plate capacitor. The goal here was to determine the surface impedance values from COMSOL in which the experimentally observed field results closely matched the modeled field results. Using a simplified geometry with a uniform field minimized geometric-related errors in the model. A continuous 1 kHz sinusoidal voltage was applied between the two parallel wires with

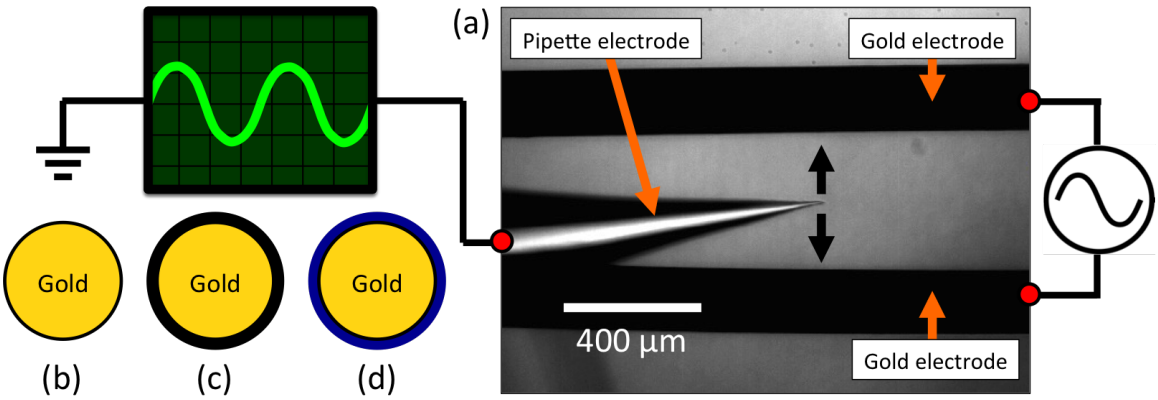


**Figure 4.10:** (a) Microscope image and schematic of experimental setup used to map voltage potential field between parallel electrodes spaced 400 µm apart in extracellular solution. A 1 kHz sine wave with a 1 V amplitude was applied between two parallel gold electrodes that were (b) uncoated, (c) coated with an insulating SAM, and (d) coated with PEDOT:PSS at a charge density of 50 mC cm-2. The peak-to-peak voltage potential was recorded with a mobile patch pipette electrode between the parallel electrodes.

the following amplitudes: 100, 200, 500, 750, and 1000 mV. A glass pipette electrode with a resistance around 4 MΩ, was placed in current clamp mode and nulled with no applied potential. Peak-to-peak voltages from noise were less than 1 mV for all experiments. Once the sinusoidal voltage was applied, the pipette electrode was scanned between the two parallel wires. The measured peak-to-peak potential was recorded at positions scanned from 25 to 375 µm and then back to 25 µm in 25 µm increments between the wires. The potential was read using a custom Labview program that reports potential while in zero current clamp mode. The pipette position was recorded from the Scientifica software program LinLab 2. In addition to bare gold and 50 mC $cm^{-2}$ PEDOT:PSS, gold coated with an insulating self-assembled monolayer (SAM) was tested as a negative control.

Since peak-to-peak potentials were measured, all results were divided by 2 to obtain potential magnitude with respect to the Ag/AgCl solution ground electrode. Representative results from SAM-coated gold, bare gold, and PEDOT:PSS-coated gold are shown in Figure 4.11. Positions at 0 and 400 µm represent the surfaces of each gold wire. The slope for each of the tested surface materials was found to be linear, which indicates that a uniform electric field was generated. Assuming perfectly symmetrical electrodes and zero surface impedance, the theoretical maximum potential would be 500 mV with a value of

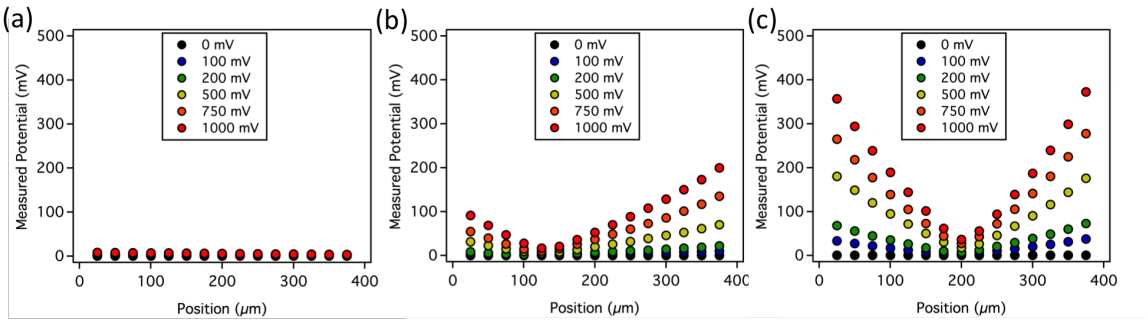


**Figure 4.11:** Representative plots of measured potentials generated by a 1 kHz, 1 V amplitude sine wave applied between parallel gold electrodes that were (a) SAM-coated gold, (b) uncoated gold, and (c) gold coated with PEDOT:PSS at a charge density of 50 mC $cm^{-2}$.

zero at 200 μm. All potentials were found to be below the theoretical maximum, which indicates the presence of surface impedance. The lowest potential drop across the solution was observed for the SAM-coated electrodes as expected. The bare gold demonstrated about half the potential drop than that observed from the PEDOT:PSS-coated gold. Thus, PEDOT:PSS generates about twice the electric field magnitude for a given excitation voltage.

Lumped surface impedance values for each surface at 1 kHz was determined using COMSOL by matching the modeled electric field to the experimentally observed electric field for an applied potential amplitude. Two 8 x 0.2 mm cylinders separated by 400 μm were used to model the parallel wire experiment as shown in Figure 4.12. One ground and one positive potential boundary condition was used for each cylinder and were located at opposite ends of the cylinder electrodes with respect to each other. Each surface potential boundary was encapsulated in an insulated cylindrical cap to force current through the gold wires (i.e. prevent unrealistic boundary shorting). Everything was then encapsulated and subtracted from a larger cylinder serving as the conductive electrolyte solution. A fine mesh was used for the entire geometry with a finer mesh refinement applied to the surface of the electrodes (defined in Table 4.2). A stationary, steady-state solver was used to obtain the solution. The surface impedance for both electrodes in each pair was assumed to be the same (i.e. averaged together).

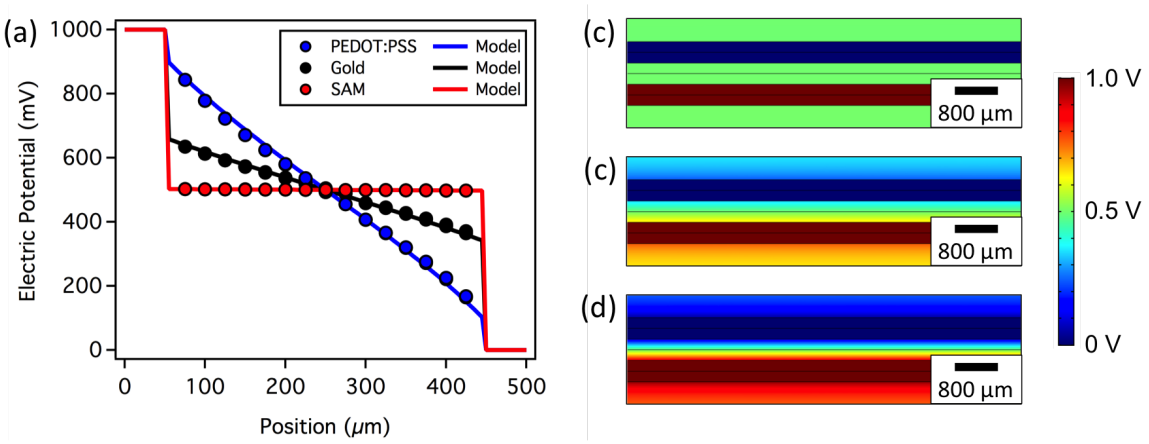


**Figure 4.12:** (a) Experimental and simulated electric potential values are plotted as a function of position between the large gold electrodes where 50 and 450 μm are the edge positions of each electrode. Field potentials generated by COMSOL between (b) SAM, (c) gold, and (d) PEDOT:PSS electrodes. The model was matched to experimental results by tuning surface impedance at each electrode surface until the model generated potential field curves with slopes within 1% of the obtained experimental values.

The slope, or electric field, was found for each pair of wires at 100, 200, 500, 750, and 1000 mV using a linear regression. Two overlapping sine waves with a slight phase shift and opposite polarity were observed when potential was measured near the zero potential. Four data points centered around the apparent zero potential location were removed prior to linear fitting to minimize peak-to-peak measurement error of the overlapping waves. All electric fields were linear with a minimum $R^2$ value $> 0.9$. Any slight nonlinearities seen in the experimental electric field were symmetrical and also present in the modeled results. Therefore, a linear regression was a suitable method for matching the model to the experimental results. The surface impedance for each pair of electrodes in COMSOL was adjusted until the electric field matched the experimental field within 1% (typically to the nearest 0.01 $\Omega$ cm$^2$).

Surface impedance results for each of the 3 surface materials are shown in Figure 4.13 across the tested voltage range. The surface impedance increased in the following order: SAM $>$ gold $>$ PEDOT:PSS. For a 1 kHz sine wave with an amplitude of 1 V, impedance was determined to be 268 $\pm$ 37, 2.43 $\pm$ 0.19, and 0.23 $\pm$ 0.05 $\Omega$ cm$^2$ for SAM, gold, and PEDOT:PSS, respectively. These are the first surface impedance values to be obtained using local field potential measurements and are comparable to values reported in literature

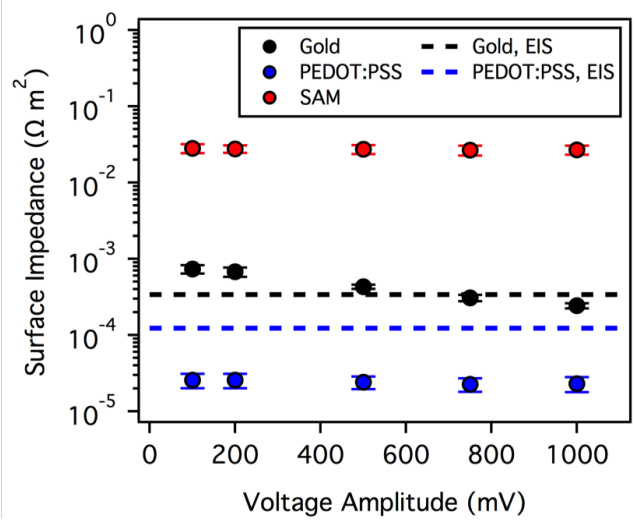


**Figure 4.13:** Surface impedance values obtained by matching COMSOL models to experimental field results for gold, gold/PEDOT:PSS, and gold/SAM. Surface impedance is plotted as a function of sinusoidal voltage amplitude. n = 3 for each point; error bars represent $\pm$ 1 standard deviation.

for PEDOT:PSS.

Gold surface impedance nearly tripled from 2.43 $\pm$ 0.19 to 7.38 $\pm$ 0.93 $\Omega$ cm$^2$ as the voltage amplitude was decrease from 1 to 0.1 V. Significantly higher currents generated at higher voltages further supports the potential-dependent faradaic charge transfer mechanism of gold. This observation is consistent with the results obtained from cyclic voltammetry and EIS. PEDOT:PSS only exhibited a slight 12% increase in surface impedance from 1 to 0.1 V, again, supporting its large reversible charge storage density. The slight increase was probably due to faradaic reactions occurring at the underlying gold substrate, which was partially accessible due to the porosity of PEDOT:PSS. The surface impedance of the SAM-coated gold was the most consistent across the applied voltage range with only a 5% change. The thiol SAM should prevent most faradaic reactions at the gold/electrolyte interface assuming perfect monolayer coverage on the gold. Therefore, the SAM strictly limits electronic/ionic transduction at the interface to the charging and discharging of the electric double layer. Double layer interactions is expected to be less voltage-dependent than faradaic reactions.

Local field potential (LFP) measurements found surface impedance values that were

higher for gold and lower for PEDOT:PSS compared to values obtained using conventional EIS. EIS results (Figure 4.7) found surface impedance for gold at 400 mV to be 3.41 $\pm$ 0.2 $\Omega$ cm$^2$. Surface impedance at 400 mV from LFP measurements were linearly interpolated and yielded a 50.4% increase with a value of 5.13 $\Omega$ cm$^2$. Since surface impedance only represents a fraction of the total impedance in the equivalent circuit (Figure 4.9), this error is not proportional to electric field error. For example, if the surface impedance values from EIS and LFP are each used in the COMSOL model for a 400 mV amplitude, an electric field difference of only 25.5% is observed for the parallel gold wire arrangement. The difference in electric field would change if the electrode geometry or separation were changed. This result highlights the complexity by which surface impedance affects electric field even for a simple electrode geometry held at a fixed distance apart and neglecting time-dependence. It is also important to note that these surface impedance values are based on geometric surface area of the parallel electrodes. Though PEDOT:PSS film thickness is no more than 1 μm, the electrochemical surface area of the porous polymer matrix is unknown. Therefore, it would be expected that these surface impedance values would overestimate impedance as the feature size of polymer structures decreases due to scaling laws.

### 4.3.5 Nonuniform field potential mapping

The goal of the following experiments was to compare 2-dimensional, nonlinear local field potential maps obtained experimentally to those predicted by the COMSOL model for PEDOT:PSS microstructures with more complex geometries. First, PEDOT:PSS polymer stubs of varying diameter are mapped at the ends of sharp gold electrodes. Second, polymer wires of varying diameter and length are mapped at the ends of sharp SAM-coated gold electrodes. For all subsequent experiments, a 1 kHz sine wave with an amplitude of 1 V was used unless otherwise noted.

PEDOT:PSS polymer stubs were synthesized as described in the methods section. Briefly, the tips of sharp gold electrodes were only immersed 15 μm or less into an aqueous solu-

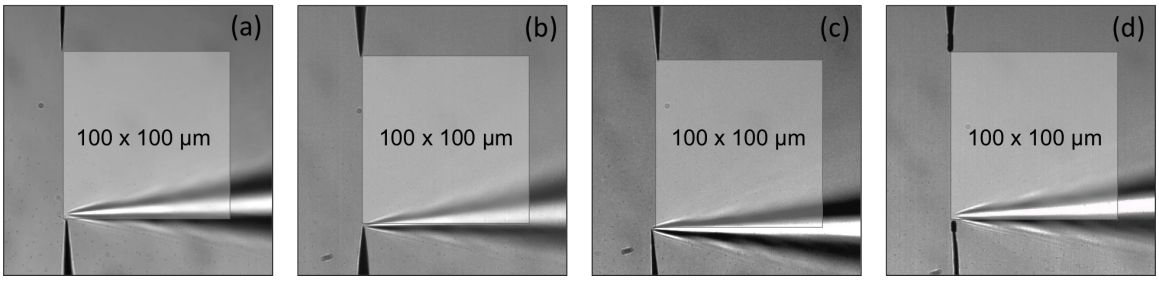


**Figure 4.14:** Microscope images showing pairs of (a) SAM-coated gold, (b) bare gold, (c) 1.9 µm PEDOT:PSS stub, and (d) 3.5 µm PEDOT:PSS stub electrodes. At the bottom right, a glass pipette recording electrode is shown, which measured potential at 432 points within the 100 x 100 µm lighter colored square region.

tion containing 10 mM EDOT monomer and 20 mM PSS polymer. A varying number of 2 s voltage pulses were applied (depending on the desired diameter) to coat the tips of gold electrodes while ensuring that the remainder of the gold was not contaminated with polymer. Electropolymerization aim to generate cylindrical polymer stubs (Figure 4.14) to produce a simple geometry that can be easily modeled in COMSOL.

Nonuniform fields were generated by separating two polymer stubs 100 µm tip-to-tip. Polymer stubs were tested in pairs in which their diameters differed by less than or equal to about 200 nm (microscopy resolution limit). Diameters between 0.5 and 4 µm were tested with typical lengths of 10 µm. LinLab 2 software was used to auto-position the tip of the glass pipette electrode from a set of pre-defined coordinates. The area mapped by the pipette was 100 x 100 µm with one side of that square area being coincident with the axial center line between the stub tips as shown in Figure 4.14. Only one side of the electrodes was mapped to avoid collision between the pipette and the electrodes. The field was assumed to be symmetrical. Video screen recordings were captured using the software program VLC to sync each peak-to-peak potential measurement in Labview with the digital position reported by LinLab 2.

Representative results from local field potential (LFP) experiments are shown for a pair of SAM, gold, 1.9 µm diameter PEDOT:PSS stub, and 3.5 µm diameter stub electrodes in the top row of Figure 4.15. Each 2D plot contains 432 LFP measurement points. Measurement points were taken 1 µm apart near the electrode tip and up to 30 µm apart at more extreme distances from the tip. The vertical axis through the origin is coincident with the

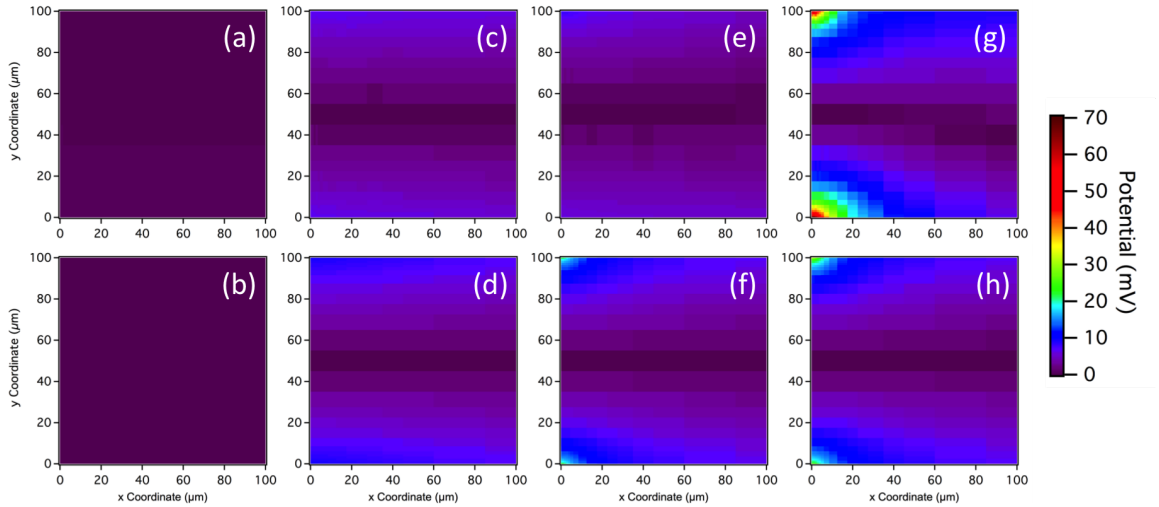


**Figure 4.15:** Representative measured (top row) and modeled (bottom row) potential field maps for (a,b) SAM-coated electrodes, (c,d) bare gold electrodes, (e,f) two 1.9 μm diameter PEDOT:PSS stubs, and (g,h) two 3.5 μm diameter PEDOT:PSS stubs.

axial centerline between the polymer stub tips. All potential values were divided by 2 to obtain the potential magnitude with respect to the Ag/AgCl solution ground electrode. For ease of comparison, potentials were offset such that the value at the coordinate x = 0, y = 50 μm was zeroed for all plots.

SAM-coated gold electrodes barely generated potentials greater than 1 mV, which is expected due to the high surface impedance of the monolayer insulation. Bare gold electrodes produced slightly larger field potentials than those coated with a SAM, but still significantly lower than PEDOT:PSS. Despite the conical geometry of the sharp, bare gold electrodes, the electric field within the mapped region resembled a uniform field. The sharp geometry did not significantly alter the shape of the resulting field due to the large impedance of the small surface area at the tip. The PEDOT:PSS stubs generated noticeably higher field potentials near their the tips. The nonuniform field shape was a result of the combination of low surface impedance and small feature size, which resembled a point source. In conclusion, PEDOT:PSS dictated the nonuniform field shape, whereas gold contributed a small magnitude uniform field.

The experimentally measured fields were compared to the COMSOL model. The model was updated using results from uniform field experiments for a 1 V, 1 kHz sine wave using surface impedance values of 268, 2.43, and 0.23 Ω $cm^2$ for SAM, gold, and PEDOT:PSS

surfaces, respectively. The gold electrode aspect ratios, polymer stub diameters, and stub lengths were recreated in the model. All electrode models were separated by a tip-to-tip distance of 102 μm assuming a pipette tip diameter of roughly 1 μm. The electrodes were vertically offset 250 μm and oriented parallel with respect to the glass substrate.

The predicted results by the COMSOL model for a the corresponding pairs of SAM, gold, 1.9 μm diameter PEDOT:PSS stub, and 3.5 μm diameter stub electrodes are presented in the bottom row of Figure 4.15. The model accurately predicted the linear axial center electric field generated by the SAM and bare gold electrodes with an electric field error of 0.002 and 0.051 V mm-1, respectively. These differences were less than 1% compared to typical electric fields generated by PEDOT:PSS stubs. The model generally did not accurately reproduce the electric fields generated by PEDOT:PSS. Additionally, the error was not consistent and was found to depend on the size of the polymer features. These errors likely originated from the limitations of using a static, steady-state model to predict the field potentials of polymer geometries with small capacitance.

Simulations consistently underestimated the electric field for stubs with diameters greater than 3 μm (n = 8). The apparent surface impedance was determined by correcting the model using a manual algorithm as described in the methods section. An example of the model correction procedure is shown in Figure 4.16. PEDOT:PSS stubs with diameters greater than 3 μm had an average surface impedance of $0.092 \pm 0.050\ \Omega\ cm^2$ (n = 8 stubs), which is significantly lower (p-value = 0.021) than that obtained for films by 60%. One reason for this difference could be that the initial surface impedance was found for a film thickness less than 1 on μm for 50 mC $cm^{-2}$ [774,777]. Surface properties for 3-dimensional microstructure are likely different than a film that has half the thickness and several orders of magnitude larger volume. PEDOT:PSS is also a porous polymer, so volume contributions have a more significant contribution to the field for small polymer geometries and would not be reflected in the model. The 100-fold increase in surface area-to-volume ratio of the polymer stub compared to the large polymer-coated wires also likely introduced error since

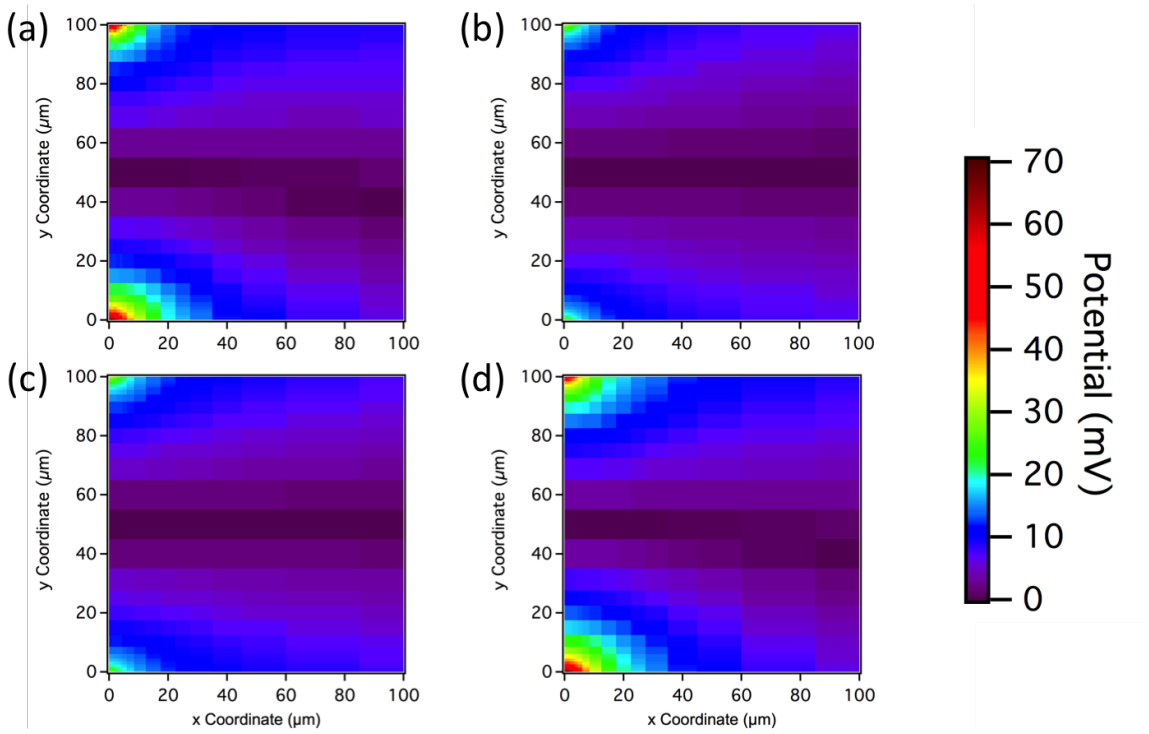


**Figure 4.16:** (a) Representative potential field map experimentally measured from two PEDOT:PSS stubs. (b) COMSOL model of the PEDOT:PSS stub, (c) after adjusting uniform field, and (d) after adjusting PEDOT:PSS surface impedance.

surface roughness was neglected in the model. Lastly, the difference could have also been due to synthesis conditions. The films were deposited on large electrodes fully immersed in monomer solution at a constant current density. PEDOT:PSS stubs were synthesized using a constant voltage onto small, high aspect ratio surfaces dipped into solution. Controlling constant current was not feasible for such small surfaces because slight thermal fluctuations of the meniscus at the electrode-solution interface constantly changed the exposed surface area. The stubs were synthesized with an approximate average current density of 100 μA $mm^{-2}$, which is roughly two orders of magnitude higher than that for the films used for LFP measurements, 2 μA $mm^{-2}$. Although, impedance differences at 1 kHz between galvanostatic and potentiostatic deposition routes were previously reported to be negligible [743].

For all pairs of PEDOT:PSS stubs with diameters greater than 3 μm, a positive error in one stub was observed with a corresponding negative error in the opposite stub. This observation was likely due to the difference in capacitance of the stubs, which would affect the

measured spatial and temporal-averaged potential. Two different capacitors in series have different potential drops. The smaller capacitor has a greater potential drop, which would manifest as a lower potential field in solution. The larger capacitor (or stub) cannot fully charge due to the smaller capacitor fully charged in series. Therefore, the field generated by the larger stub is not fully shielded. Time-dependent discrepancies will be discussed more for the small diameter stubs.

In contrast to large diameter stubs, simulations consistently overestimated the electric field generated by PEDOT:PSS stubs with diameters less than 2 μm (n = 10). Only 1 out of 10 polymer stubs was found to have a surface impedance slightly less than gold. Surface impedance values were not determined since a magnitude greater than gold was not physically probable but rather a consequence of the simplified model. One potential hypothesis is that thinner diameter stubs did not have the same surface impedance as determined by LFP measurements of films, similar to the hypothesis for thicker diameter stubs. This may account for part of the deviation but does not explain how smaller diameter PEDOT:PSS stubs could have a surface impedance greater than gold. It is more likely that the accuracy of a spatial and temporal-averaged model decreases as PEDOT:PSS feature size decreases due to the smaller absolute capacitance localized between the tips. This hypothesis is supported by the larger fields produced by PEDOT:PSS wires with the same diameter but longer length. The larger apparent surface impedance of small diameter PEDOT:PSS stubs in comparison to bare gold was likely due to a complex interaction of electrochemical faradaic reactions as a function of time. As the PEDOT:PSS pseudocapacitance charges, electrochemical potential for faradaic currents increases.

The methods section describes how PEDOT:PSS wires were grown using an alternating kilohertz square wave. Previous work has shown that polymer deposition is not completely localized at the tip. However, wire synthesis was not successful when only the tip of the gold electrode was immersed in the monomer solution. Gold wires were instead pre-coated with an electrochemically-insulating dodecanethiol SAM. A 3 V, 10 kHz square wave was

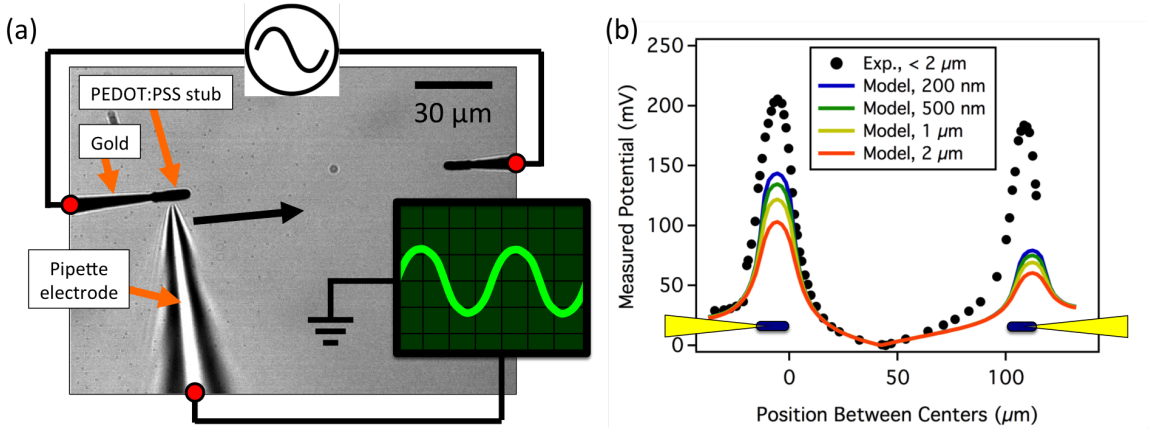


**Figure 4.17:** Representative potential field profiles from experimental and model data along the side of two 3.1 µm PEDOT:PSS stubs spaced at a tip-to-tip distance of 102 µm.

applied between two sharp, SAM-coated gold electrodes in air. The tips of the electrodes were then brought in contact to induce a localized electric short, which melted the tips. This process presumably disrupted the SAM at the tip and allowed polymer formation to occur. Small micron-sized deposits were seen at SAM discontinuities but did not significantly affect the field due to their small surface area and distance from the end of polymer wires. This assumption is supported by potential profiles along the wires shown in Figure 4.17 for experimental data and the model. Additionally, after the model was corrected, the SAM-coated gold surface impedance was determined to be $51.0 \pm 27.5\ \Omega\ \text{cm}^2$.

PEDOT:PSS wires were found to have an average surface impedance of $0.0767 \pm 0.0189\ \Omega\ \text{cm}^2$ (n = 3 wires), which was slightly lower than the value found for polymer stubs with diameters great than 3 µm. These results were contrary to those obtained for polymer stub diameters less than 2 µm. Thus, the LFP results for wires would support the explanation that the potential field at the tip depended on the volume of polymer instead of the diameter *per se*, since the wires were significantly longer than the stubs.

### 4.3.6 Single cell patch clamping in nonuniform fields

Single cell patch clamping with applied potential fields provided a method to directly measure and quantify the membrane potential in response to a time-varying electric field. Note that HEK cells do not have voltage-gated ion channels to elicit action potentials. Therefore, it was expected that HEK cell membrane potential should have been a function of potential

instead of electric field (as in the case of cardiomyocytes). The primary purpose of these experiments was to establish the method of simultaneous patch clamping and extracellular stimulation using polymer stubs and wires. Results were analyzed with respect to the average field potential at the cell predicted by the COMSOL model for different electrode materials, geometries, and locations.

A patch pipette was used to form a gigaseal onto the membrane of a HEK cell as described previously. The working electrode tip was fixed 10 μm directly above the edge of the cell membrane and the counter electrode was positioned at tip-to-tip distances of 25, 50, 100, and 500 μm. A 1 V, 1 kHz sine wave was applied to pairs of SAM-coated gold, bare gold, PEDOT:PSS stubs, and PEDOT:PSS wires separated by each of these four distances (Figure 4.18). Peak-to-peak sinusoidal potential measurements were measured in gigasealed (Figure 4.19 (b)), patched (Figure 4.19 (c)), and broken (Figure 4.19 (d)) membrane states. The positions of the patch pipette and the working electrode were fixed during all measurements.

One caveat of using a patch pipette to measure membrane potential is that the signal measured included parasitic capacitance between the glass pipette and the extracellular solution. This contribution was determined by recording potential after the pipette tip formed a gigaseal with the cell membrane (”sealed state” - Figure 4.19 (b)). Any potential recorded in a sealed state should be due to parasitic capacitance since intracellular potentials were insulated by the in tact cell membrane at the tip. After measuring potentials in the sealed state, a negative pressure was applied to the pipette to breach the cell membrane and establish the ”patched state” (Figure 4.19 (c)). Peak-to-peak potentials measured in the patched state consisted of changes in the cell membrane potential as well as parasitic capacitance. Peak-to-peak parasitic contributions measured in the sealed state (Figure 4.20 (a)) were subtracted from potential measurements in the patched state (Figure 4.20 (b)) to obtain the net change in potential due to the HEK cell (Figure 4.22). After intracellular potential measurements were measured, extracellular potential measurements were obtained by breaking

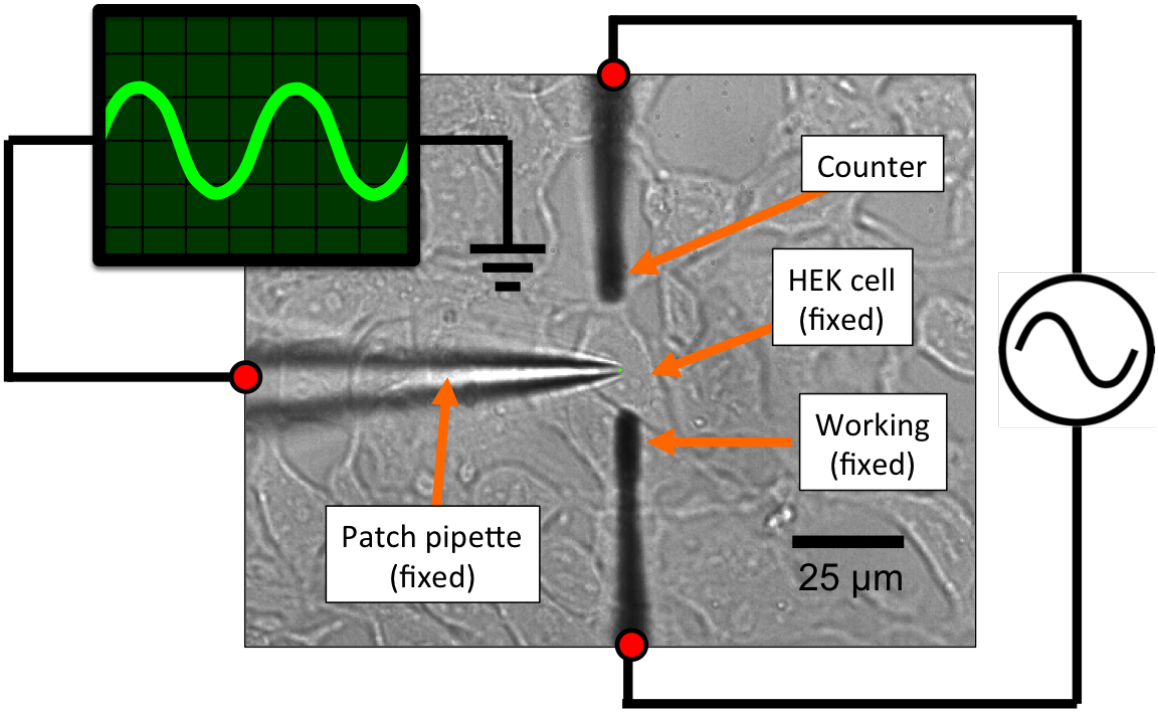


**Figure 4.18:** Microscope image captured during a representative cell stimulation experiment. A HEK cell is patched and held in current clamp mode while a sinusoidal electric field was generated by two PEDOT:PSS stubs. Peak-to-peak membrane potential was recorded while the pipette and working electrode were both fixed throughout the experiment. The counter electrode was positioned at tip-to-tip distances of 25, 50, 100, and 500 µm with respect to the working electrode.

the seal between the cell and the pipette (Figure 4.19 (d)) using a high positive pressure. Extracellular peak-to-peak measurements are shown in Figure 4.20 (c).

Membrane potential of the HEK cells should change in response to the sinusoidal changes in extracellular potential. It is beneficial to first look at how extracellular potentials changed as a function of counter electrode position. Extracellular potential at a fixed location was found to depend on the position of the counter electrode as shown by Figure 4.20 (c). This can be explained by using superposition of potential fields generated by two point sources of opposite charge. The potential from one electrode decays with the inverse of distance as given by the following equation:

$$V = \frac{I}{4\pi\sigma r} \tag{4.1}$$

where $V$ is extracellular potential, $I$ is current, $\sigma$ is conductivity of the solution, and $r$ is the distance from the electrode source. For a bipolar arrangement, which was used for these

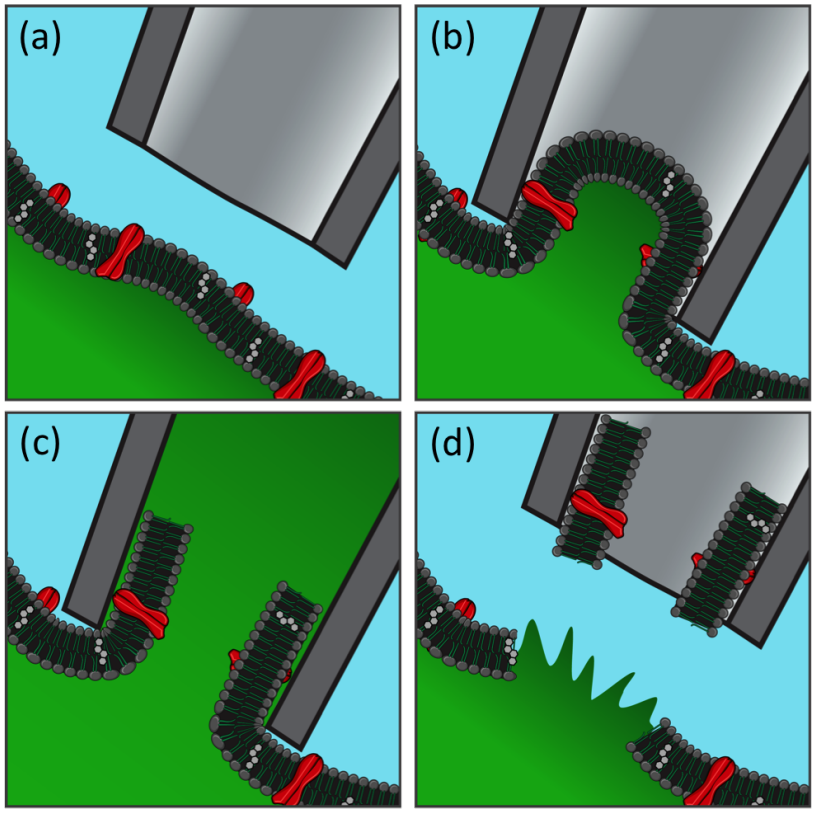


**Figure 4.19:** Magnified illustration of patch pipette interface at cell membrane (a) before gigseal seal, (b) after gigaseal (sealed), (c) patched into cell, and (d) forced detachment (broken).

experiments, superposition is used to sum the potential field contributions by each electrode. Here, the electrodes were opposite potential, so their fields destructively interacted (charge cancellation). Therefore, as one electrode was moved away from the opposite electrode, the potential near each electrode increased in magnitude since the overlap in their opposing fields decreased. The results in Figure 4.20 (c) show that in some cases the potential increased while in other cases the potential decreased as the counter electrode was separated from the working electrode. This can be explained by the relative location of the zero equipotential line (where both fields entirely canceled). For a perfectly symmetrical pair of electrodes, the zero equipotential line will always be equidistant from the tip of each electrode. Therefore, if the working electrode is fixed and the counter electrode is pulled away, the zero equipotential will appear to move towards the counter electrode to maintain its equidistant location. If the size or surface impedance of the electrodes are unequal, then the zero equipotential line will shift to one of the electrodes. In some cases, the equipotential line may have been located between to the working electrode and the pipette

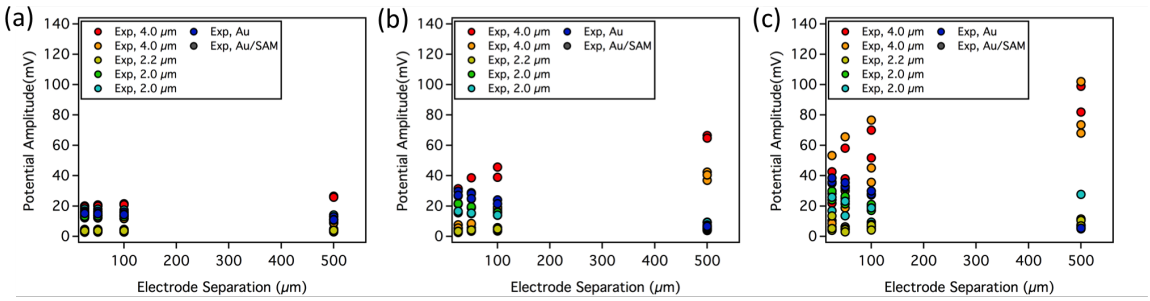


**Figure 4.20:** PEDOT:PSS stub stimulation results. Raw potential measurement data from HEK cells as a function of counter electrode position during 1 kHz, 1 V sine wave stimulation for (a) sealed, (b) patched, and (c) broken cell states. Experiments with PEDOT:PSS stubs are labeled by their diameter. Electrode separation is defined as the tip-to-tip distance between the counter and working electrodes.

electrode. In this scenario, as the counter electrode is pulled away, the potential will appear to decrease as the zero line approaches the pipette. As the counter electrode continues to be pulled away, the zero potential line will eventually pass the pipette electrode and potential will then appear to increase. This behavior was expected to hold for cell membrane potential measurements as well since the membrane potential of HEK cells primarily depended on the extracellular potential.

Raw data for measured sinusoidal potential amplitudes (not peak-to-peak) in the sealed, patched, and broken states are shown in Figure 4.20 and Figure 4.21 for PEDOT:PSS stubs and wires, respectively. The measured potentials during the gigaseal state were the lowest of the three states while the broken state generally demonstrated the highest measured potentials. Potentials measured during the sealed state were expected to be the smallest since the only contribution of current was from the parasitic pipette capacitance. Broken state potentials were the highest since the series resistance of the cell membrane was no longer present. Patch clamp potential amplitudes were in between sealed and broken state measurements with respect to magnitude. The potentials in all three states were dependent on electrode separation.

The change in membrane potential amplitude due to 1 kHz stimulation is shown in Figure 4.22. These values were obtained by subtracting patch clamping results from sealed results to obtain the change in potential of each HEK cell. The change in membrane potential generally correlated with the potential field around the cell. In most cases, the change

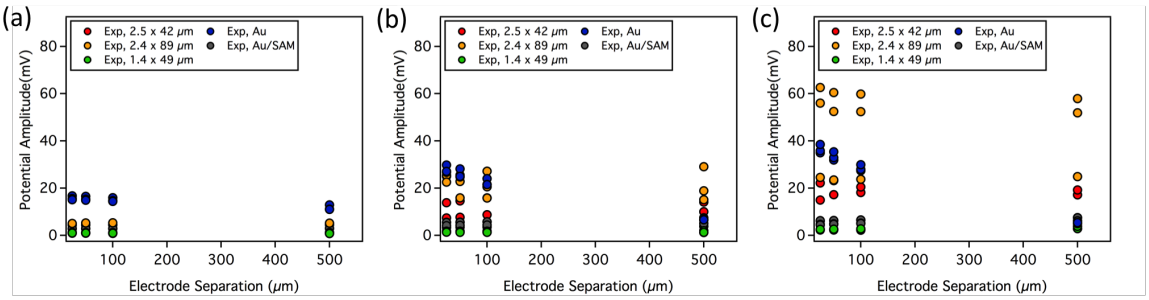


**Figure 4.21:** PEDOT:PSS wire stimulation results. Raw potential measurement data from HEK cells during 1 kHz, 1 V sine wave stimulation for (a) sealed, (b) patched, and (c) broken cell states. Experiments with PEDOT:PSS wires are labeled by their dimensions. Electrode separation is defined as the tip-to-tip distance between the counter and working electrodes.

in membrane potential increased as the counter electrode was moved farther away from the electrode fixed at the target cell. This observation is consistent with the previous observation that the total potential drop between the electrodes increased as the gap between the electrodes increased. As the solution resistance increases, its share of the total resistance, and thus the total potential, increases as shown by the equivalent circuit diagram in Figure 4.9. It is important to note that this trend suggests that HEK cell membrane potential predominantly depended on the potential magnitude near the membrane. This is contrary to neurons and cardiomyocytes that depend upon a local electric field gradient for eliciting an action potential, which decreases with increasing electrode separation [150]. The model also exhibited an increase in potential at the electrode tip due to increased electrode separation.

Interestingly, the membrane potential stimulus amplitude decreased for some electrodes/polymer stubs and increased for others when electrode separation was increased. The potential at the cell would be expected to increase with electrode separation due to the increased total solution resistance. However, since these measurements were obtained from peak-to-peak measurement values, potential amplitude was never zero. The tip-to-tip potential profile resembled a ”V” shape where the peak-to-peak potential exhibits a point of inflection at the zero potential location (i.e. absolute value). This ”V” shape was observed in uniform field potential measurements shown in Figure 4.11. The initial zero location

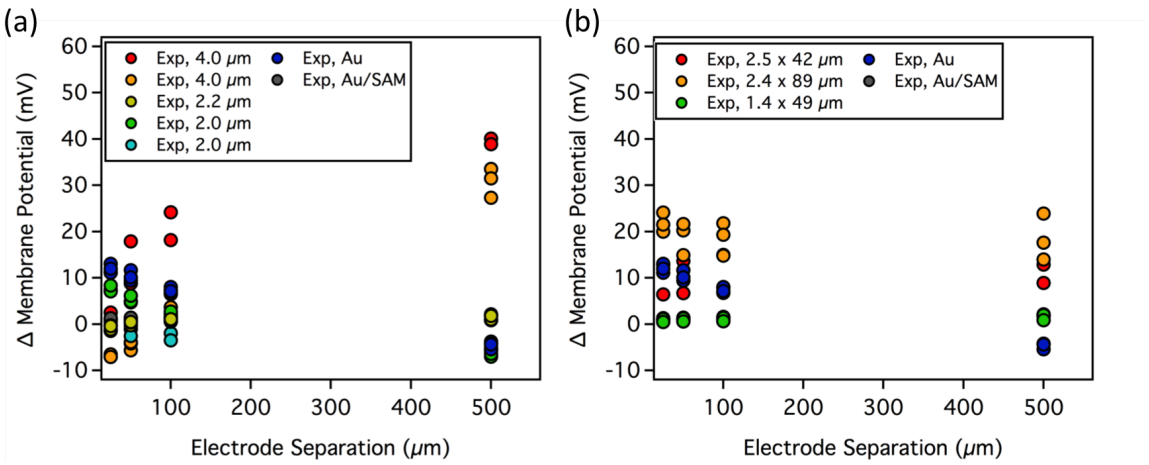


**Figure 4.22:** Change in HEK cell membrane potential due to stimulus, which was calculated by subtracting potential measurements in the sealed state from the patched state. Results are shown for PEDOT:PSS (a) stubs and (b) wire. Both are compared to bare gold and SAM-coated gold.

depends on the surface impedance and surface area of each electrode; it is theoretically located exactly half way between two perfectly symmetrical electrodes. Slight defects in electrode shape or differences in surface impedance will shift the zero. This occurs because electrodes are electrically wire in series, which is equivalent to two capacitors in series. When the capacitors are different sizes, a difference in potential drop is observed at each electrode interface, which shifts the zero location. The zero location also shifts when the electrode separation is changed. This occurs for symmetrical and asymmetrical electrodes to a varying degree. With respect to the cell position, the zero will always move towards the mobile electrode as the mobile electrode is moved away from the cell. Therefore, if the zero location is located behind the working electrode (fixed at the cell), the zero potential line may pass through the cell if the electrodes are sufficiently separated. If this occurs, then the peak-to-peak change in cell membrane potential will appear to decrease with electrode separation (as the zero line approaches the cell) and then increase (as the zero line passes over and away from the cell). The probability of this occurring with sharp, bare gold electrodes is low because of the large potential drop at the gold tips. The small surface area and low surface impedance at the tip of the sharp gold electrodes consequently exposes the cell to a very small potential range ($\sim$12 mV). The likelihood of the zero potential existing between this small range is low. The lower surface impedance of PEDOT:PSS compared

to gold, however, increases the probability that the zero potential line exists between the electrode tips. Furthermore, the location of the zero potential line changes with time during stimulation pulses. The potential drop across the electrode/electrolyte interface increases with time for an applied electrochemical potential step. Ionic currents charge the electric double layer capacitor and faradaic currents create a depletion layer of ionic species around the electrode. However, if the electrodes are asymmetrical, the increase in potential drop at each interface will be unequal over time, which causes the zero potential line to shift and broaden.

PEDOT:PSS wires were fabricated at the end of SAM-coated electrodes. Three different wires were used to test the effects of wire length and diameter: 2.5 x 42 μm (nominal wire), 2.4 x 89 μm (long wire), and 1.4 x 49 μm (thin wire). A bare gold electrode was used as the counter electrode for all PEDOT:PSS wire cell stimulation experiments. Raw potential measurements are shown for the sealed, patched, and broken states for the nominal wire, long wire, thin wire, bare gold, and SAM-coated gold in Figure 4.21. Interestingly, the amplitude of the change in membrane potential in response to an applied stimulus from wires was relatively large, but the amplitude hardly changed when electrode separation was increased. A similar behavior was observed for the SAM-coated gold electrodes, which is expected since the electrode with the attached wire is SAM-coated. The change in potential due to the long wire was significantly higher than that of SAM-coated or bare gold alone. The change in membrane potential increased with length and diameter. A decrease in membrane potential change would be expected for a smaller diameter because of the smaller surface area and higher series resistance at the wire tip. However, the increased change in membrane potential due to the longer wire is counterintuitive due to the increased series resistance at the polymer wire tip. This result nonetheless agreed with the COMSOL model, which showed a large field around the wire. A longer, uninsulated wire has more overall surface area, which will lower the total impedance at the electrode. In other words, fields generated along the wire length contribute to the potential field at the

tip. Diminishing returns would be expected as the length of a wire increases. The increased series resistance due to the wire length would eventually be greater than the decreased surface impedance due to additional surface area added farther away from the tip. However, the potential field at the wire tip would always decrease with increased length if the wire were insulated.

The experimental conditions for each pair of electrodes and cells were simulated in a COMSOL model. The same overall geometry used for nonuniform field mapping was used for consistency (Figure 4.5). The model was used to predict how the cell membrane potential response from an applied field changed with electrode separation. Model and experimental results were compared by normalizing potential measurements obtained at 25 μm for each trial. All curves were found to be monotonic, so any potential curves that decreased with separation were inverted for comparison purposes. The model used average surface potential experienced at the cell membrane. Change in cell potential was calculated by integrating the potential over the surface of a half-ellipsoid with a height of 5 μm and a length/width approximated from brightfield microscope images. Gold electrodes, polymer stubs, and polymer wires were modeled using the same geometries as those used for nonuniform field potential measurements. Simulations were computed for gold and PEDOT:PSS surface impedance values found from uniform potential mapping as well as values obtained after adjustment from nonuniform field mapping. Experimental and simulated results for a pair of 4 μm PEDOT:PSS stubs are plotted in Figure 4.23. Interestingly, the model with surface impedance values from uniform potential measurements more closely matched experimental results for HEK cell stimulation. The adjusted model clearly overestimated the change in membrane potential for one of the stub configurations, which, for that particular pair of stubs, had a sizeable surface impedance adjustment. Smaller diameter stubs exhibited the opposite error. Simulation results for stubs with a diameter of 2 μm agreed well with experimental results following surface impedance adjustments. Nonuniform potential field measurements indicated that PEDOT:PSS features with diameters less

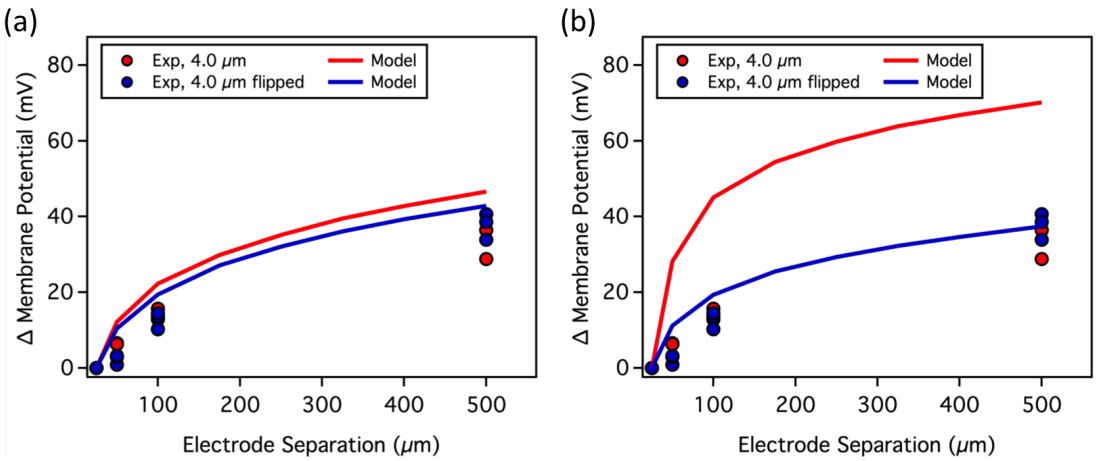


**Figure 4.23:** Change in HEK cell membrane potential due to stimulus from a pair of 4.0 μm PEDOT:PSS stubs. Results are shown for HEK cells stimulated with each stub. Predicted results from the COMSOL model are shown for (a) original PEDOT:PSS surface impedance values (from uniform field measurements) and (b) adjusted values (from nonuniform field measurements).

than 2 μm generated a significantly lower field than predicted by the model. Potential fields larger than predicted by the model were obtained for PEDOT:PSS stub diameters greater than 2 μm. Therefore, the effects of the polymer stub diameter were consistent at least in general behavior. These results do assume that the solution conductivity is accurate and constant. An underestimation in solution conductivity would result in an overestimation of change in potential amplitude with electrode separation. The results are likely less accurate for smaller polymer structures due to the spatial and temporal-average surface impedance assumption that was used in estimating the surface impedance from uniform potential measurements.

### 4.3.7 Time-dependent model studies

A COMSOL model was modified to elucidate time-dependent phenomenon that may have led to the observed results related to differences in surface impedance as a function of polymer stub or wire diameter. One potential error in the pipette potential mapping method could have been due to the zero potential location. Near this location, two overlapping sine waves were observed, which were presumably a superposition of ionic current due to each electrode at opposite polarity. Due to the inevitable difference in capacitance between any two electrodes (e.g. surface defects, geometry, etc.), their respective sinusoidal currents

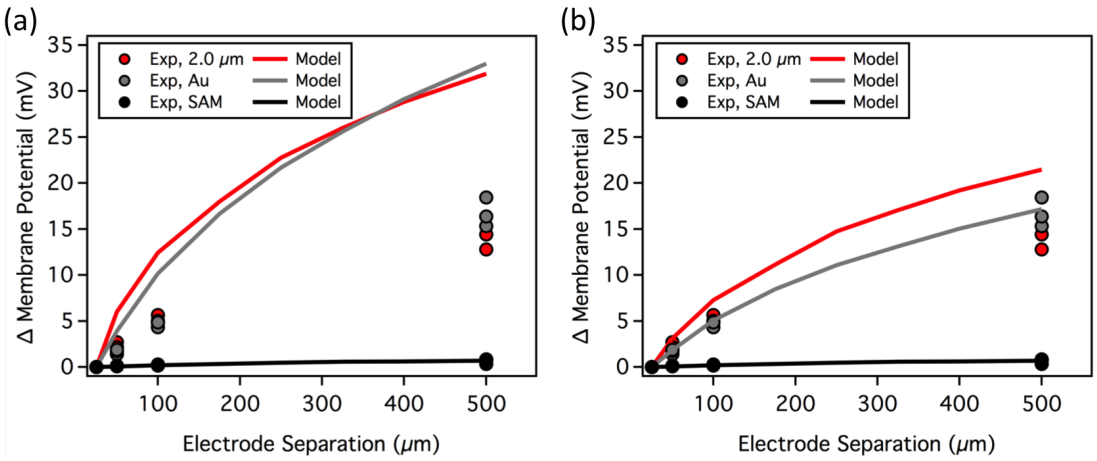


**Figure 4.24:** Change in HEK cell membrane potential due to stimulus from a pair of 2.0 µm PEDOT:PSS stubs. Results are compared to gold and SAM-coated gold. Predicted results from the COMSOL model are shown for (a) original surface impedance values (from uniform field measurements) and (b) adjusted values (from nonuniform field measurements).

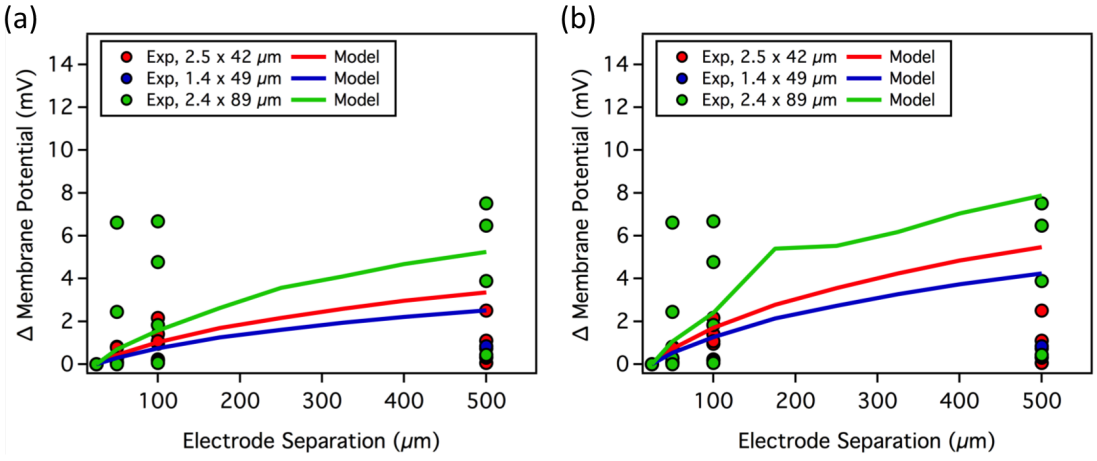


**Figure 4.25:** Change in HEK cell membrane potential due to stimulus from PEDOT:PSS wires and a bare gold counter electrode. Predicted results from the COMSOL model are shown for (a) original surface impedance values (from uniform field measurements) and (b) adjusted values (from nonuniform field measurements).

were never perfectly out of phase as might be theoretically expected. The pipette also has a finite tip diameter as well as an Ag/AgCl electrode that may have different potential time constants for difference ionic species. A well-defined zero potential line was consequently not observed and likely resulted in peak-to-peak potential measurement error in these areas. Time-dependent model studies were used to investigate the temporal evolution of a $\pm$ 2.5 mV band during sinusoidal voltage excitation.

A contact impedance boundary condition was applied to the modeled PEDOT:PSS surface. COMSOL models contact impedance using a capacitor in parallel with a resistor. Capacitance was also estimated from previous results obtained from current transients of PEDOT:PSS wires with diameters near 4 μm. A specific capacitance value of 35 F $m^{-2}$ was used for PEDOT:PSS is on the order of previously published values [213] along with a charge transfer resistance of 1 x $10^{-3}$ $m^2$. The contact impedance boundary did not account for pore resistance. Therefore, a 50 nm shell was added to the PEDOT:PSS surface with a capacitance of zero and a specific resistance value of 1 x $10^{-6}$ $\Omega$ $m^2$, which was found to match RC time constants obtained from current transients. previous gold current yielded an estimated specific capacitance of 0.5 F $m^2$.

The results from time-dependent models are shown in Figure 4.26. One important observation is that the zero equipotential line shifts with time towards one of the electrodes. This explains why one of the electrodes exhibited a larger potential than the counter electrode. This model shows that time dependence must be considered when predicting the field generated by small polymer geometries.

## 4.4 Conclusions

The current work investigated the use of small scale PEDOT:PSS stubs and microwires for generating localized potential fields. A pipette electrode was used to map uniform field potentials generated by PEDOT:PSS, bare gold, and SAM-coated gold. A model was used to extrapolate surface impedance boundary conditions and were compared to

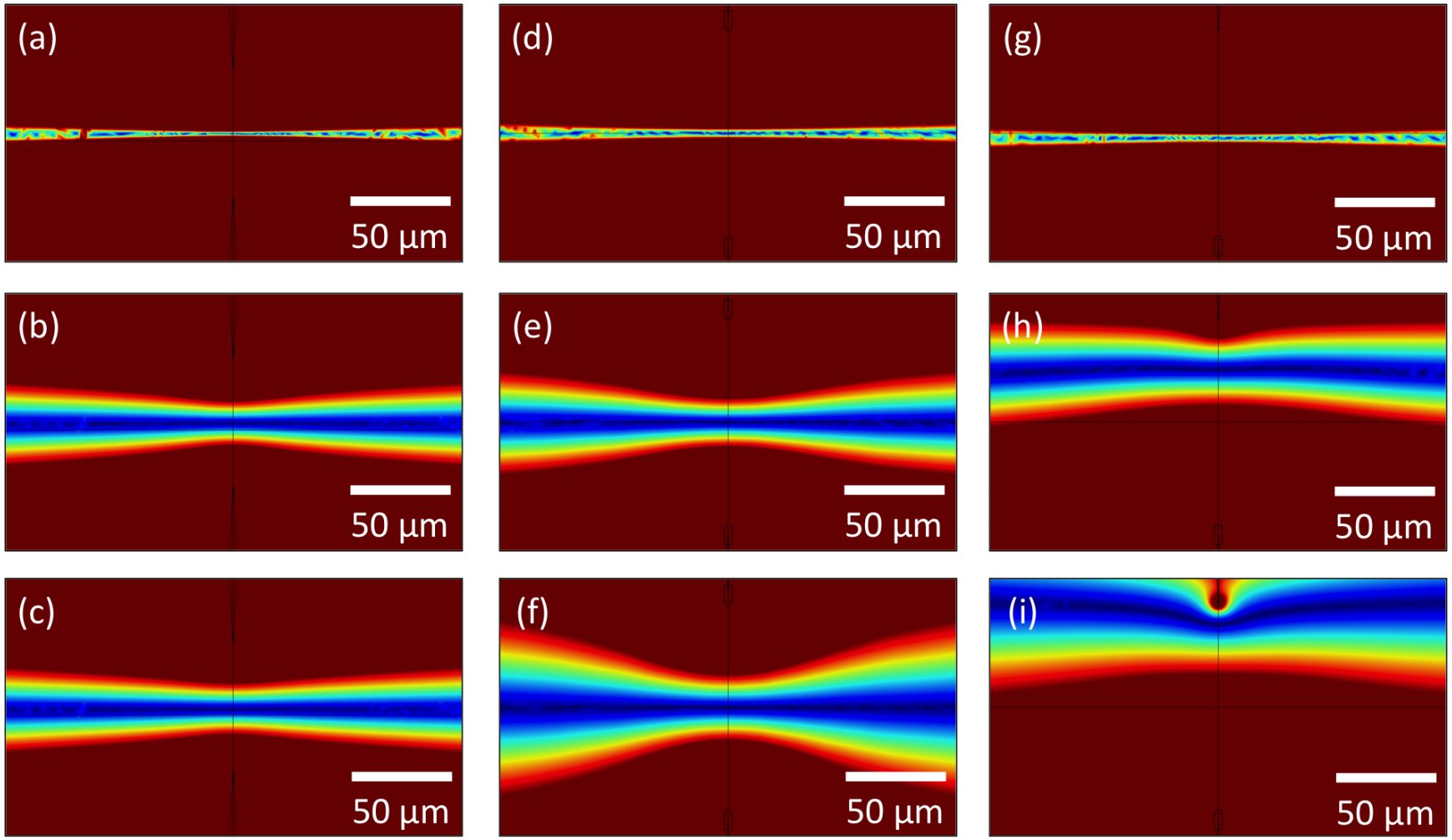


**Figure 4.26:** Time-dependent COMSOL model showing the evolution of a ± 2.5 mV band in response to a 1 V voltage step for (a-c) symmetrical 1.25 µm PEDOT:PSS stubs, (d-f) symmetrical 4 µm PEDOT:PSS stubs, and (g-i) asymmetrical arrangement with 1.25 µm (top) and 4 µm (bottom) PEDOT:PSS stubs. The time range is from 0 (top), 100 µs (middle), and 200 µs (bottom).

results obtained from conventional EIS. Small, PEDOT:PSS stubs at the end of sharp gold electrodes were subsequently mapped with a pipette electrode and compared to the model. Finally, membrane potential changes of HEK cells were directly measured using patch clamping in response to nonuniform potential fields delivered by polymer stubs and wires. Results were compared to those predicted by the model of potential fields for different cell geometries and locations.

It was found that absolute potential was difficult to model due to the slight variations in geometry and surface impedance that induce significant changes in potential offsets. However, potential offsets should not significantly change the accuracy of modeled electric fields. Electric field values were underestimated by the model with input surface impedance values from uniform field measurements. These discrepancies could be due to the difficulty in using a spatial and temporal-averaged surface impedance to model a porous material for small geometries. Impedance normalized to a volumetric shell may be more representative and accurate for smaller geometries. Polymer stubs and wires with diameters below 2 μm exhibited surface impedance values similar to gold. These errors became significant with small absolute capacitance values of the small geometries that cannot be accurately modeled using time-averaged surface impedance. Changes in HEK cell membrane potential in response to voltage stimulus followed the average potential field predicted by the model. Changes in membrane potential increased as electrodes were separated at a greater distance due to the larger potential drop across the solution relative to the potential drop at each electrode surface. The zero potential line was found to be important since it is dynamic with time. Time-dependent studies find that smaller stub and wire geometries created a field that decays more rapidly and causes the zero equipotential line to grow in size and move in space. These findings reveal that polymer electrode geometries below $\sim$200 $\mu m^3$ are not modeled well using a spatial and temporal-averaged surface impedance. A time-dependent model would yield more accurate results due to the drastic changes in field over a short time scale for small capacitance microstructures.

# CHAPTER 5
# CONCLUSIONS AND FUTURE WORK

## 5.1 Major Contributions

This work was based on the synthesis of PEDOT:PSS nanowires first developed by Flanders et. al. at Kansas State University [156–160]. The potential advantage of conductive polymer wires is the combination of their electrical conductivity and relative low mechanical modulus. Yet, the application of these wires as an electroactive biomaterial was not explored before this research. This work investigated the use of polymer wires as single cell stimulation electrodes. Overall, the outcomes of this research have advanced our knowledge and techniques related to single cell polymer wire microelectrode development, electrically conductive biomaterials, and subcellular electric field modeling. The major contributions are summarized:

- **Method for visualizing localized electric fields of PEDOT:PSS nanowires** Fluorescently labeled proteins were used to track potential fields generated by polymer nanowires. A method using tagged proteins and fluorescence microscopy was developed to determine the spatial range of generated field potentials without the need for direct electrochemical coupling.

- **PEDOT:PSS microwire synthesis:** Nanowires were not able to elicit action potentials in cardiomyocytes due to excessive series resistance and low surface area of nanoscale wires. Microwires were synthesized by using a lower range of frequencies during AC voltage synthesis. Large diameter PEDOT:PSS wires grown with this method have not previous been performed. It was found that lower frequencies did yield larger diameter wires, but diameter control was not as precise. Additionally, nonspecific electropolymerization occurred higher up on the gold electrode whereas

high frequency synthesis localized polymer only at the tip.

- **Electrochemical characterization of PEDOT:PSS micro and nanowires:** PEDOT:PSS polymers have been well-characterized as electrical biomaterials in terms of their charge storage density and impedance. However, polymer wires had not been applied for single cell electric stimulation and thus, had not been electrochemically characterized. A method was developed to probe the charge storage density of polymer wires by using a drop of electrolyte on a hydrophobic slide. This method allows for charge storage density measurements of isolated microstructures down to 1 $\mu m^2$ while keeping the rest of the electrode perfectly insulated in air.

- **Evaluation of PEDOT:PSS microwire single cell stimulation:** Micro and nanowires composed entirely of conductive polymers introduces an interesting tradeoff between electrical conductivity, surface impedance, and mechanical flexibility. Cardiomyocytes were used as model cells to determine the minimum feature size of PEDOT:PSS polymer wires that could be used to electrically stimulate single cells. The smallest wire capable of stimulation was 27 μm long with a diameter of 2 μm. This work was the first to determine these limits and concluded that electrical conductivity restricts polymer wire dimensions capable of single cell stimulation to a mechanically rigid range.

- **Enhanced conductivity of PEDOT:PSS micro and nanowires:** Conductivity was found to prohibit the ability for smaller, flexible wires to stimulate single cells. A method to increase conductivity of the polymer wires was developed. First, it was found that post chemical treatments of polymer wires were ineffective in conductivity enhancement. This is an interesting finding since chemical post treatments are well-known to enhance the conductivity of spin cast films several orders of magnitude. The work presented here determined that synthesis conditions are the key to controlling downstream electrical conductivity of polymer wires. It was found that

higher concentrations of monomer and lower molecular weight of the counter ion polymer PSS yielded conductivities several fold higher. However, the wires with this enhanced conductivity were noticeably more mechanically rigid.

- **In situ monitoring of surface impedance during polymer film deposition:** The principal advantage of conductive polymers like PEDOT:PSS are their low surface impedances, which makes them attractive as films. Their relatively low electrical conductivity compared to noble metals, however, means higher series resistance for excessively thick films. A simple method for *in situ* monitoring of surface impedance during PEDOT:PSS film deposition was developed and was found to correlate very well with resulting surface impedance values.

- **Local field potentials for measuring surface impedance and electric fields at microelectrode tips:** Surface impedance is important for characterizing and modeling the effectiveness of bioelectrodes for in vivo applications. Microelectrodes with high surface impedance values require higher voltages for cellular stimulation that have been shown to degrade electrodes faster and damage tissue. Surface impedance has been measured for PEDOT:PSS films extensively but has not been measured using local field potentials in uniform fields or in nonuniform fields generated by small polymer microsctructures. This method provides a direct way of measuring the electric field generated by microelectrodes in an electrolyte solution.

- **Surface impedance scaling:** Electrical impedance spectroscopy is often used to characterize the electrochemical efficiency of an electrode used for stimulation. The electrodes that are tested often have a large, flat surface area, but the geometric dimensional limit at which surface impedance values measured in this way are valid has not been explored. This work determined that using a spatial and temporal average of surface impedance for a 1 kHz sine wave begins to introduce significant error for polymer structures below 2 μm in diameter.

- **Modeling surface impedance for subcellular microprobes:** A model was developed that is capable of predicting the shape and magnitude of microelectrode wires. The model was specifically made for polymer wires, but can be adjusted for any material given the necessary input parameters, notably surface impedance and electrical conductivity. The process of obtaining this input parameters and adjusting the model for accuracy was developed in this work.

- **Single cell stimulation with membrane potential feedback from patch clamping:** A method was developed to measured membrane potential of a cell while in the presence of a nonuniform electric field generated by microelectrodes in bipolar and monopolar configurations. This method also compensates for glass pipette parasitic capacitance.

- **Time-dependent model electric field evolution from microelectrodes:** A time-dependent model was built to investigate the effective potential field generated by polymer microstructures too small to be characterized under the assumption of a spatiotemporally averaged surface impedance. This model elucidates important phenomenon such as the translation of the zero potential line and transient, nonuniform potential field generation.

## 5.2 Future Work

It is unlikely that extracellular electrode arrays made of polymer wires will ever been able to selectively interact with all 86 billion neurons in the brain. Implanted electrodes are too invasive and introduce too many physical interfaces between nonbiological and biological materials. The mechanical benefits of using wires made entirely out of conductive polymers do not outweigh their poor electrical conductivity. Wires would need to be longer than a few cell lengths and be less than 5 μm in diameter for them to be useful. However, a simple composite wire could increase conductivity greatly and may improve the physical

connections between electrodes and cells. The fundamental problem of flexible wires and electrodes is still the inability to control their placement *in vivo* and choose which cells they interact with. Significant advancements need to be achieved before the potential benefits of these polymer wires can be realized for neural applications.

The primary challenge in engineering extracellular stimulation electrodes for deep brain stimulation is the interaction between the electrode and brain tissue. Implantation is a major hurdle; tissue damage during implantation is often the source of long-term biocompatibility issues. Flexible electrodes actually make implantation more difficult since they are not stiff enough to penetrate brain tissue. Injectable electronics have largely avoided implantation damage and demonstrated that flexible electrode arrays can maintain excellent chronic stability *in vivo*. However, this injection method sacrifices the control of positioning electrodes near specific target neurons. Recent research has also shown that a shuttle can be used to position wires as small as those used in the research presented here. Tissue damage from the shuttle during implantation was shown to be fully recoverable in the brain and enabled long-term stability of the implanted flexible electrode. These latest developments definitely show promise for improving current DBS electrode devices. Future DBS electrodes will likely decrease in size and maintain effective therapeutic stimulation while minimizing side effects from extraneously neuron stimulation. The ultimate goal for flexible DBS electrodes will ultimately be to improve chronic stability and cell selectivity. Full resolution brain mapping and control is likely more feasible using wireless techniques (e.g. temporal interference [23]) since they have much lower physical constraints and do not suffer from the substantial biomaterials challenges. Wireless techniques are still very far from achieving single cell resolution with tens of billions of neurons simultaneously.

### 5.2.1 PEDOT:PSS wires

This represented the first work in evaluating these specific PEDOT:PSS polymer wires for bioelectrical applications. The low surface impedance of PEDOT:PSS makes it an ideal

interface for both generating ionic field gradients as well as measuring them. This two-way transducer capability is only inherent in pseudocapacitive materials such as PEDOT:PSS and Iridium Oxide. Gold, for example, can really only be used for stimulation if a high enough voltage is used to elicit faradaic electrochemical reactions. Recording with materials such as gold, would need to have an extremely intimate connection to the the cell with a relatively large surface area, such as the microelectrode array composed of gold micro-mushrooms [215], which only works due to the insulating properties of the substrate the cells are grown on. PEDOT:PSS wires for recording cell signals would be an interesting study, but, again, would suffer from their low conductivity. Although, the studies conducted so far have been carried out at room temperature. Physiological temperature might make smaller wires capable of stimulation due to enhanced conductivity and currents experienced at higher temperatures [216].

Three dimensional PEDOT:PSS structures at the cell interface might be a more useful investigation since PEDOT:PSS has rarely been studied beyond a film morphology. An example might be PEDOT:PSS stubs on a substrate or an array of nanowires tethered to a cell. Results would be useful for future electrode developments that might employ three-dimensional structures at the tip of a wire composed of a different material. One major area for improvement is a model based on volumetric capacitance. PEDOT:PSS is a porous material and cannot be modeled as having two-dimensional surface impedance for small structures. More work needs to be performed on mapping different sized polymer geometries and determining the limit at which 2D surface impedance assumptions break down.

PEDOT:PSS, in general, has not been investigated enough at the nanoscale for engineering optimization. For example, the mechanism by which PEDOT:PSS can safely generate highly localized electric fields is a complex process [132–134]. It is generally accepted that the interaction between PEDOT and its counter-ionic polymer PSS is responsible for the pseudocapacitive behavior that yields high charge density. However, there have not been extensive studies on optimizing the PEDOT counterion in light of the fundamentals

of the charge transfer mechanism. Glimpses of the potential in this area are seen with the PEDOT:PSS wires with enhanced conductivity using different molecular weight PSS polymers for the counter ion. There might be an optimum counterion molecular weight or synthesis conditions that promote a preferential conformation at the PEDOT and PSS interface. These types of studies could leverage the mechanism of charge injection of PEDOT:PSS and fully exploit its capabilities for even lower surface impedance.

### 5.2.2 Neuron stimulation

Single PEDOT:PSS wires may not be useful, but PEDOT:PSS nanowire arrays may still have a promising future for stimulating electrically active cells such as cardiomyocytes or neurons. These types of cells are stimulated from local electric field gradients and do not require fully induced cell depolarization to elicit an action potential. As a polymer wire is scaled down, mechanical flexibility increases but at the cost of higher electric resistance. However, if several wires are attached to a cell membrane locations with a high density of ion channels, it may be possible to elicit an action potential. PEDOT:PSS nanowires will never be able to stimulate cells unless they are in direct contact with the cell membrane. PEDOT:PSS wires in this work have been used to stimulate single cardiomyocytes with binary feedback (cell contraction) and HEK cells with analog feedback (patch clamping). The next step would be to stimulate an electrically active cell with analog feedback from patch clamping. The response to a potential field is drastically different between HEK cells and electrically excitable cells due to the presence of voltage-gated ion channels. These channels are activated from local electric field gradients, which then begin to depolarize the cell. These studies can then be used to solidify the accuracy of the COMSOL model by relating polymer wire dimensions, distance from cell, voltages, and currents to minimum cell stimulation requirements. A robust model calibrated from experiments can then be used to predict the performance of new, smaller wire designs such as composite nanowires.

### 5.2.3 Composite wires

Composite wires are notable since it was found that the polymer conductivity is not sufficient for long thin nanostructures to be successful for mechanically flexible bioelectrical interfaces. Materials with higher conductivity might be combined with PEDOT:PSS to take advantage of the properties of both materials. Initial work was performed by assembling gold nanoparticles into a flexible chain that demonstrated higher conductivity and lower apparent Young's modulus than PEDOT:PSS. This type of wire might serve as the perfect electronic pathway complemented with a PEDOT:PSS tip to facilitate efficient electronic/ionic transduction at a target location. The following was presented at the 2018 Society for Biomaterials Conference in Atlanta, GA.

Single neuron electrodes are needed to better understand and treat abnormalities in the brain. Patch clamping and microelectrode arrays are mechanically rigid, which can adversely affect cell health. A sufficiently small and flexible bioelectrode is needed that can accommodate tissue dynamics while maintaining electrical connection to a target cell. Nanowires offer the promise of providing subcellular spatial resolution with low bending modulus to better match the mechanical properties of tissue. Previous work has shown that as conductive polymer wires are scaled down to flexible dimensions, they are not able to stimulate cells due to their low electrical conductivity [150]. Here, we use dielectrophoresis to assemble gold nanoparticles (AuNPs) into nanowires that are 14x less rigid and 1000x more conductive than polymer wires composed of poly(3,4-ethylenedioxythiopene):polystyrene sulfonate (PEDOT:PSS). Thus, AuNP wires offer a potentially more stable, long-term electrical connection to single cells in soft tissue environments.

An inverted microscope retrofitted with two 3-axis micromanipulators was used to image and manipulate electrodes and wires. PEDOT:PSS and AuNP wires were synthesized by applying an oscillating voltage between two sharp gold electrodes in solution [158, 217]. PEDOT:PSS wires were grown using a square wave voltage (2 – 3 kHz, $\pm$ 2.0 – 7.2 Vpp) in an aqueous solution containing 10 mM EDOT and 20 mM PSS. Dielectrophoresis was

used to assemble 30 nm AuNPs using a square wave voltage (0.05 – 1 MHz, ± 1.6 – 2 Vpp) and a DC offset (+1.4 V). Conductivity was calculated from current-voltage curves obtained from two point probe measurements. Scanning electron microscopy (SEM) confirmed the diameter of single-width AuNP chains. Apparent Young's Modulus of the wires was estimated by finding the resonant frequency of vibration in air. Wires were oscillated electrostatically by applying a sinusoidal voltage with a gold counter electrode. Resonant frequency peaks were found from video analysis by plotting the vibration amplitude as a function of frequency. Brightfield microscopy images were used to measure wire lengths and diameters; the full-width-half-maximum of line intensity profiles was used for the latter. Each wire was modeled in COMSOL as 5 μm cylindrical segments. The diameter of each wire segment was averaged. The Young's modulus was determined by the value in which the resonant frequency of the model matched the experimental value within 1 %.

Electrical conductivity (Figure 5.1) was found to be 38 ± 14 S $cm^{-1}$ for PEDOT:PSS wires with an average wire diameter of 1.5 ± 0.1 μm (n = 9) and 150,007 ± 6259 S $cm^{-1}$ (n=4) for 30 nm AuNP wires. Effective Young's modulus was found to be 527 ± 116 MPa for PEDOT:PSS wires (n = 3) and 39 ± 21 MPa for AuNP wires (n = 4), respectively (Figure 5.2). PEDOT:PSS wires for vibration experiments had an average diameter of 1.6 ± 0.1 μm and lengths between 76 – 106 μm. AuNP wire diameters and lengths were between 1 – 3 μm and 19 – 60 μm, respectively. Images of AuNP wires in brightfield and SEM images is shown in Figure 5.3.

Developing biomaterial interfaces that are both electrically conductive and mechanically flexible is difficult to achieve since these properties are typically anticorrelated. AuNP wires were found to have a higher mechanical compliance and more than three orders of magnitude higher electrical conductivity compared to PEDOT:PSS polymer wires. The combination of high conductivity and mechanical flexibility makes AuNP wires promising for stable, long-term electrical connections to single cells in soft tissue environments.

In general, testing new wire designs by varying shape, material, or synthesis conditions

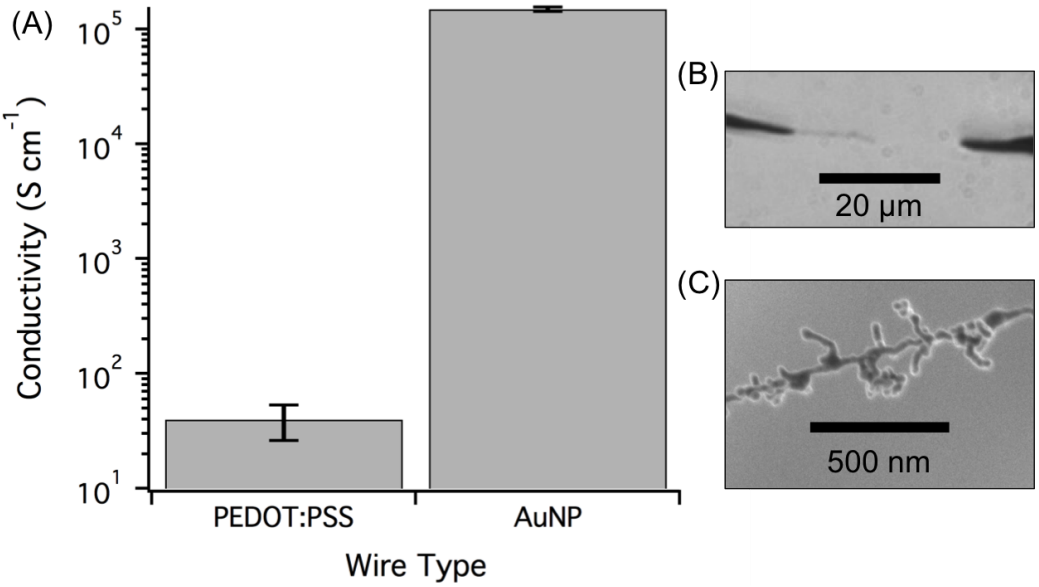


**Figure 5.1:** (A) Conductivity of PEDOT:PSS and AuNP wires. (B) Brightfield and (C) SEM image of 30 nm AuNP wire.

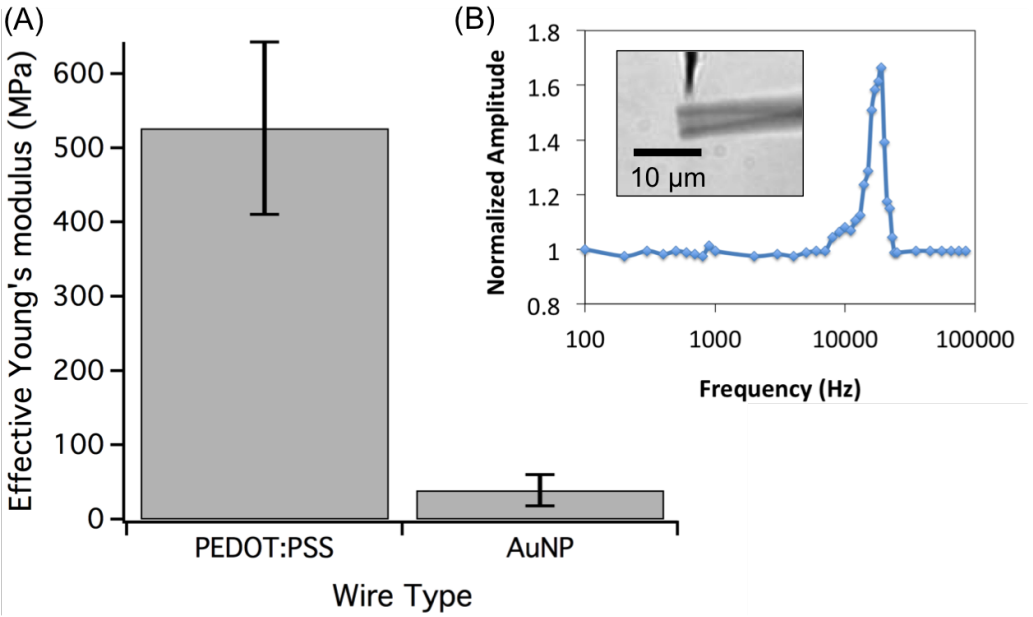


**Figure 5.2:** (A) Young's modulus values for PEDOT:PSS and AuNP wires. (B) Representative amplitude plot and inset image of a PEDOT:PSS wire oscillated at resonance.

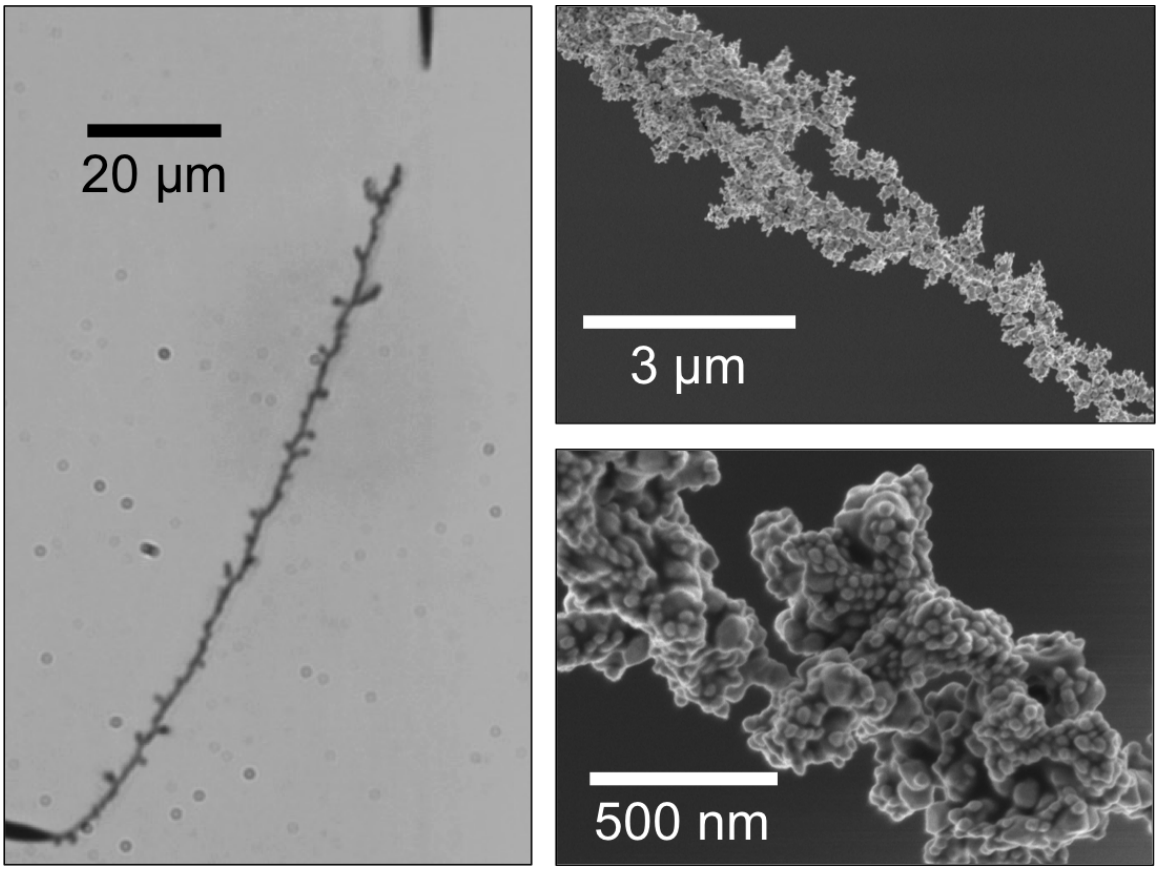


**Figure 5.3:** Brightfield microscope image (left) and scanning electron micrographs (right) of a AuNP wire assembled from 30 nm gold nanoparticles.

can be quickly evaluated with two measurements: conductivity and surface impedance. Conductivity should be measured using a two-point probe technique at several locations along the wire to account for contact resistance. Surface impedance can quickly be measured using uniform and non-uniform field mapping with a glass pipette electrode. These two parameters will dictate what kind of fields can be generated for a given wire. Once these parameters are determined, they can be used in a simple COMSOL model to incorporate the effects of wire shape on the resulting electric field. This simple model can quickly compare the performance of flexible wire electrodes. Actual performance needs to still be incorporated into the model and is a potential top for future work.

### 5.2.4 Modeling electrode stimulation

The COMSOL model that was developed for this work is powerful for predicting electric field generation of polymer microstructures as well as potentially new, composite materials. One limitations of the model that will always exist is the geometric accuracy. Nonuniform surface roughness and geometric defects are nearly impossible to accurately model. Error due to geometry becomes especially non-negligible when polymer stub diameters fall below 2 μm. Surface area-to-volume ratios at small scales make the spatially-averaged surface impedance assumption invalid and would need to take polymer volume into account. The low total capacitance at for small scale electrodes means that potential fields change drastically in space and rapidly in time. A time-dependent model is necessary in these regimes to average the spatiotemporal changes exhibited by the small electrodes. An initial time-dependent model was developed here but still needs significant improvement. An investigation on how the average surface capacitance of PEDOT:PSS wires and stubs changes with volume is needed. PEDOT:PSS is a porous matrix that cannot be accurately modeled with average surface properties at small scales. There is likely a maximum film depth within PEDOT:PSS that can freely exchange ions in and out of electrolyte solution within a certain time ($\sim$500 μs for a 1 kHz wave). A time constant and specific capacitance

needs to be determined for wires of various diameter using current transients. An equation should then be developed that relates that specific capacitance and charge transfer resistance to the dimensions of the polymer structure to be modeled. Once these parameters are incorporated into the model, polymer electrodes with diameters below 2 μm can be accurately modeled. Note that 1 ms is considered the upper limit for stimulation pulses. Shorter pulses are preferred because they minimize irreversible faradaic reactions that occur more rapidly after charging the double layer capacitance. Shorted pulses are more difficult to measure directly using local field potentials from a pipette because of the limitations of measuring fast potential transients with inherent parasitic capacitance.

## 5.3 Final thoughts

Information and control of cells in the brain have either been conducted at one of two extremes: 1.) Single cell, high selectivity, and low throughput or 2.) one or multiple cells, low selectivity, and high throughput. This is the case for all types of current techniques, both invasive and noninvasive. There is no method to control or probe a large population of individually-targeted cells from several or all parts of the brain. A method to facilitate high throughput connections to individual cells in the brain is a significant engineering challenge. The fundamental issue is, really, the vast number of hurdles stacked up that need to be cleared simultaneously. The ultimate method must be biocompatible, use low voltage/current, have mechanical flexibility, be capable of local cell selectivity, have high conductivity, have low surface impedance, be biochemically stable, interface to electronics, be powered, be implantable, be safe, and meet ethical requirements. Most of these challenges originate from the hostile nature of the biological environment. A feasible comprehensive solution is difficult to imagine without large scale genetic engineering, which obviously approaches the limits of current ethical paradigms. The long-term approach might be a significant advancement in portable, noninvasive electric field generation from the outside of the body. Ed Boyden's group at MIT has recently published work that employs con-

structive and destructive electric field interference [23], which has potential advantages similar to what two photon illumination has brought to fluorescence microscopy. However, the resolution and throughput of this method is still far from connecting to every cell in the brain simultaneously in a lab setting. But, even single connections to a relatively small group of cells in a region of the brain would still provide significant insight into the role of individual cells and neuronal circuits. Deep brain stimulation and recording with microelectrode arrays have already demonstrated success with basic materials. Work on bioelectrical materials that are small and flexible do show promise but still face significant challenges in implementation and reliability beyond the lab setting. Conductive polymer films, particularly PEDOT:PSS, are imperative for the next generation microelectrode and will not go away. Their combination of low surface impedance and biocompatibility has, so far, been unmatched.

# Appendices

# APPENDIX A

# POLYMER WIRE DIAMETER IMAGE PROCESSING

Image processing in Matlab was used to calculate PEDOT:PSS nanowire diameter. (a) The SEM image of the PEDOT:PSS nanowire shown in Figure A.1(a) was first rotated, cropped, and converted to a binary image. (b) The outlined nanowire profile (black), slope of nanowire profile (blue), and calculated wire diameter (red) are plotted as a function of x-position along the wire segment. The slope of the nanowire profile was calculated using a least squares linear regression. The slope line indicates the orientation of the nanowire in the image. The raw image was rotated until the slope was near zero to ensure accurate diameter measurements. The diameter was then calculated by subtracting the upper and lower boundary positions of the wire profile. The diameter for an individual wire was found from the average of all measured diameter points. The average diameter for each synthesis frequency was determined to be 0.76 $\pm$ 0.22 and 1.50 $\pm$ 0.55 μm for 10 and 2 kHz wires, respectively. Surface roughness of the wires affects the electrochemical surface area in contact with the electrolyte solution. Average surface roughness, $R_a$, was calculated using Equation A.1 and was determined to be 17.6 $\pm$ 8.3 and 23.4 $\pm$ 7.8 μm for 10 and 2 kHz wires, respectively. Surface roughness did not vary significantly between these wire diameter (p-value = 0.35). Diameter and surface roughness results were determined for n = 4 wires at each frequency.

$$R_a = \frac{1}{N} = \sum_{n=1}^{N} |r(x)| \tag{A.1}$$

where $N$ is the number of points along the profile and $r(x)$ is the height of the boundary measured from the mean y-position of the profile.

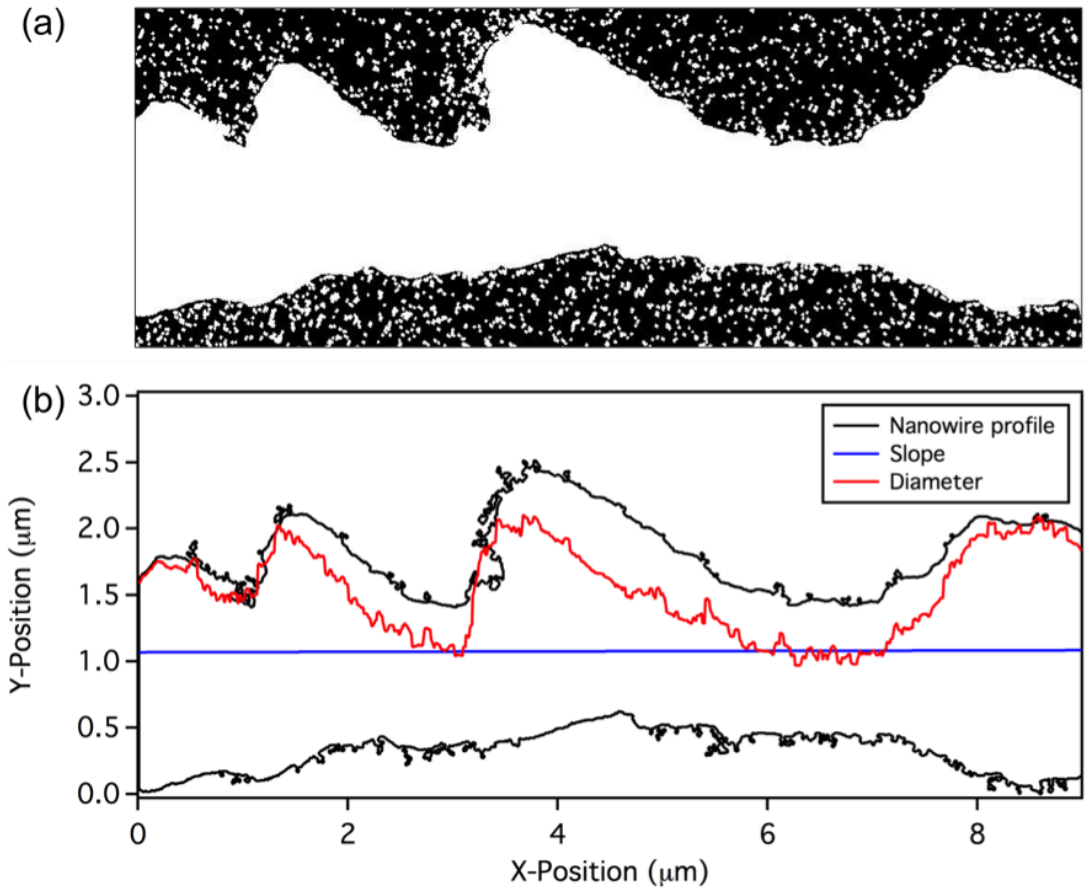


**Figure A.1:** Representative MATLAB image processing results used to calculate PEDOT:PSS nanowire diameter where (a) is the binary converted image from SEM and (b) is the plotted profile obtained from Matlab.

## REFERENCES


[1] Frederico A.C. Azevedo et al. “Equal numbers of neuronal and nonneuronal cells make the human brain an isometrically scaled-up primate brain”. In: *Journal of Comparative Neurology* 513.5 (2009), pp. 532–541.

[2] Steven M Wellman et al. “A Materials Roadmap to Function Neural Interface Design”. In: *Advanced Functional Materials* in press (2017), p. 1701269.

[3] B Alberts et al. *Molecular Biology of the Cell*. Vol. 54. 2008, p. 1725. ISBN: 0815341067.

[4] Benjamin D Almquist and Nicholas A Melosh. “Fusion of biomimetic stealth probes into lipid bilayer cores.” In: *Proceedings of the National Academy of Sciences of the United States of America* 107.13 (2010), pp. 5815–5820.

[5] B. Tian et al. “Three-Dimensional, Flexible Nanoscale Field-Effect Transistors as Localized Bioprobes”. In: *Science* 329.5993 (2010), pp. 830–834.

[6] Frank Rattay. “Analysis of Models for External Stimulation of Axons”. In: *IEEE Transactions on Biomedical Engineering* BME-33.10 (1986), pp. 974–977.

[7] F Rattay. “Analysis of models for extracellular ber stimulation”. In: *Ieee* 36.7 (1989), pp. 676–682.

[8] A. L. Hodgkin and A. F. Huxley. “A quantitative description of membrane current and its application to conduction and excitation in nerve”. In: *Bulletin of Mathematical Biology* 52.1-2 (1990), pp. 25–71. arXiv: NIHMS150003.

[9] Boshuo Wang et al. “Modified cable equation incorporating transverse polarization of neuronal membranes for accurate coupling of electric fields”. In: *Journal of Neural Engineering* 15.2 (2018).

[10] Claude Bédard and Alain Destexhe. “A modified cable formalism for modeling neuronal membranes at high frequencies”. In: *Biophysical Journal* 94.4 (2008), pp. 1133–1143. arXiv: 0705.3759.

[11] Claude Bédard and Alain Destexhe. “Generalized cable theory for neurons in complex and heterogeneous media”. In: *Physical Review E - Statistical, Nonlinear, and Soft Matter Physics* 88.2 (2013). arXiv: 1304.5674.

[12] Student Member. “A New 3-D Finite-Element Model Based on Thin-Film Approximation for Microelectrode Array Recording of Extracellular Action Potential”. In: 55.2 (2008), pp. 683–692.

[13] Sébastien Joucla and Blaise Yvert. “The ”mirror” estimate: An intuitive predictor of membrane polarization during extracellular stimulation”. In: *Biophysical Journal* 96.9 (2009), pp. 3495–3508.

[14] Sébastien Joucla et al. “Extracellular neural microstimulation may activate much larger regions than expected by simulations: A combined experimental and modeling study”. In: *PLoS ONE* 7.8 (2012).

[15] Sébastien Joucla and Blaise Yvert. “Improved focalization of electrical microstimulation using microelectrode arrays: A modeling study”. In: *PLoS ONE* 4.3 (2009).

[16] Sébastien Joucla, Alain Glière, and Blaise Yvert. “Current approaches to model extracellular electrical neural microstimulation”. In: *Frontiers in Computational Neuroscience* 8.February (2014), pp. 1–12. arXiv: 1307.7701.

[17] Soheyl Noachtar and Jan Rémi. *The role of EEG in epilepsy: A critical review*. 2009.

[18] Rafael Polanía, Michael A. Nitsche, and Christian C. Ruff. *Studying and modifying brain function with non-invasive brain stimulation*. 2018.

[19] Steven G. Dickstein et al. “The neural correlates of attention deficit hyperactivity disorder: An ALE meta-analysis”. In: *Journal of Child Psychology and Psychiatry and Allied Disciplines* 47.10 (2006), pp. 1051–1062.

[20] Prashanthi Vemuri, David T Jones, and Clifford R Jack. “Resting state functional MRI in Alzheimer’s Disease.” In: *Alzheimer’s research & therapy* 4.1 (2012), p. 2.

[21] Arthur R. Houweling and Michael Brecht. “Behavioural report of single neuron stimulation in somatosensory cortex”. In: *Nature* 451.7174 (2008), pp. 65–68.

[22] P. A. Merton and H. B. Morton. “Stimulation of the cerebral cortex in the intact human subject”. In: *Nature* 285.5762 (1980), p. 227.

[23] Nir Grossman et al. “Noninvasive Deep Brain Stimulation via Temporally Interfering Electric Fields”. In: *Cell* 169.6 (2017), 1029–1041.e16.

[24] Moustafa R. K. Ali et al. “Targeting cancer cell integrins using gold nanorods in photothermal therapy inhibits migration through affecting cytoskeletal proteins”. In: *Proceedings of the National Academy of Sciences* 114.28 (2017), E5655–E5663.

[25] Agnieszka Z. Wilczewska et al. *Nanoparticles as drug delivery systems*. 2012.

[26] Ashlyn T. Young, Neil Cornwell, and Michael A. Daniele. *Neuro-Nano Interfaces: Utilizing Nano-Coatings and Nanoparticles to Enable Next-Generation Electrophysiological Recording, Neural Stimulation, and Biochemical Modulation*. 2018.

[27] Chiara Paviolo et al. "Nanoparticle-enhanced infrared neural stimulation". In: *Journal of Neural Engineering* 11.6 (2014).

[28] Ritchie Chen et al. "Wireless magnetothermal deep brain stimulation". In: *Science* 347.6229 (2015), pp. 1477–1480.

[29] Jesse D. Marshall and Mark J. Schnitzer. "Optical strategies for sensing neuronal voltage using quantum dots and other semiconductor nanocrystals". In: *ACS Nano* 7.5 (2013), pp. 4601–4609.

[30] Katherine Lugo et al. "Remote switching of cellular activity and cell signaling using light in conjunction with quantum dots". In: *Biomedical Optics Express* 3.3 (2012), p. 447.

[31] Sanshiro Hanada et al. "Cell-based in vitro blood-brain barrier model can rapidly evaluate nanoparticles' brain permeability in association with particle size and surface modification". In: *International Journal of Molecular Sciences* 15.2 (2014), pp. 1812–1825.

[32] Elizabeth A. Nance et al. "A dense poly(ethylene glycol) coating improves penetration of large polymeric nanoparticles within brain tissue". In: *Science Translational Medicine* 4.149 (2012).

[33] Jules J. Vandersarl, Alexander M. Xu, and Nicholas A. Melosh. "Nanostraws for direct fluidic intracellular access". In: *Nano Letters* 12.8 (2012), pp. 3881–3886.

[34] Tian-Ming Fu et al. "Sub-10-nm intracellular bioelectronic probes from nanowire-nanotube heterostructures." In: *Proceedings of the National Academy of Sciences of the United States of America* 111.4 (2014), pp. 1259–1264.

[35] Cameron C. McIntyre and Ross W. Anderson. *Deep brain stimulation mechanisms: the control of network activity via neurochemistry modulation*. 2016. arXiv: 15334406.

[36] Donald A. Malone et al. "Deep Brain Stimulation of the Ventral Capsule/Ventral Striatum for Treatment-Resistant Depression". In: *Biological Psychiatry* 65.4 (2009), pp. 267–275.

[37] P. Justin Rossi et al. “Proceedings of the third annual deep brain stimulation think tank: A review of emerging issues and technologies”. In: *Frontiers in Neuroscience* 10.APR (2016).

[38] Zhe Li et al. *Review on Factors Affecting Targeting Accuracy of Deep Brain Stimulation Electrode Implantation between 2001 and 2015*. 2017.

[39] Nolan R Williams, Kelly D Foote, and Michael S Okun. “STN vs. GPi Deep Brain Stimulation: Translating the Rematch into Clinical Practice.” In: *Movement disorders clinical practice* 1.1 (2014), pp. 24–35. arXiv: NIHMS150003.

[40] Marina Picillo et al. “Programming Deep Brain Stimulation for Parkinson’s Disease: The Toronto Western Hospital Algorithms”. In: *Brain Stimulation* 9.3 (2016), pp. 425–437.

[41] John S. Allen, Hanna Damasio, and Thomas J. Grabowski. “Normal neuroanatomical variation in the human brain: An MRI-volumetric study”. In: *American Journal of Physical Anthropology* 118.4 (2002), pp. 341–358.

[42] Thomas Wichmann and Mahlon R DeLong. “Deep Brain Stimulation for Movement Disorders of Basal Ganglia Origin: Restoring Function or Functionality?” In: *Neurotherapeutics* (2016), pp. 264–283.

[43] O Aquilina. “A brief history of cardiac pacing.” In: *Images in paediatric cardiology* 8.2 (2006), pp. 17–81.

[44] J. Gardner. “A history of deep brain stimulation: Technological innovation and the role of clinical assessment tools”. In: *Social Studies of Science* 43 (2013), pp. 707–728.

[45] Erik O. Udo et al. “Incidence and predictors of short- and long-term complications in pacemaker therapy: The FOLLOWPACE study”. In: *Heart Rhythm* 9.5 (2012), pp. 728–735.

[46] Zian H. Tseng et al. “Sudden death in patients with cardiac implantable electronic devices”. In: *JAMA Internal Medicine* 175.8 (2015), pp. 1342–1350.

[47] Jing Zhang et al. “The safety issues and hardware-related complications of deep brain stimulation therapy: a single-center retrospective analysis of 478 patients with Parkinson’s disease”. In: *Clinical Interventions in Aging* Volume 12 (2017), pp. 923–928.

[48] Onanong Jitkritsadakul et al. “Systematic review of hardware-related complications of Deep Brain Stimulation: Do new indications pose an increased risk?” In: *Brain Stimulation* 10.5 (2017), pp. 967–976.

[49] Carsten Buhmann et al. “Adverse events in deep brain stimulation: A retrospective long-term analysis of neurological, psychiatric and other occurrences”. In: *PLoS ONE* 12.7 (2017).

[50] Can Tao et al. “Functional dissection of synaptic circuits: in vivo patch-clamp recording in neuroscience”. In: *Frontiers in Neural Circuits* 9 (2015).

[51] W. A. Stoy et al. “Robotic navigation to subcortical neural tissue for intracellular electrophysiology in vivo”. In: *Journal of Neurophysiology* 118.2 (2017), pp. 1141–1150.

[52] Qiuyu Wu () et al. “Integration of autopatching with automated pipette and cell detection in vitro”. In: *Journal of Neurophysiology* 116.4 (2016), pp. 1564–1578.

[53] Suhasa B. Kodandaramaiah et al. “Automated whole-cell patch-clamp electrophysiology of neurons in vivo”. In: *Nature Methods* 9.6 (2012), pp. 585–587. arXiv: NIHMS150003.

[54] Suhasa B Kodandaramaiah et al. “Assembly and operation of the autopatcher for automated intracellular neural recording in vivo”. In: *Nat. Protocols* 11.4 (2016), pp. 634–654.

[55] Albert K. Lee et al. “Whole-Cell Recordings in Freely Moving Rats”. In: *Neuron* 51.4 (2006), pp. 399–407.

[56] Ziyan Zhu et al. “Cochlear-implant spatial selectivity with monopolar, bipolar and tripolar stimulation”. In: *Hearing Research* 283.1-2 (2012), pp. 45–58. arXiv: NIHMS150003.

[57] Patrick K. Campbell et al. “A Silicon-Based, Three-Dimensional Neural Interface: Manufacturing Processes for an Intracortical Electrode Array”. In: *IEEE Transactions on Biomedical Engineering* 38.8 (1991), pp. 758–768.

[58] Edwin M. Maynard, Craig T. Nordhausen, and Richard A. Normann. “The Utah Intracortical Electrode Array: A recording structure for potential brain-computer interfaces”. In: *Electroencephalography and Clinical Neurophysiology* 102.3 (1997), pp. 228–239.

[59] Changhyun Kim and Kensall D. Wise. “A 64-site multishank CMOS low-profile neural stimulating probe”. In: *IEEE Journal of Solid-State Circuits* 31.9 (1996), pp. 1230–1238.

[60] Arnold C. Hoogerwerf and Kensall D. Wise. “A Three-Dimensional Microelectrode Array for Chronic Neural Recording”. In: *IEEE Transactions on Biomedical Engineering* 41.12 (1994), pp. 1136–1146.

[61] Tobias Nyberg, Akiyoshi Shimada, and Keiichi Torimitsu. “Ion conducting polymer microelectrodes for interfacing with neural networks”. In: *Journal of Neuroscience Methods* 160.1 (2007), pp. 16–25.

[62] St??phanie P Lacour et al. “Flexible and stretchable micro-electrodes for in vitro and in vivo neural interfaces”. In: *Medical and Biological Engineering and Computing* 48.10 (2010), pp. 945–954.

[63] Aviad Hai, Joseph Shappir, and Micha E Spira. “Long-term, multisite, parallel, in-cell recording and stimulation by an array of extracellular microelectrodes.” In: *Journal of neurophysiology* 104.1 (2010), pp. 559–568.

[64] Jacob T Robinson et al. “Vertical nanowire electrode arrays as a scalable platform for intracellular interfacing to neuronal circuits”. In: *Nature Nanotechnology* 7.3 (2012), pp. 180–184. arXiv: NIHMS150003.

[65] Abhishek Prasad and Justin C Sanchez. “Quantifying long-term microelectrode array functionality using chronic in vivo impedance testing.” In: *Journal of neural engineering* 9.2 (2012), p. 26028.

[66] Alexander R Harris et al. “Conducting polymer coated neural recording electrodes.” In: *Journal of neural engineering* 10.1 (2013), p. 16004.

[67] Micha E. Spira and Aviad Hai. “Multi-electrode array technologies for neuroscience and cardiology”. In: *Nature Nanotechnology* 8.2 (2013), pp. 83–94.

[68] Marie Engelene J. Obien et al. *Revealing neuronal function through microelectrode array recordings*. 2015.

[69] Lohitash Karumbaiah et al. “Relationship between intracortical electrode design and chronic recording function”. In: *Biomaterials* 34.33 (2013), pp. 8061–8074.

[70] Tarun Saxena et al. “The impact of chronic blood-brain barrier breach on intracortical electrode function”. In: *Biomaterials* 34.20 (2013), pp. 4703–4713.

[71] David Jäckel et al. “Combination of High-density Microelectrode Array and Patch Clamp Recordings to Enable Studies of Multisynaptic Integration”. In: *Scientific Reports* 7.1 (2017).

[72] Vijay Viswam et al. “Multi-functional microelectrode array system featuring 59,760 electrodes, 2048 electrophysiology channels, impedance and neurotransmitter measurement units”. In: *Digest of Technical Papers - IEEE International Solid-State Circuits Conference*. Vol. 59. 2016, pp. 394–396. ISBN: 9781467394666.

[73] V Viswam et al. “Effects of sub-10$\mu$m electrode sizes on extracellular recording of neuronal cells”. In: *18th International Conference on Miniaturized Systems for Chemistry and Life Sciences, MicroTAS 2014*. 2014, pp. 980–982.

[74] Douglas J. Bakkum et al. “Tracking axonal action potential propagation on a high-density microelectrode array across hundreds of sites”. In: *Nature Communications* 4 (2013).

[75] C M Lopez et al. “A 16384-electrode 1024-channel multimodal CMOS MEA for high-throughput intracellular action potential measurements and impedance spectroscopy in drug-screening applications”. In: *Digest of Technical Papers - IEEE International Solid-State Circuits Conference*. Vol. 61. 2018, pp. 464–466.

[76] Dennis E Discher. “Tissue Cells Feel and Respon to the Stiffness of Their Substrate”. In: *Science* 310.5751 (2005), pp. 1139–1143. arXiv: NIHMS150003.

[77] Bashir Bhana et al. “Influence of substrate stiffness on the phenotype of heart cells”. In: *Biotechnology and Bioengineering* 105.6 (2010), pp. 1148–1160.

[78] Joseph J. Pancrazio et al. *Thinking Small: Progress on Microscale Neurostimulation Technology*. 2017.

[79] S. Ghassemi et al. “Cells test substrate rigidity by local contractions on submicrometer pillars”. In: *Proceedings of the National Academy of Sciences* 109.14 (2012), pp. 5328–5333.

[80] L. Trichet et al. “Evidence of a large-scale mechanosensing mechanism for cellular adaptation to substrate stiffness”. In: *Proceedings of the National Academy of Sciences* 109.18 (2012), pp. 6933–6938.

[81] E. C. Yusko and C. L. Asbury. “Force is a signal that cells cannot ignore”. In: *Molecular Biology of the Cell* 25.23 (2014), pp. 3717–3725.

[82] Tian Ming Fu et al. “Stable long-term chronic brain mapping at the single-neuron level”. In: *Nature Methods* 13.10 (2016), pp. 875–882.

[83] Takafumi Suzuki, Kunihiko Mabuchi, and Shoji Takeuchi. “A 3D flexible parylene probe array for multichannel neural recording”. In: *International IEEE/EMBS Conference on Neural Engineering, NER*. Vol. 2003-Janua. 2003, pp. 154–156. ISBN: 0780375793.

[84] Dae Hyeong Kim et al. “Dissolvable films of silk fibroin for ultrathin conformal bio-integrated electronics”. In: *Nature Materials* 9.6 (2010), pp. 1–7.

[85] JRogers et al. “Bioresorbable silicon electronic sensors for the brain”. In: *Nature* 530.7588 (2016), pp. 71–76.

[86] Jia Liu et al. “Syringe-injectable electronics”. In: *Nature Nanotechnology* 10.7 (2015), pp. 629–635. arXiv: NIHMS150003.

[87] Stacie M. Gutowski et al. “Host response to microgel coatings on neural electrodes implanted in the brain”. In: *Journal of Biomedical Materials Research - Part A* 102.5 (2014), pp. 1486–1499.

[88] J. N. Turner et al. “Cerebral astrocyte response to micromachined silicon implants”. In: *Experimental Neurology* 156.1 (1999), pp. 33–49.

[89] Vadim S. Polikov, Patrick A. Tresco, and William M. Reichert. *Response of brain tissue to chronically implanted neural electrodes*. 2005.

[90] Lan Luan et al. “Ultraflexible nanoelectronic probes form reliable, glial scarfree neural integration”. In: *Science Advances* 3.2 (2017).

[91] Aaron Gilletti and Jit Muthuswamy. “Brain micromotion around implants in the rodent somatosensory cortex.” In: *Journal of neural engineering* 3.3 (2006), pp. 189–195.

[92] James C. Barrese et al. “Failure mode analysis of silicon-based intracortical microelectrode arrays in non-human primates”. In: *Journal of Neural Engineering* 10.6 (2013). arXiv: 15334406.

[93] Philipp Gutruf and John A. Rogers. *Implantable, wireless device platforms for neuroscience research*. 2018.

[94] Fran A Hardaway, Ahmed M Raslan, and Kim J Burchiel. “Deep Brain Stimulation-Related Infections: Analysis of Rates, Timing, and Seasonality”. In: *Neurosurgery* 0.0 (2017), pp. 1–8.

[95] Gabriel Gagnon-Turcotte et al. “A wireless optogenetic headstage with multichannel electrophysiological recording capability”. In: *Sensors (Switzerland)* 15.9 (2015), pp. 22776–22797.

[96] Kate L. Montgomery et al. “Wirelessly powered, fully internal optogenetics for brain, spinal and peripheral circuits in mice”. In: *Nature Methods* 12.10 (2015), pp. 969–974.

[97] Sung Il Park et al. “Soft, stretchable, fully implantable miniaturized optoelectronic systems for wireless optogenetics”. In: *Nature Biotechnology* 33.12 (2015), pp. 1280–1286. arXiv: 15334406.

[98] Sung Il Park et al. “Stretchable multichannel antennas in soft wireless optoelectronic implants for optogenetics”. In: *Proceedings of the National Academy of Sciences* 113.50 (2016), E8169–E8177.

[99] Gunchul Shin et al. “Flexible Near-Field Wireless Optoelectronics as Subdermal Implants for Broad Applications in Optogenetics”. In: *Neuron* 93.3 (2017), 509–521.e3.

[100] Viviana Lovat et al. “Carbon nanotube substrates boost neuronal electrical signaling”. In: *Nano Letters* 5.6 (2005), pp. 1107–1110.

[101] Erik B. Malarkey et al. “Conductive single-walled carbon nanotube substrates modulate neuronal growth”. In: *Nano Letters* 9.1 (2009), pp. 264–268.

[102] Maricica Pacurari, Vince Castranova, and Val Vallyathan. “Single- and multi-wall carbon nanotubes versus asbestos: are the carbon nanotubes a new health risk to humans?” In: *Journal of toxicology and environmental health. Part A* 73.5 (2010), pp. 378–95.

[103] Ken Donaldson et al. *Carbon nanotubes: A review of their properties in relation to pulmonary toxicology and workplace safety*. 2006.

[104] Zhilian Yue et al. *Controlled delivery for neuro-bionic devices*. 2013.

[105] Rylie A. Green, Nigel H. Lovell, and Laura A. Poole-Warren. “Impact of co-incorporating laminin peptide dopants and neurotrophic growth factors on conducting polymer properties”. In: *Acta Biomaterialia* 6.1 (2010), pp. 63–71.

[106] Xinyan Cui et al. “In vivo studies of polypyrrole/peptide coated neural probes”. In: *Biomaterials* 24.5 (2003), pp. 777–787.

[107] Mohammad Reza Abidian, Dong Hwan Kim, and David C. Martin. *Conducting-polymer nanotubes for controlled drug release*. 2006.

[108] C. Boehler et al. “Actively controlled release of Dexamethasone from neural microelectrodes in a chronic invivo study”. In: *Biomaterials* 129 (2017), pp. 176–187.

[109] Josef A. Goding et al. “Living Bioelectronics: Strategies for Developing an Effective Long-Term Implant with Functional Neural Connections”. In: *Advanced Functional Materials* 28.12 (2018).

[110] Alejandro Carnicer-Lombarte, Henry T. Lancashire, and Anne Vanhoestenberghe. “In vitro biocompatibility and electrical stability of thick-film platinum/gold alloy electrodes printed on alumina”. In: *Journal of Neural Engineering* 14.3 (2017).

[111] Sandeep Negi et al. “Neural electrode degradation from continuous electrical stimulation: Comparison of sputtered and activated iridium oxide”. In: *Journal of Neuroscience Methods* 186.1 (2010), pp. 8–17.

[112] Dana Lynn Andre et al. “Mechanisms determining safety and performance of brain stimulating electrodes”. In: *Proceedings of the 31st Annual International Conference of the IEEE Engineering in Medicine and Biology Society: Engineering the Future of Biomedicine, EMBC 2009*. 2009, pp. 689–692. ISBN: 9781424432967.

[113] Stuart F. Cogan et al. “Tissue damage thresholds during therapeutic electrical stimulation”. In: *Journal of Neural Engineering* 13.2 (2016).

[114] Douglas B. McCreery et al. “Charge density and charge per phase as cofactors in neural injury induced by electrical stimulation”. In: *IEEE Transactions on Biomedical Engineering* 37.10 (1990), pp. 996–1001.

[115] MEDTRONIC Inc. *US FDA 1997 Medtronic Activa Tremor Control System PMA P960009 Summary of Safety and Effectiveness*. Tech. rep. 1997.

[116] Robert K. Shepherd and Douglas B. McCreery. *Basis of electrical stimulation of the cochlea and the cochlear nucleus*. 2006.

[117] C. Chen et al. *Membrane electroporation theories: A review*. 2006.

[118] Michelle Y Cheng, Markus Aswendt, and Gary K Steinberg. “Optogenetic Approaches to Target Specific Neural Circuits in Post-stroke Recovery”. In: *Neurotherapeutics* (2015), pp. 1–16.

[119] Frederic Gilbert, Alexander R. Harris, and Robert M.I. Kapsa. “Controlling Brain Cells With Light: Ethical Considerations for Optogenetic Clinical Trials”. In: *AJOB Neuroscience* 5.3 (2014), pp. 3–11.

[120] Nicola G. Ghazi et al. “Treatment of retinitis pigmentosa due to MERTK mutations by ocular subretinal injection of adeno-associated virus gene vector: results of a phase I trial”. In: *Human Genetics* 135.3 (2016), pp. 327–343.

[121] M.a. Liker et al. “Deep Brain Stimulation: An Evolving Technology”. In: *Proceedings of the IEEE* 96.7 (2008), pp. 1129–1141.

[122] Cameron C McIntyre et al. “Engineering the next generation of clinical deep brain stimulation technology”. In: *Brain Stimulation* 8.1 (2015), pp. 21–26.

[123] Elisa Castagnola et al. “Smaller , softer , lower-impedance electrodes for human neuroprosthesis : a pragmatic approach”. In: 7.April (2014), pp. 1–17.

[124] Anqi Zhang and Charles M Lieber. “Nano-Bioelectronics”. In: *Chemical Reviews* 116.1 (2016), pp. 215–257.

[125] A Petrossians, J J Whalen, and J D Weiland. “Improved electrode material for deep brain stimulation”. In: *2016 38th Annual International Conference of the IEEE Engineering in Medicine and Biology Society (EMBC)*. 2016, pp. 1798–1801. ISBN: 978-1-4577-0220-4.

[126] Andreas Elschner et al. *PEDOT: Principles and Applications of an Intrinsically Conductive Polymer*. 8. 2010, p. 380. ISBN: 9781420069129. arXiv: arXiv:1011.1669v3.

[127] D. DeLongchamp and P. T. Hammond. “Layer-by-layer assembly of PEDOT/polyaniline electrochromic devices”. In: *Advanced Materials* 13.19 (2001), pp. 1455–1459.

[128] Sanyuan Chen et al. “PEDOT/MWCNT composite film coated microelectrode arrays for neural interface improvement”. In: *Sensors and Actuators, A: Physical* 193 (2013), pp. 141–148.

[129] Ramona Gerwig et al. “PEDOT-CNT Composite Microelectrodes for Recording and Electrostimulation Applications: Fabrication, Morphology, and Electrical Properties.” In: *Frontiers in neuroengineering* 5.May (2012), p. 8.

[130] Annalisa Vacca et al. “Preparation and characterisation of transparent and flexible PEDOT:PSS/PANI electrodes by ink-jet printing and electropolymerisation”. In: *RSC Adv.* 5.97 (2015), pp. 79600–79606.

[131] Stuart F Cogan. “Neural stimulation and recording electrodes.” In: *Annual review of biomedical engineering* 10 (2008), pp. 275–309.

[132] R. Giridharagopal et al. “Electrochemical strain microscopy probes morphology-induced variations in ion uptake and performance in organic electrochemical transistors”. In: *Nature Materials* 16.7 (2017), pp. 1–6.

[133] Eleni Stavrinidou et al. “A physical interpretation of impedance at conducting polymer/electrolyte junctions”. In: *AIP Advances* 4.1 (2014).

[134] Alexander Giovannitti et al. “Controlling the mode of operation of organic transistors through side-chain engineering”. In: *Proceedings of the National Academy of Sciences* 113.43 (2016), pp. 12017–12022.

[135] Abdelmohsen Benoudjit, Mamoun M. Bader, and Wan Wardatul Amani Wan Salim. “Study of electropolymerized PEDOT:PSS transducers for application as electrochemical sensors in aqueous media”. In: *Sensing and Bio-Sensing Research* 17.January (2018), pp. 18–24.

[136] Thierry Brousse et al. “Capacitive and Pseudocapacitive Electrodes for Electrochemical Capacitors and Hybrid Devices”. In: *Metal Oxides in Supercapacitors*. 2017, pp. 1–24. ISBN: 9780128111697.

[137] R Samba, T Herrmann, and G Zeck. “PEDOT-CNT coated electrodes stimulate retinal neurons at low voltage amplitudes and low charge densities.” In: *Journal of neural engineering* 12.1 (2015), p. 16014.

[138] Xiliang Luo et al. “Highly stable carbon nanotube doped poly(3,4-ethylenedioxythiophene) for chronic neural stimulation”. In: *Biomaterials* 32.24 (2011), pp. 5551–5557. arXiv: NIHMS150003.

[139] Haihan Zhou et al. “Poly(3,4-ethylenedioxythiophene)/multiwall carbon nanotube composite coatings for improving the stability of microelectrodes in neural prostheses applications”. In: *Acta Biomaterialia* 9.5 (2013), pp. 6439–6449.

[140] Kip A Ludwig et al. “Poly(3,4-ethylenedioxythiophene) (PEDOT) polymer coatings facilitate smaller neural recording electrodes.” In: *Journal of neural engineering* 8.1 (2011), p. 14001.

[141] Brian J. Worfolk et al. “Ultrahigh electrical conductivity in solution-sheared polymeric transparent films”. In: *Proceedings of the National Academy of Sciences* 112.46 (2015), pp. 14138–14143. arXiv: arXiv:1408.1149.

[142] Hang-Beom Bu et al. “Click-functionalization of conducting poly(3,4-ethylenedioxythiophene) (PEDOT).” In: *Chemical communications (Cambridge, England)* 11 (2008), pp. 1320–1322.

[143] Liangqi Ouyang et al. “Enhanced PEDOT adhesion on solid substrates with electrografted P(EDOT-NH2)”. In: *Science Advances* 3.3 (2017).

[144] Shyh-chyang Luo et al. “Thin , Ultrasmooth , and Functionalized PEDOT Films with in Vitro and in Vivo Biocompatibility Ultrasmooth , and Functionalized PEDOT Films with in Vitro and in Vivo Biocompatibility”. In: *Society* c (2008), pp. 8071–8077.

[145] Maria Vomero et al. “Highly Stable Glassy Carbon Interfaces for Long-Term Neural Stimulation and Low-Noise Recording of Brain Activity”. In: *Scientific Reports* 7 (2017).

[146] Marco Marzocchi et al. “Physical and Electrochemical Properties of PEDOT:PSS as a Tool for Controlling Cell Growth”. In: *ACS Applied Materials & Interfaces* 7.32 (2015), pp. 17993–18003.

[147] Giada Cellot et al. “PEDOT:PSS interfaces support the development of neuronal synaptic networks with reduced neuroglia response in vitro”. In: *Frontiers in Neuroscience* 9.JAN (2016).

[148] Thomas Stöcker, Anna Köhler, and Ralf Moos. “Why does the electrical conductivity in PEDOT:PSS decrease with PSS content? A study combining thermoelectric measurements with impedance spectroscopy”. In: *Journal of Polymer Science, Part B: Polymer Physics* 50.14 (2012), pp. 976–983.

[149] Yue Wang et al. “A highly stretchable, transparent, and conductive polymer”. In: *Science Advances* 3.3 (2017).

[150] Scott B. Thourson and Christine K. Payne. “Modulation of action potentials using PEDOT:PSS conducting polymer microwires”. In: *Scientific Reports* 7.1 (2017).

[151] Jacek Gasiorowski et al. “Surface morphology, optical properties and conductivity changes of poly(3,4-ethylenedioxythiophene):poly(styrenesulfonate) by using additives”. In: *Thin Solid Films* 536 (2013), pp. 211–215.

[152] Desalegn Alemu et al. “Highly conductive PEDOT:PSS electrode by simple film treatment with methanol for ITO-free polymer solar cells”. In: *Energy & Environmental Science* 5.11 (2012), p. 9662.

[153] Kuan Sun, Yijie Xia, and Jianyong Ouyang. “Improvement in the photovoltaic efficiency of polymer solar cells by treating the poly(3,4-ethylenedioxythiophene): Poly(styrenesulfonate) buffer layer with co-solvents of hydrophilic organic solvents and hydrophobic 1,2-dichlorobenzene”. In: *Solar Energy Materials and Solar Cells*. Vol. 97. 2012, pp. 89–96. ISBN: 0927-0248.

[154] Apsar Pasha et al. “Conductivity and dielectric properties of PEDOT-PSS doped DMSO nano composite thin films”. In: *Journal of Materials Science: Materials in Electronics* 27.8 (2016), pp. 8332–8339.

[155] Mrunal S. Mahajan et al. “Changes in in-plane electrical conductivity of PEDOT:PSS thin films due to electric field induced dipolar reorientation”. In: *RSC Adv.* 5.105 (2015), pp. 86393–86401.

[156] Birol Ozturk, Ishan Talukdar, and Bret N Flanders. “Directed growth of diameter-tunable nanowires”. In: *Nanotechnology* 18 (2007), p. 365302.

[157] Birol Ozturk et al. “Single-step growth and low resistance interconnecting of gold nanowires”. In: *Nanotechnology* 18.17 (2007), p. 175707.

[158] Prem S Thapa et al. “Directional growth of polypyrrole and polythiophene wires”. In: *Applied Physics Letters* 94.3 (2009), pp. 2009–2011.

[159] Prem S Thapa et al. “Directional growth of metallic and polymeric nanowires.” In: *Nanotechnology* 20.23 (2009), p. 235307.

[160] Bret N Flanders. “Directed Electrochemical Nanowire Assembly: Precise Nanostructure Assembly Via Dendritic Solidification”. In: *Modern Physics Letters B* 26.01 (2012), p. 1130001.

[161] Nic D. Leipzig and Molly S. Shoichet. “The effect of substrate stiffness on adult neural stem cell behavior”. In: *Biomaterials* 30.36 (2009), pp. 6867–6878.

[162] Lohitash Karumbaiah et al. “The upregulation of specific interleukin (IL) receptor antagonists and paradoxical enhancement of neuronal apoptosis due to electrode induced strain and brain micromotion”. In: *Biomaterials* 33.26 (2012), pp. 5983–5996.

[163] Allen J Bard and Larry R Faulkner. *Electrochemical Methods: Fundamentals and Applications*. Vol. 677. 2001, p. 833. ISBN: 0471043729.

[164] Philip R Kennedy. “The cone electrode: a long-term electrode that records from neurites grown onto its recording surface”. In: *Journal of Neuroscience Methods* 29.3 (1989), pp. 181–193.

[165] J D Morris et al. “Conducting polymer nanowires for control of local protein concentration in solution”. In: *Journal of Physics D-Applied Physics* 50 (2017), #174003.

[166] Benjamin S. Elkin, Ashok I. Ilankovan, and Barclay Morrison. “A Detailed Viscoelastic Characterization of the P17 and Adult Rat Brain”. In: *Journal of Neurotrauma* 28.11 (2011), pp. 2235–2244.

[167] Yun-Bi Lu et al. “Viscoelastic properties of individual glial cells and neurons in the CNS”. In: *Proceedings of the National Academy of Sciences* 103.47 (2006), pp. 17759–17764.

[168] Pouria Fattahi et al. *A review of organic and inorganic biomaterials for neural interfaces*. 2014. arXiv: 15334406.

[169] L. Groenendaal et al. “Poly(3,4-ethylenedioxythiophene) and its derivatives: past, present, and future”. In: *Advanced Materials* 12.7 (2000), pp. 481–494.

[170] Niranjan S. Ramgir, Yang Yang, and Margit Zacharias. *Nanowire-based sensors*. 2010.

[171] Yanyan Cao et al. “Electrical transport and chemical sensing properties of individual conducting polymer nanowires”. In: *Nano Letters* 8.12 (2008), pp. 4653–4658.

[172] Yun Ze Long et al. “Electrical Conductivity Studies on Individual Conjugated Polymer Nanowires: Two-Probe and Four-Probe Results”. In: *Nanoscale Research Letters* 5.1 (2010), pp. 237–242.

[173] Sarah M. Richardson-Burns, Jeffrey L. Hendricks, and David C. Martin. “Electrochemical polymerization of conducting polymers in living neural tissue”. In: *Journal of Neural Engineering* 4.2 (2007).

[174] Sarah M. Richardson-Burns et al. “Polymerization of the conducting polymer poly(3,4-ethylenedioxythiophene) (PEDOT) around living neural cells”. In: *Biomaterials* 28.8 (2007), pp. 1539–1552. arXiv: NIHMS150003.

[175] Saravanarajan Shanmugham et al. “Polymer nanowire elastic moduli measured with digital pulsed force mode AFM”. In: *Langmuir* 21.22 (2005), pp. 10214–10218.

[176] Grigori Guitchounts et al. “A carbon-fiber electrode array for long-term neural recording”. In: *Journal of Neural Engineering* 10.4 (2013). arXiv: NIHMS150003.

[177] Paul H. Humble et al. “Electric field gradient focusing of proteins based on shaped ionically conductive acrylic polymer”. In: *Analytical Chemistry* 76.19 (2004), pp. 5641–5648.

[178] L Libioulle. “Very sharp gold and platinum tips to modify gold surfaces in scanning tunneling microscopy”. In: *Journal of Vacuum Science & Technology B: Microelectronics and Nanometer Structures* 13.3 (1995), p. 1325.

[179] Ute Böhme and Ulrich Scheler. “Effective charge of bovine serum albumin determined by electrophoresis NMR”. In: *Chemical Physics Letters* 435.4-6 (2007), pp. 342–345.

[180] Sabiha Runa et al. “TiO2Nanoparticles Alter the Expression of Peroxiredoxin Antioxidant Genes”. In: *Journal of Physical Chemistry C* 120.37 (2016), pp. 20736–20742.

[181] Candace C. Fleischer and Christine K. Payne. “Nanoparticle surface charge mediates the cellular receptors used by protein-nanoparticle complexes”. In: *Journal of Physical Chemistry B* 116.30 (2012), pp. 8901–8907. arXiv: NIHMS150003.

[182] Xiao Hong Nancy Xu and Edward S. Yeung. “Long-range electrostatic trapping of single-protein molecules at a liquid-solid interface”. In: *Science* 281.5383 (1998), pp. 1650–1653.

[183] Martin C. Henstridge, Edmund J.F. Dickinson, and Richard G. Compton. “On the estimation of the diffuse double layer of carbon nanotubes using classical the-

ory: Curvature effects on the Gouy-Chapman limit". In: *Chemical Physics Letters* 485.1-3 (2010), pp. 167–170.

[184] K Bohinc, V Kralj-Iglic, and A Iglic. "Thickness of electrical double layer. Effect of ion size". In: *Electrochimica Acta* 46.19 (2001), pp. 3033–3040.

[185] Martin Z. Bazant, Katsuyo Thornton, and Armand Ajdari. "Diffuse-charge dynamics in electrochemical systems". In: *Physical Review E - Statistical Physics, Plasmas, Fluids, and Related Interdisciplinary Topics* 70.2 (2004), p. 24. arXiv: 0401118 [cond-mat].

[186] Roy Biran, David C. Martin, and Patrick A. Tresco. "Neuronal cell loss accompanies the brain tissue response to chronically implanted silicon microelectrode arrays". In: *Experimental Neurology* 195.1 (2005), pp. 115–126. arXiv: 15334406.

[187] Ravi V. Bellamkonda, S. Balakrishna Pai, and Philippe Renaud. "Materials for neural interfaces". In: *MRS Bulletin* 37.6 (2012), pp. 557–561.

[188] Mijeong Kang et al. "Subcellular neural probes from single-crystal gold nanowires". In: *ACS Nano* 8.8 (2014), pp. 8182–8189.

[189] J T Robinson, M Jorgolli, and H Park. "Nanowire electrodes for high-density stimulation and measurement of neural circuits". In: *Frontiers in Neural Circuits* 7 (2013), #38.

[190] C Xie et al. "Intracellular recording of action potentials by nanopillar electroporation". In: *Nature Nanotechnology* 7.3 (2012), pp. 185–190.

[191] Z L C Lin et al. "Iridium oxide nanotube electrodes for sensitive and prolonged intracellular measurement of action potentials". In: *Nature Communications* 5 (2014), #3206.

[192] D Khodagholy et al. "Highly Conformable Conducting Polymer Electrodes for In Vivo Recordings". In: *Advanced Materials* 23.36 (2011), H268–H272.

[193] J W Jeong et al. "Soft Materials in Neuroengineering for Hard Problems in Neuroscience". In: *Neuron* 86.1 (2015), pp. 175–186.

[194] T D Y Kozai et al. "Ultrasmall implantable composite microelectrodes with bioactive surfaces for chronic neural interfaces". In: *Nature Materials* 11.12 (2012), pp. 1065–1073.

[195] D H Kim et al. "Flexible and Stretchable Electronics for Biointegrated Devices". In: *Annual Review of Biomedical Engineering* 14 (2012), pp. 113–128.

[196] D C Martin. “Molecular design, synthesis, and characterization of conjugated polymers for interfacing electronic biomedical devices with living tissue”. In: *Mrs Communications* 5.2 (2015), pp. 131–153.

[197] N K Guimard, N Gomez, and C E Schmidt. “Conducting polymers in biomedical engineering”. In: *Progress in Polymer Science* 32.8-9 (2007), pp. 876–921.

[198] K A Ludwig et al. “Chronic neural recordings using silicon microelectrode arrays electrochemically deposited with a poly(3,4-ethylenedioxythiophene) (PEDOT) film”. In: *Journal of Neural Engineering* 3.1 (2006), pp. 59–70.

[199] Y H Xiao et al. “Electrochemical polymerization of poly(hydroxymethylated-3,4-ethylenedioxythiophene) (PEDOT-MeOH) on multichannel neural probes”. In: *Sensors and Actuators B-Chemical* 99.2-3 (2004), pp. 437–443.

[200] M J Higgins et al. “Organic Conducting Polymer-Protein Interactions”. In: *Chemistry of Materials* 24.5 (2012), pp. 828–839.

[201] J Y Wong, R Langer, and D E Ingber. “Electrically conducting polymers can noninvasively control the shape and growth of mammalian-cells”. In: *Proceedings of the National Academy of Sciences of the United States of America* 91.8 (1994), pp. 3201–3204.

[202] Sarah M. Richardson-Burns et al. “Polymerization of the conducting polymer poly(3,4-ethylenedioxythiophene) (PEDOT) around living neural cells”. In: *Biomaterials* 28.8 (2007), pp. 1539–1552.

[203] H Okuzaki and M Ishihara. “Spinning and characterization of conducting microfibers”. In: *Macromolecular Rapid Communications* 24.3 (2003), pp. 261–264.

[204] D T Jayaram et al. “Controlling the Resting Membrane Potential of Cells with Conducting Polymer Microwires”. In: *Small* DOI: 10.10 (2017).

[205] Bradley A Stone, Melvyn Lieberman, and Wanda Krassowska. “Field Stimulation of Isolated Chick Heart Cells”. In: *Journal of cardiovascular electrophysiology* 10.1 (1999), pp. 92–107.

[206] Leslie Tung, Nicholas Sliz, and Michele R Mulligan. “Influence of electrical axis of stimulation on excitation of cardiac muscle cells”. In: *Circulation Research* 69.3 (1991), pp. 722–730.

[207] Ravi Ranjan and Nitish V Thakor. “Electrical stimulation of cardiac myocytes”. In: *Annals of biomedical engineering* 23.6 (1995), pp. 812–821.

[208] M Kang et al. “Electro-triggering and electrochemical monitoring of dopamine exocytosis from a single cell by using ultrathin electrodes based on Au nanowires”. In: *Nanoscale* 8.1 (2016), pp. 214–218.

[209] Emmanuelle Boubour and R Bruce Lennox. “Insulating Properties of Self-Assembled Monolayers Monitored by Impedance Spectroscopy”. In: 11 (2000), pp. 4222–4228.

[210] Jung Kim Dae et al. “A simple method for the removal of thiols on gold surfaces using an NH4OH-H2O2-H2O solution”. In: *Scanning* 30.2 (2008), pp. 118–122.

[211] Zaneta Pławińska, Agata Michalska, and Krzysztof Maksymiuk. “Optimization of capacitance of conducting polymer solid contact in ion-selective electrodes”. In: *Electrochimica Acta* 187 (2016), pp. 397–405.

[212] G Casalbore-Miceli et al. “Investigations on the ion transport mechanism in conducting polymer films”. In: *Solid State Ionics* 131.3-4 (2000), pp. 311–321.

[213] G. R. Hernández-Labrado et al. “Subdiffusion behavior in poly(3,4-ethylenedioxythiophene): Polystyrene sulfonate (PEDOT:PSS) evidenced by electrochemical impedance spectroscopy”. In: *Journal of Electroanalytical Chemistry* 659.2 (2011), pp. 201–204.

[214] Amélie A. Guex et al. “Conducting polymer electrodes for auditory brainstem implants”. In: *J. Mater. Chem. B* 3.25 (2015), pp. 5021–5027. arXiv: 15334406.

[215] Silviya M. Ojovan et al. “A feasibility study of multi-site,intracellular recordings from mammalian neurons by extracellular gold mushroom-shaped microelectrodes”. In: *Scientific Reports* 5 (2015).

[216] Jian Zhou et al. “The temperature-dependent microstructure of PEDOT/PSS films: insights from morphological, mechanical and electrical analyses”. In: *J. Mater. Chem. C* 2.46 (2014), pp. 9903–9910.

[217] Robert Kretschmer and Wolfgang Fritzsche. “Pearl chain formation of nanoparticles in microelectrode gaps by dielectrophoresis”. In: *Langmuir* 20.26 (2004), pp. 11797–11801.

# VITA

Scott Thourson was born and raised in Mount Prospect, Illinois. He graduated from Bradley University in Peoria, Illinois, with a B.S. in Mechanical Engineering. During his time at Bradley, he completed a co-op at Hamilton Sunstrand (UTC Aerospace). He enrolled in the Bioengineering Graduate Program at the Georgia Institute of Technology following his undergraduate studies. He currently resides in Atlanta, Georgia.